RESEARCH ARTICLE SUMMARY

NEURODEGENERATION

Short RNA chaperones promote aggregation-resistant TDP-43 conformers to mitigate neurodegeneration

Katie E. Copley *et al.*

Full article and list of author affiliations:
https://doi.org/10.1126/science.adv3301

INTRODUCTION: Aberrant aggregation of TDP-43, an RNA binding protein with a prion-like domain, is a pathological hallmark of amyotrophic lateral sclerosis (ALS) and frontotemporal dementia (FTD). TDP-43 mislocalization from the nucleus to the cytoplasm and subsequent aggregation drive neuronal dysfunction and death across these fatal neurodegenerative diseases. TDP-43 pathology also occurs frequently in Alzheimer's disease (AD), where it exacerbates cognitive decline, yet effective therapeutic strategies remain limited across all TDP-43 proteinopathies. Deliverable agents that prevent and reverse aberrant TDP-43 aggregation and restore functional TDP-43 to the nucleus in degenerating neurons could provide a therapeutic solution. Short RNA chaperones can solubilize TDP-43 and are highly deliverable to the central nervous system. However, critical mechanistic, translational, and functional barriers must be overcome to advance short RNA chaperones as therapeutics for TDP-43 proteinopathies.

RATIONALE: Our rationale was to address several unanswered questions about short RNA chaperones as TDP-43 therapeutics. We asked how short RNAs engage TDP-43 to antagonize aberrant assembly and how short RNAs remodel TDP-43 structure to prevent aggregation. We further explored whether short RNAs prevent aggregation of diverse disease-linked TDP-43 variants and whether optimized RNA sequences with enhanced chaperone activity can be identified. We investigated whether short RNAs mitigate aberrant TDP-43 phenotypes in optogenetic human cell models, induced pluripotent stem cell (iPSC)–derived motor neurons under oxidative stress, and ALS patient–derived motor neurons. Finally, we examined whether short RNA chaperones could ameliorate established aberrant TDP-43 phenotypes in a mouse model of TDP-43 proteinopathy where cytoplasmic TDP-43 aggregation, loss of TDP-43 function, and progressive motor neuron degeneration are already underway.

RESULTS: We elucidate how short, specific RNAs solubilize TDP-43. These short RNAs engage and stabilize the TDP-43 RNA recognition motifs, which allosterically destabilizes a conserved helical region in the prion-like domain, thereby promoting aggregation-resistant conformers. Sequence-space mining yielded short RNA chaperones with enhanced activity against wild-type TDP-43 and a broad spectrum of disease-linked variants. Critically, an enhanced short RNA chaperone directly dissolves preformed TDP-43 condensates and aggregates. Furthermore, enhanced short RNA chaperones suppress cytoplasmic TDP-43 aggregation in an optogenetic human cellular model of disease. Notably, lead short RNA chaperones do not interfere with TDP-43 function. Rather, short RNA chaperones antagonize loss of TDP-43 function in iPSC-derived motor neurons experiencing oxidative stress. Additionally, lead short RNAs restore physiological nuclear TDP-43 localization in ALS patient–derived motor neurons. Finally, in mice experiencing cytoplasmic TDP-43 aggregation, loss of function, and motor neuron degeneration, an enhanced short RNA chaperone reverses pathological TDP-43 aggregation, restores TDP-43 function, and confers neuroprotection.

CONCLUSION: We define a mechanistic framework for how short RNA chaperones counter TDP-43 aggregation through allosteric modulation of the prion-like domain. Our results establish enhanced short RNA chaperones as therapeutic candidates for TDP-43 proteinopathies, including ALS, FTD, and AD. This work provides a rational foundation for RNA-based therapeutic strategies targeting TDP-43 and demonstrates the feasibility of engineered short RNAs for mitigating fatal neurodegenerative diseases driven by pathological protein aggregation. ☐

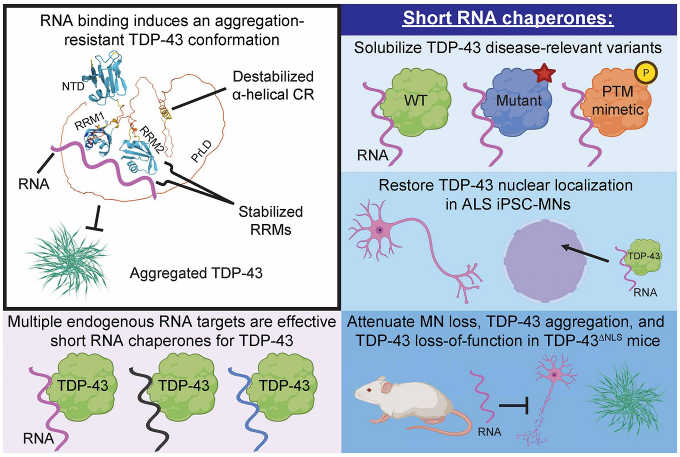

Short RNA chaperones antagonize TDP-43 aggregation through allosteric mechanisms and confer neuroprotection. (Left) RNA binding stabilizes TDP-43 RNA recognition motifs (RRMs), allosterically destabilizing the prion-like domain (PrLD) α helix and preventing aggregation. (Right) Enhanced short RNA chaperones solubilize disease-relevant TDP-43 variants; restore nuclear TDP-43 localization in ALS patient iPSC-derived motor neurons (MNs); and reverse pathological TDP-43 aggregation, restore TDP-43 function, and confer neuroprotection in mice. NTD, N-terminal domain; CR, conserved region; WT, wild-type; PTM, posttranslational modification. [Figure created with BioRender.com]

Corresponding author: James Shorter (jshorter@pennmedicine.upenn.edu) Cite this article as K. E. Copley *et al.*, *Science* **392**, eadv3301 (2026). DOI: 10.1126/science.adv3301

NEURODEGENERATION

Short RNA chaperones promote aggregation-resistant TDP-43 conformers to mitigate neurodegeneration

Katie E. Copley[1,2], Jocelyn C. Mauna[3,4,5], Helen L. Danielson[6], Qizan Chen[7], Busra Ozguney[7], Marilyn Ngo[3,4,5], Longxin Xie[3,4,5], Ashleigh Smirnov[1], Matt Davis[8,9,10], Leland Mayne[1], Miriam Linsenmeier[1], Jack D. Rubien[1], Cristian A. Bergmann[3,4,5], Bede Portz[1], Bo Lim Lee[1], Hana M. Odeh[1], Longsheng Lai[1], Yi-Wei Chang[1], Martina Hallegger[11,12,13], Jernej Ule[11,12], Piera Pasinelli[8,9,14], Yan Poon[15], Jeetain Mittal[7,16,17], Nicolas L. Fawzi[18], Ben E. Black[1], Christopher J. Donnelly[3,4,5,19,20], Brigid K. Jensen[8,9,14], James Shorter[1,2]*

Aberrant aggregation of the prion-like RNA binding protein TDP-43 drives several fatal neurodegenerative proteinopathies, including amyotrophic lateral sclerosis (ALS). In this work, we define how short, specific RNAs solubilize TDP-43. These short RNAs engage and stabilize the TDP-43 RNA recognition motifs, which allosterically destabilizes a conserved helical region in the prion-like domain, thereby promoting aggregation-resistant conformers. Sequence-space mining identified short RNA chaperones with enhanced activity against TDP-43 and disease-linked variants. Enhanced short RNA chaperones mitigated aberrant TDP-43 phenotypes in optogenetic models and in ALS patient–derived and control motor neurons. In mice with cytoplasmic TDP-43 aggregation and motor neuron loss, an enhanced short RNA chaperone reduced pathological aggregation, restored TDP-43 function, and conferred neuroprotection. These results define a mechanistic and therapeutic framework for RNA-based strategies to counter TDP-43 proteinopathies.

There are no effective therapeutics for fatal TDP-43 proteinopathies, including amyotrophic lateral sclerosis (ALS), frontotemporal dementia (FTD), limbic-predominant age-related TDP-43 encephalopathy (LATE), Alzheimer's disease (AD), and chronic traumatic encephalopathy (CTE) (*1*–*5*). A unifying feature of degenerating neurons in most ALS cases, substantial fractions of FTD and AD cases, all LATE cases, and advanced CTE cases is the aberrant cytoplasmic mislocalization and aggregation of TDP-43 (*1*–*8*). TDP-43 is an essential and predominantly nuclear RNA binding protein (RBP) with a prion-like domain (PrLD) (*1*, *2*), which plays critical roles in RNA processing, splicing, and polyadenylation (*9*, *10*). An aberrant phase transition of TDP-43 in the cytoplasm is a key pathological event that is difficult for neurons to reverse (*2*, *6*, *7*, *11*–*16*). Deliverable agents that prevent and reverse the aberrant phase transitions of TDP-43 and restore functional TDP-43 to the nucleus in degenerating neurons could provide a therapeutic solution (*2*, *11*). Such agents would eliminate any toxic gain of function of aberrant TDP-43 conformers in the cytoplasm and any toxic loss of function caused by depletion of TDP-43 from the nucleus (*2*, *11*).

TDP-43 contains two RNA recognition motifs (RRMs), which preferentially engage UG-rich RNA (Fig. 1A) (*17*). TDP-43 also harbors an intrinsically disordered PrLD, which includes a short conserved region (CR) with transient α-helical structure (Fig. 1A) (*1*, *2*, *18*, *19*). The CR plays a pivotal role in TDP-43 phase separation and aggregation (*6*, *7*, *18*–*20*). Typically, wild-type (WT) TDP-43 aggregates in disease, but rare forms of disease are connected with TDP-43 missense variants that are frequently found in the PrLD (*1*). Aberrant posttranslational modifications (PTMs) of TDP-43 occur in disease, including hyperphosphorylation and lysine acetylation (*8*, *21*, *22*). A broad-acting therapeutic should be effective against diverse disease-relevant forms of TDP-43.

RNA solubilizes TDP-43 in vitro (*13*, *14*, *23*). One short 34-nucleotide (nt) RNA derived from the 3′ untranslated region (3′UTR) of the *TARDBP* mRNA, called Clip34 (table S1 and Fig. 1B), which TDP-43 binds to regulate its own expression, can prevent and reverse WT TDP-43 phase separation and aggregation (*13*, *14*). Given the therapeutic success of short oligonucleotides (for example, antisense oligonucleotides) for neurodegenerative disease (*24*), similarly sized short RNA chaperones such as Clip34 warrant investigation as TDP-43 proteinopathy therapeutics.

Several critical barriers, however, limit development of short RNA chaperones such as Clip34. Key unknowns include (i) how short RNAs must engage TDP-43 to antagonize aberrant assembly; (ii) how short RNAs alter TDP-43 structure to prevent aggregation; (iii) whether short RNAs can prevent aggregation of diverse disease-linked TDP-43 variants, including missense mutants and TDP-43 bearing disease-linked PTMs; (iv) whether more potent short RNA chaperones against TDP-43 exist beyond Clip34; and (v) whether short RNAs mitigate aberrant TDP-43 phenotypes in human motor neurons, including ALS patient–derived motor neurons, and mouse models of disease. In this work, we addressed these pressing issues and thereby defined a mechanistic and therapeutic framework for RNA-based strategies to treat TDP-43 proteinopathies.

Results

Clip34 is an allosteric antagonist of TDP-43 aggregation

We first mapped the domains of TDP-43 required for Clip34 chaperone activity by purifying full-length TDP-43 and constructs lacking the N-terminal domain (NTD), RRM1, RRM2, RRM1/2, PrLD, or NTD/PrLD, each with a C-terminal maltose-binding protein (MBP) tag (Fig. 1A and fig. S1, A and B). Specific MBP tag removal with TEV protease triggered rapid TDP-43 aggregation, whereas the MBP-tagged TDP-43 remained soluble (fig. S1C and Fig. 1, C to I) (*13*, *25*). Upon MBP tag removal, full-length TDP-43, TDP-43$^{\Delta NTD}$, TDP-43$^{\Delta RRM1}$, and TDP-43$^{\Delta RRM2}$ aggregated robustly, whereas TDP-43 lacking the PrLD did not (Fig. 1C), as expected (*20*). Unexpectedly, TDP-43$^{\Delta RRM1/2}$ exhibited reduced aggregation (Fig. 1C), which indicates that the RRMs contribute to the aggregation propensity of TDP-43.

We assessed the ability of Clip34 to antagonize aggregation of these TDP-43 constructs. At a 1:4 RNA:TDP-43 ratio, Clip34 abolished TDP-43 aggregation (Fig. 1D), demonstrating substoichiometric efficacy. This effect was specific because Clip34 did not reduce phase separation

---

[1]Department of Biochemistry and Biophysics, Perelman School of Medicine, University of Pennsylvania, Philadelphia, PA, USA. [2]Neuroscience Graduate Group, Perelman School of Medicine, University of Pennsylvania, Philadelphia, PA, USA. [3]Department of Neurobiology, University of Pittsburgh School of Medicine, Pittsburgh, PA, USA. [4]Live Like Lou Center for ALS Research at the University of Pittsburgh Brain Institute, University of Pittsburgh School of Medicine, Pittsburgh, PA, USA. [5]Center for Neuroscience at the University of Pittsburgh, University of Pittsburgh School of Medicine, Pittsburgh, PA, USA. [6]Institute for Biology, Engineering, and Medicine, Brown University, Providence, RI, USA. [7]Artie McFerrin Department of Chemical Engineering, Texas A&M University, College Station, TX, USA. [8]Jefferson Weinberg ALS Center, Thomas Jefferson University, Philadelphia, PA, USA. [9]Vickie and Jack Farber Institute for Neuroscience, Thomas Jefferson University, Philadelphia, PA, USA. [10]Sidney Kimmel School of Medicine, Thomas Jefferson University, Philadelphia, PA, USA. [11]UK Dementia Research Institute at King's College London, London, UK. [12]The Francis Crick Institute, London, UK. [13]Oxford-GSK Institute of Molecular and Computational Medicine, Centre for Human Genetics, Nuffield Department of Medicine, University of Oxford, Oxford, UK. [14]Department of Neuroscience, Thomas Jefferson University, Philadelphia, PA, USA. [15]Confluence Therapeutics, San Francisco, CA, USA. [16]Department of Chemistry, Texas A&M University, College Station, TX, USA. [17]Interdisciplinary Graduate Program in Genetics and Genomics, Texas A&M University, College Station, TX, USA. [18]Department of Molecular Biology, Cell Biology, and Biochemistry, Brown University, Providence, RI, USA. [19]Center for Protein Conformational Diseases, University of Pittsburgh School of Medicine, Pittsburgh, PA, USA. [20]Pittsburgh Institute for Neurodegeneration, University of Pittsburgh School of Medicine, Pittsburgh, PA, USA. ***Corresponding author. Email: jshorter@pennmedicine.upenn.edu**

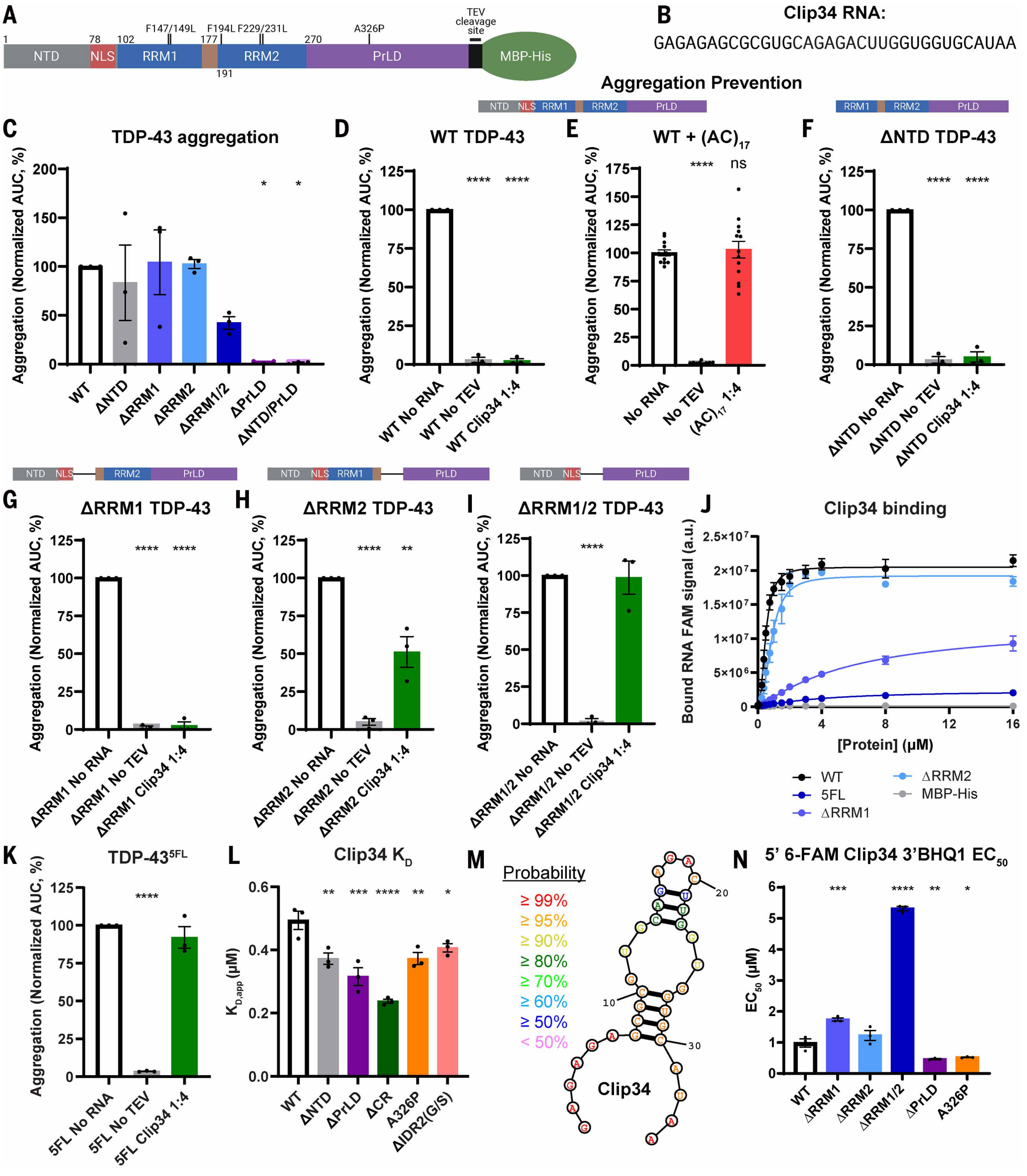

Fig. 1. Clip34 is an allosteric antagonist of TDP-43 aggregation. (**A**) Domain map of TDP-43 indicating five Phe-to-Leu mutations within the RRMs and the A326P PrLD mutation. (**B**) RNA sequence of Clip34, a 34-nt RNA derived from the 3′UTR of *TARDBP* RNA, which TDP-43 binds to regulate its expression. (**C**) Area under the curve (AUC) of standardized aggregation turbidity data for each deletion construct, normalized to WT TDP-43. Data are means ± SEMs [$n = 3$ experiments; one-way analysis of variance (ANOVA) with Dunnett's correction comparing with WT; $*P < 0.05$]. (**D** to **I**) Turbidity AUC for each variant normalized to its respective "no RNA" control; domain maps are shown above each graph. For (D) and (F) to (I), no RNA conditions are based on the same data shown in (C). Data are means ± SEMs [$n = 3$; $n = 13$ for (E); one-way ANOVA with Dunnett's correction comparing with no RNA; $**P < 0.01$; $****P < 0.0001$]. (**J**) Bound 5′ 6-FAM Clip34 signal for EMSAs with indicated TDP-43–MBP-His variants or MBP-His. Data are means ± SEMs ($n = 4$ for TDP-43^{5FL}; $n = 2$ to 3 for other TDP-43 variants; $n = 2$ for MBP-His; shown is the nonlinear regression: [agonist] versus response with variable slope, of combined replicates). (**K**) TDP-43^{5FL} turbidity AUC data normalized to the no RNA control. Data are means ± SEMs ($n = 3$; one-way ANOVA with Dunnett's correction comparing with no RNA; $****P < 0.0001$). (**L**) Apparent K_d values calculated from the bound signal of individual replicates of EMSAs performed with 5′ 6-FAM Clip34 and WT TDP-43–MBP-His or the indicated variant. WT data are the same data as in (J). Data are means ± SEMs ($n = 3$; one-way ANOVA with Dunnett's correction comparing with WT; $*P < 0.05$; $**P < 0.01$; $***P < 0.001$; $****P < 0.0001$). (**M**) Clip34 secondary structure predicted by RNAstructure. Text color indicates the probability for each nucleotide. (**N**) EC$_{50}$ values calculated from individual replicates of relative fluorescence intensity for 5′ 6-FAM Clip34 3′ BHQ1 with indicated TDP-43–MBP-His variants. Data are means ± SEMs ($n = 3$; 100 nM RNA; one-way ANOVA with Dunnett's correction comparing with WT; $*P < 0.05$; $**P < 0.01$; $***P < 0.001$; $****P < 0.0001$). Single-letter abbreviations for the amino acid residues are as follows: A, Ala; C, Cys; D, Asp; E, Glu; F, Phe; G, Gly; H, His; I, Ile; K, Lys; L, Leu; M, Met; N, Asn; P, Pro; Q, Gln; R, Arg; S, Ser; T, Thr; V, Val; W, Trp; and Y, Tyr.

of FUS (fused in sarcoma) (fig. S1, D and E), another ALS/FTD-linked RBP with a PrLD (2). Moreover, the UG-deficient RNA $(AC)_{17}$, which does not bind TDP-43, failed to inhibit aggregation (Fig. 1E). Thus, specific RNA sequences are required for chaperone activity.

Clip34 inhibited aggregation of TDP-43$^{\Delta NTD}$ (Fig. 1F), which indicates that Clip34 binding to the NTD is not required for inhibition. Clip34 also effectively inhibited TDP-43$^{\Delta RRM1}$ aggregation (Fig. 1G) but exhibited reduced activity against TDP-43$^{\Delta RRM2}$ (Fig. 1H), demonstrating that RRM2 plays an important role. Clip34 failed to prevent aggregation of TDP-43$^{\Delta RRM1/2}$ (Fig. 1I) or the isolated PrLD. Thus, Clip34 does not inhibit TDP-43 aggregation through direct interactions with the PrLD, which drives aggregation (6, 7, 20). Rather, Clip34 must engage the RRMs to antagonize TDP-43 aggregation. These results suggest that Clip34 binding to the TDP-43 RRMs elicits an allosteric effect on other domains of TDP-43, which precludes TDP-43 aggregation.

Revealing allosteric cross-talk between the TDP-43 RRMs, PrLD, and RNA

To explore how Clip34 promotes aggregation-resistant TDP-43 conformers, we explored how TDP-43 binds to Clip34. TDP-43 bound Clip34 cooperatively, with a hill slope (h) of ~2.4 and a dissociation constant (K_d) of ~0.49 μM (Fig. 1J and fig. S2, A to C). By contrast, Clip34 did not bind strongly to TDP-43^{5FL}, which bears Phe^{147}→Leu (F147L), F149L, F194L, F229L, and F231L mutations in the RRMs that impair RNA binding (Fig. 1J and fig. S2B) (26, 27). Clip34 failed to inhibit TDP-43^{5FL} aggregation (Fig. 1K). Thus, Clip34 engages the RRMs to abrogate TDP-43 aggregation and must exert allosteric effects that prevent intermolecular contacts between PrLDs.

We next assessed the contribution of each RRM. TDP-43$^{\Delta RRM1}$ binding to Clip34 was reduced by ~1.6-fold in terms of B_{max} (the maximum specific binding) compared with TDP-43, whereas TDP-43$^{\Delta RRM2}$ binding was reduced by ~1.1-fold (Fig. 1J and fig. S2B). TDP-43$^{\Delta RRM1}$ bound Clip34 with reduced cooperativity (h ~ 1.2) and a K_d of ~6.4 μM, whereas TDP-43$^{\Delta RRM2}$ bound Clip34 cooperatively (h ~ 2.5) with a K_d of ~0.9 μM (Fig. 1J and fig. S2C). Thus, RRM1 contributes more to tight, cooperative Clip34 binding than RRM2, yet Clip34 still effectively inhibited TDP-43$^{\Delta RRM1}$ aggregation and was less effective against TDP-43$^{\Delta RRM2}$ (Fig. 1, G and H). Binding affinity therefore does not fully predict chaperone activity, which indicates that Clip34 must engage TDP-43 in a specific manner to prevent aggregation, consistent with an allosteric mechanism.

We next explored the role of the NTD in binding to Clip34. The NTD negatively regulated Clip34 binding, as TDP-43$^{\Delta NTD}$ bound Clip34 with a K_d of ~0.37 μM, representing an ~1.3-fold increase in affinity compared with TDP-43 (Fig. 1L and fig. S2D). This finding is consistent with an allosteric connection between the NTD and RRMs (28). However, Clip34 still effectively inhibited TDP-43$^{\Delta NTD}$ aggregation (Fig. 1F), which indicates that the NTD is not required for Clip34 chaperone activity.

We next considered whether Clip34 binding to the RRMs allosterically affects the PrLD. The PrLD drives TDP-43 aggregation (6, 7, 20) but, in cells, also promotes binding and regulation of a subset of RNA targets, which contain >100-nt binding regions composed of dispersed motifs, including the 3′UTR of *TARDBP* mRNA (29). Most studies of TDP-43 binding to RNA have used isolated RRMs rather than full-length TDP-43 (17). Thus, the impact of the PrLD on RNA binding has remained unclear. We found that the PrLD negatively regulates Clip34 binding to the RRMs because PrLD deletion enhanced Clip34 binding (Fig. 1L and fig. S2D). TDP-43$^{\Delta PrLD}$ bound Clip34 more cooperatively (h ~ 2.7) with a K_d of ~0.32 μM, representing an ~1.5-fold affinity increase relative to TDP-43 (Fig. 1L and fig. S2D). Thus, in addition to forming intermolecular contacts that drive aggregation (6, 7, 20), the PrLD indirectly promotes TDP-43 insolubility by reducing the apparent RRM affinity for RNA. RNA binding–deficient TDP-43 is highly aggregation prone in cells (14).

To determine whether this inhibitory effect stems from a specific PrLD region, we tested TDP-43 variants with specific deletions within the PrLD (29). Deletion of the extreme C-terminal portion of the PrLD [TDP-43$^{\Delta IDR2(G/S)}$] slightly enhanced binding to Clip34, with an ~1.2-fold affinity increase relative to TDP-43 (Fig. 1L and fig. S2, D and E). Deletion of the α-helical CR of the PrLD strongly enhanced binding to Clip34, indicated by an ~2.1-fold affinity increase for TDP-43$^{\Delta CR}$, and a helix-breaking mutation within the CR, TDP-43^{A326P}, similarly enhanced binding (Fig. 1L and fig. S2, D and E). Thus, negative regulation of RNA binding by the PrLD is mediated, at least in part, by the α helicity of the CR, which is critical for TDP-43 phase separation through helix-helix interactions and aggregation through intermolecular β sheet interactions (6, 7, 16, 29, 30).

To explore whether the inhibitory effect of the PrLD on RNA binding affects Clip34 chaperone activity, we assessed TDP-43 variants bearing specific PrLD deletions (29). Clip34 exhibited enhanced ability to antagonize aggregation of all partial PrLD deletion variants tested (fig. S3 and supplementary text). Thus, the PrLD antagonizes the ability of Clip34 to reduce TDP-43 aggregation.

TDP-43 remodels Clip34 by unfolding stem-loop structure

TDP-43 RRMs frequently engage single-stranded, UG-rich RNA, which is often found in introns (17, 31, 32). However, Clip34 is predicted to form a stem-loop structure (Fig. 1M) (33). To assess this prediction, we used Clip34 bearing a 5′ fluorophore and a 3′ quencher, exploiting the predicted proximity of the 5′ and 3′ ends (Fig. 1M) (33). Low basal fluorescence indicated close apposition of the 5′ and 3′ ends (fig. S2F, red arrow). TDP-43 bound Clip34 cooperatively (Fig. 1J), which may enable unfolding of the stem-loop structure. Upon addition of TDP-43, fluorescence increased strongly (fig. S2F), which indicates that TDP-43 remodels Clip34 in a manner that increases the distance between the 5′ and 3′ ends. RRM1 deletion slightly impaired remodeling, whereas deletion of both RRMs strongly impaired remodeling (Fig. 1N and fig. S2F). Conversely, deletion of the PrLD or the CR helix-breaking TDP-43^{A326P} mutation enhanced remodeling (Fig. 1N and fig. S2F). Thus, TDP-43 remodels the Clip34 stem-loop in a predominantly RRM-dependent manner that is negatively regulated by the PrLD. This finding raised the possibility that the energetics of TDP-43–Clip34 binding might alter TDP-43 structural dynamics.

Clip34 remodels TDP-43 by stabilizing the RRMs and destabilizing the PrLD CR

We examined how Clip34 affected TDP-43 native structure using hydrogen-deuterium exchange–mass spectrometry (HXMS). HXMS measures the exchange of backbone amide hydrogens over time after dilution in D_2O-based buffer (34). When backbone hydrogens make hydrogen bonds, they exchange more slowly with deuterium (34). As backbone hydrogens make hydrogen bonds involved in protein secondary and tertiary structure, the kinetics by which the hydrogens exchange reports on the stability of structure in that region of the protein (34). Thus, we can establish how Clip34 might alter TDP-43 structural dynamics to preclude aggregation.

We performed HXMS across a wide timescale (1 s to 14.5 hours) with TDP-43 (with a C-terminal MBP tag to ensure solubility) in the absence or presence of excess Clip34 to saturate binding (table S2 and fig. S4, A to C). We achieved ≥87.9% sequence coverage of TDP-43 under all conditions (table S2 and fig. S4, A and B). For each peptide at each time point, we calculated the percentage difference in deuterium exchange between Clip34-bound and free states and then derived consensus values for individual TDP-43 residues (Fig. 2, A and B, and fig. S5).

Exchange in the NTD was similar between Clip34-bound and free states, which indicates that Clip34 binding does not affect NTD structure (Fig. 2A and fig. S6, A to C), consistent with our finding that the NTD is dispensable for Clip34 chaperone activity (Fig. 1F). By contrast, extensive decreases in exchange occurred in the RRMs in the presence

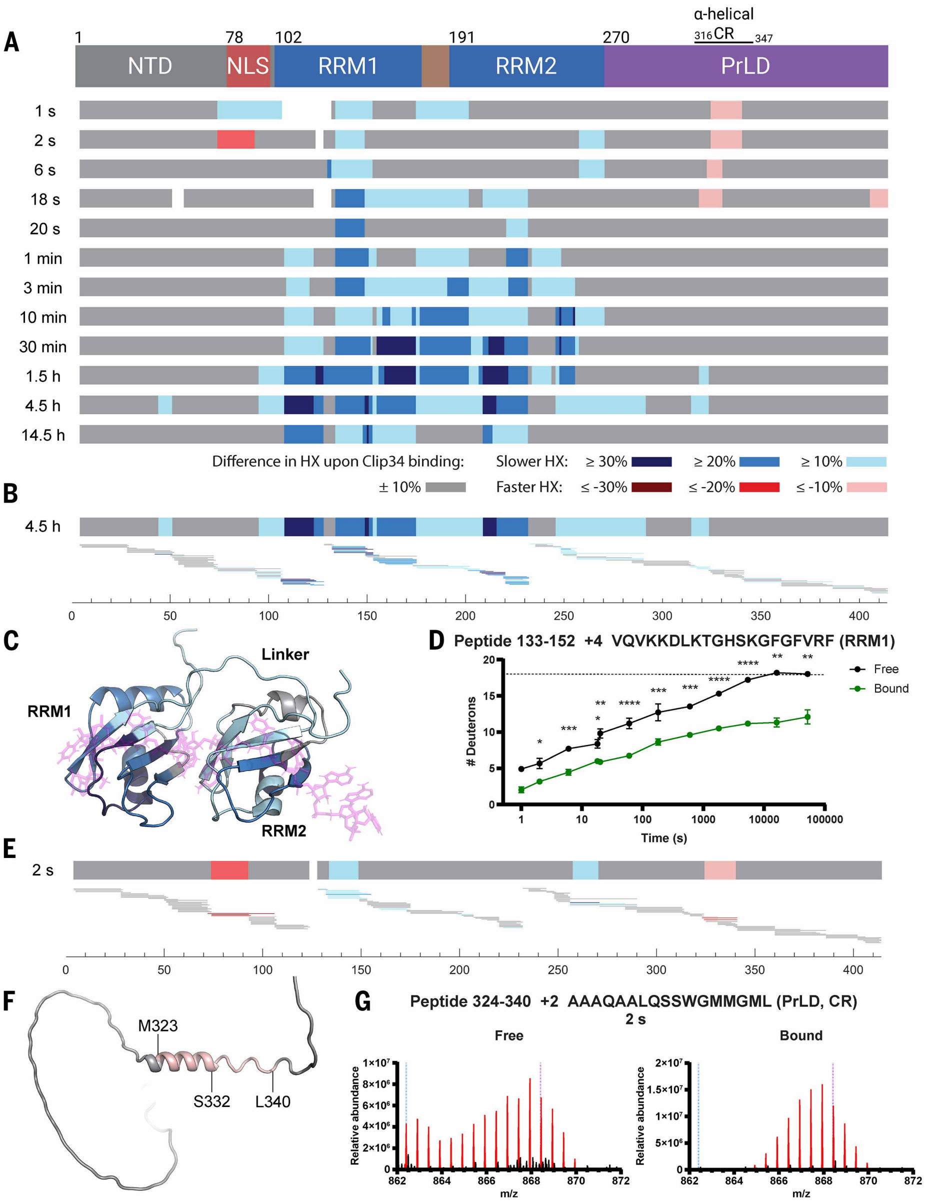

Fig. 2. Clip34 remodels TDP-43 by stabilizing the RRMs and destabilizing the PrLD CR. (**A**) Aligned with the TDP-43 domain map, for each time point, residue color corresponds to the consensus percentage difference in exchange between Clip34-bound (2:1::[Clip34]:[TDP-43]) and free states, as in the legend. White spaces are coverage gaps. (**B**) Consensus percentage difference in exchange at 4.5 hours, shown again as in (A). Aligned beneath it are peptides analyzed at 4.5 hours, with percentage differences in exchange between bound and free states colored as in (A). Amino acid number is indicated on the axis below. (**C**) Consensus percentage difference in exchange between bound and free states at 4.5 hours shown on the structure of the RRMs bound to AUG12 RNA (PDB: 4BS2), colored as in (A) and generated in PyMOL. RRMs are represented as a cartoon, whereas RNA is represented as a stick. (**D**) HX for a representative RRM1 peptide. The dashed line represents the fully deuterated condition. Data are means ± SDs (3 to 7 replicates run on MS per time point; $n = 2$ to 6 replicates per time point based on medium- or high-confidence peptide detection; some error bars too small to visualize; Welch's t test comparing bound and free at each time point; $^{*}P < 0.05$; $^{**}P < 0.01$; $^{***}P < 0.001$; $^{****}P < 0.0001$). (**E**) Consensus percentage difference in exchange at the 2-s time point, shown again as in (A). Aligned beneath it are peptides analyzed at 2 s, displayed as in (B). (**F**) Consensus percentage difference in exchange between bound and free states at 2 s shown on the cartoon representation of the AlphaFold structure of WT TDP-43 (Uniprot: Q13148), downloaded from the AlphaFold Protein Structure Database, colored as in (A) and generated in PyMOL. (**G**) Raw mass spectra at the 2-s time point for a representative peptide located in the CR. Signal corresponding to this peptide is colored red, whereas noise from overlapping peptide(s) is colored black. The blue dashed line indicates the monoisotopic peak, and the purple dashed line indicates the centroid value of the peptide in the fully deuterated sample.

of Clip34, particularly at later time points, which indicates that Clip34 stabilizes RRM1 and RRM2 structure (Fig. 2, A to D, and fig. S6, D to I). Previous nuclear magnetic resonance (NMR) studies have revealed the structure of the TDP-43 RRMs in complex with the 12-nt RNA AUG12 (table S1) (*17*). Sublocalizing exchange differences revealed that Clip34 extensively stabilized both RRMs, including throughout the β sheet RNA binding surface (Fig. 2C), with particularly strong stabilization of RNA binding residues F149 in RRM1 and F229 and F231 in RRM2 (Fig. 2B and fig. S5) (*17*). Additionally, at late time points, Clip34 exerted one of its strongest stabilizing effects on the extreme C-terminal portion of RRM1 (Y155-D174; Fig. 2A), which likely prevents localized unfolding that may contribute to aggregation (*16*).

Exchange was rapid and unaffected by Clip34 across most of the PrLD, including IDR1 and IDR2, as expected for an intrinsically disordered domain (Fig. 2A and fig. S6, J to L). There was, however, one important exception. Exchange in the CR increased substantially in the presence of Clip34, particularly at early time points (1 to 18 s), indicating destabilization (Fig. 2A, E to G; fig. S6, M and N; and fig. S7, A to C). This destabilization spans residues M323 within the predicted α helix through L340 at the end of the transient helical region (Fig. 2F) (*18*, *19*, *35*). Sublocalized analysis revealed strong destabilization at Q331 and S332 in the minor helical region (Fig. 2E and fig. S5). Thus, Clip34 induces a CR-specific destabilization spanning both major and minor helical segments, revealing an allosteric effect on the PrLD expected to antagonize aggregation.

CR peptide mass spectra exhibited bimodality at early time points, suggesting two TDP-43 populations with distinct CR structures (Fig. 2G and fig. S7, A to C). The slow-exchanging, more stabilized population is strongly represented in spectra at early time points in the free state but is poorly represented in the Clip34-bound state (Fig. 2G and fig. S7, A to C). Thus, Clip34 binding decreases the probability of a more stabilized CR structure. The CR forms a transient α-helical structure (*18*, *19*). Hence, these data suggest that in the absence of RNA, the CR forms a transient α helix, whereas upon Clip34 binding, the CR is destabilized to disfavor α helicity. Given the important role of CR α-helical structure in phase separation and aggregation (fig. S3B) (*16*, *18*, *19*, *29*), this observation helps explain how Clip34 prevents TDP-43 aggregation. Specifically, Clip34 binding induces an aggregation-resistant form of TDP-43 with stabilized RRMs and a destabilized CR in the PrLD. Consistent with this mechanism, Clip34 failed to inhibit TDP-43^{5FL} aggregation (Fig. 1K) and exhibited reduced capacity to stabilize the RRMs and disrupt

CR bimodal exchange in this variant (figs. S8 to S10 and supplementary text).

To complement these findings, all-atom molecular dynamics simulations of TDP-43 with the AUG12 RNA chaperone revealed that RNA engagement disrupts CR helicity and shifts the PrLD toward a more disordered ensemble (figs. S11 to S14 and supplementary text). This allosteric remodeling occurs without requiring direct RNA-CR contacts, which indicates that conformational changes are propagated through indirect mechanisms. Thus, RNA binding constrains RRM conformational heterogeneity while reorganizing intramolecular interactions, providing strong support for the allosteric mechanism defined by HXMS.

Enhancing Clip34 activity against diverse disease-linked TDP-43 variants

For maximal therapeutic deployability, short RNA chaperones should mitigate aggregation of diverse disease-linked TDP-43 variants, including missense variants that cause disease as well as TDP-43 bearing pathological PTMs. We assessed Clip34 chaperone activity against ALS/FTD-linked missense variants in RRM1 (P112H), the RRM1-RRM2 linker (K181E), or the PrLD (G295R, G298S, A321V, Q331K, M337V, and A382T), as well as pathological PTM mimetics including phosphorylation (S292E, S409/410E, and S292/409/410E), lysine acetylation (K145/K192Q), and physiological arginine methylation (R293F) (Fig. 3A and fig. S15, A and B) (*1*, *22*, *36*–*39*). These TDP-43 variants aggregated to a similar extent

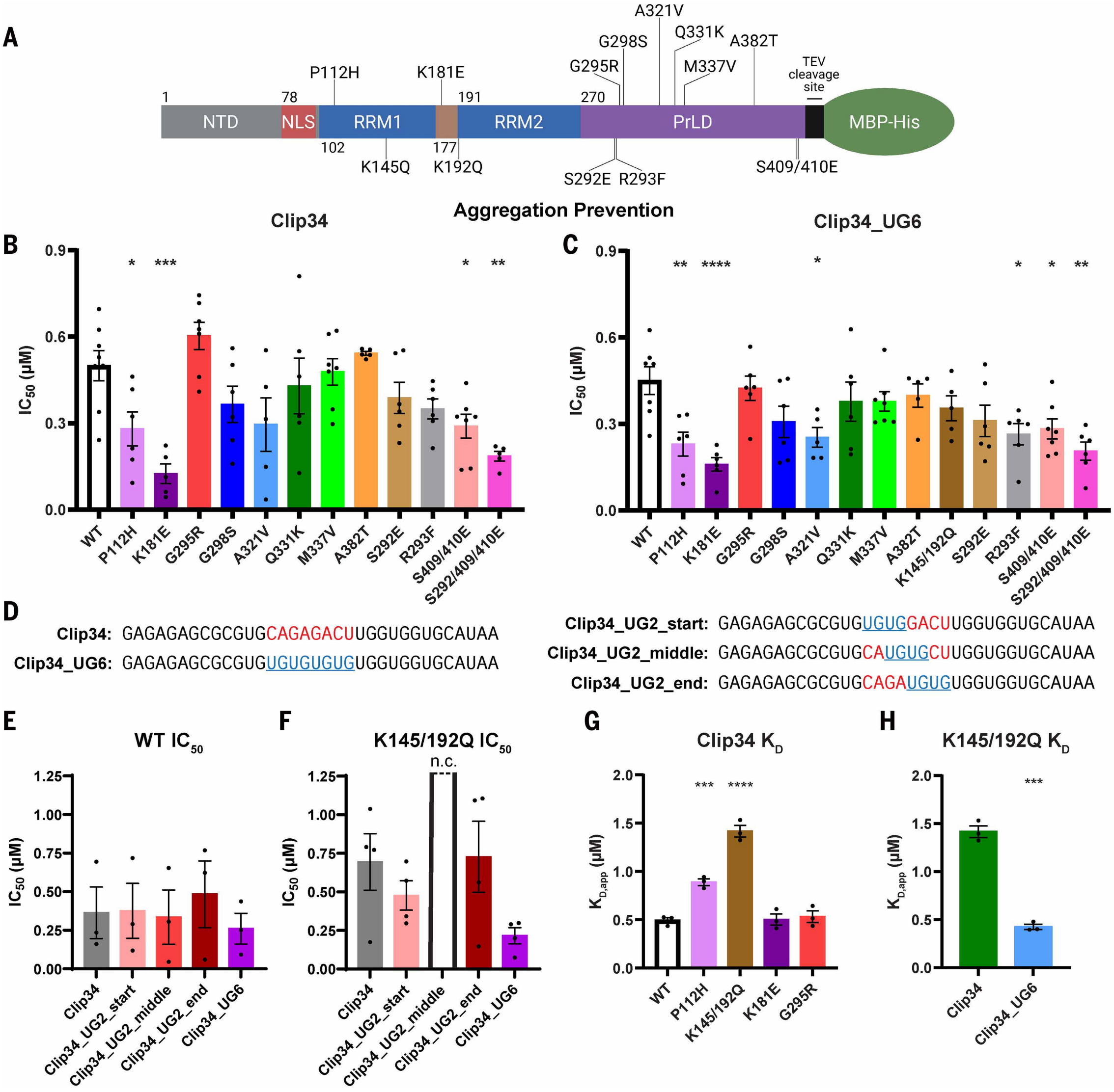

D

Clip34:	GAGAGAGCGCGUGCAGAGACUUGGUGGUGCAUAA
Clip34_UG6:	GAGAGAGCGCGUGUGUGUGUGUGGUGGUGCAUAA
Clip34_UG2_start:	GAGAGAGCGCGUGUGUGGACUUGGUGGUGCAUAA
Clip34_UG2_middle:	GAGAGAGCGCGUGCAUGUGCUUGGUGGUGCAUAA
Clip34_UG2_end:	GAGAGAGCGCGUGCAGAUGUGUGGUGGUGCAUAA

Fig. 3. Clip34 and Clip34_UG6 effectively prevent aggregation of diverse disease-linked TDP-43 variants. (**A**) Domain map of TDP-43 to scale (excluding MBP-His solubility tags). Missense mutants (top) and PTM mimetics (bottom) investigated in this study are indicated. (**B** and **C**) TDP-43–MBP-His (5 μM) was incubated with TEV protease in the presence or absence of Clip34 (B) or Clip34_UG6 (C) for 16 hours, measuring turbidity every minute in a plate reader. Standardized turbidity data were normalized to the no RNA condition for that replicate; the AUC of these data was used to calculate an IC_{50} value (nonlinear regression: [inhibitor] versus normalized response with variable slope). Data are means ± SEMs ($n = 5$ to 8; one-way ANOVA with Dunnett's correction comparing with WT; $^{*}P < 0.05$; $^{**}P < 0.01$; $^{***}P < 0.001$; $^{****}P < 0.0001$). (**D**) RNA sequences of Clip34 and its variants. Red text represents nucleotides in Clip34, whereas blue text represents nucleotides in Clip34_UG6. (**E** and **F**) IC_{50} values for Clip34 and Clip34 variants with WT TDP-43 (E) or TDP-$43^{K145/192Q}$ (F). Data are means ± SEMs ($n = 3$ to 4; n.c. indicates that an IC_{50} value could not be accurately calculated). (**G** and **H**) Apparent K_d values calculated from the bound signal from individual replicates of EMSAs performed with 5′ 6-FAM Clip34 and the indicated TDP-43 protein (G) or TDP-$43^{K145/192Q}$ with 5′ 6-FAM Clip34 or Clip34_UG6 (H). Data shown for TDP-$43^{K145/192Q}$ with Clip34 is the same in both figure parts, and WT TDP-43 with Clip34 as in Fig. 1, J and L. Data are means ± SEMs [$n = 3$; one-way ANOVA with Dunnett's correction comparing with WT (G) or unpaired t test (H); $^{***}P < 0.001$; $^{****}P < 0.0001$].

(fig. S15, C and D). Clip34 prevented aggregation of all disease-linked TDP-43 variants, with half-maximal inhibitory concentration (IC_{50}) values ranging from ~0.12 μM to 0.69 μM (Fig. 3, B and F, and fig. S15E). For a subset of TDP-43 variants, Clip34 prevented aggregation more effectively than for WT TDP-43 (IC_{50} ~ 0.5 μM), including TDP-43^{P112H} (IC_{50} ~ 0.28 μM) and TDP-43^{K181E} (IC_{50} ~ 0.12 μM; Fig. 3B). This result is notable because these mutations have been suggested to reduce RNA binding (*37*–*39*), which indicates that Clip34 can overcome this deficit. Clip34 also exhibited lower IC_{50} values against phosphomimetic variants TDP-$43^{S409/410E}$ (IC_{50} ~ 0.29 μM) and TDP-$43^{S292/409/410E}$ (IC_{50} ~ 0.19 μM; Fig. 3B), which mimic phosphoforms of TDP-43 that accumulate in pathological inclusions (*36*, *40*). Thus, Clip34 exhibits broad chaperone activity against diverse disease-linked forms of TDP-43.

Clip34 was less effective against the lysine acetylation mimetic TDP-$43^{K145/192Q}$ (IC_{50} ~ 0.69 μM) compared with WT TDP-43 (Fig. 3F and fig. S15, E to G). K145Q:K192Q mutations reduce RNA binding (*22*, *41*–*43*), which likely reduces Clip34 efficacy. This issue is problematic for Clip34 because TDP-43 acetylated at K145 accumulates in pathological inclusions in ALS (*22*).

To enhance activity against TDP-$43^{K145/192Q}$, we engineered Clip34_UG6, which harbors $(UG)_4$ in place of CAGAGACU in the middle of the sequence (Fig. 3, C and D). Clip34_UG6 binds to the isolated TDP-43 RRMs with higher affinity than Clip34 (*44*) and prevented aggregation of diverse disease-linked TDP-43 variants with IC_{50} values ranging from ~0.16 μM to 0.45 μM (Fig. 3C). Like Clip34, Clip34_UG6 was more effective against RRM1 variant TDP-43^{P112H} (IC_{50} ~ 0.23 μM), linker variant TDP-43^{K181E} (IC_{50} ~ 0.16 μM), and phosphomimetics TDP-$43^{S409/410E}$ (IC_{50} ~ 0.28 μM) and TDP-$43^{S292/409/410E}$ (IC_{50} ~ 0.21 μM) compared with WT TDP-43 (IC_{50} ~ 0.45 μM; Fig. 3C and fig. S15F). Unlike Clip34, Clip34_UG6 was substantially more effective against the PrLD variant TDP-43^{A321V} (IC_{50} ~ 0.25 μM) and the arginine methylation mimetic TDP-43^{R293F} (IC_{50} ~ 0.26 μM) compared with WT TDP-43 (IC_{50} ~ 0.45 μM; Fig. 3C). Critically, Clip34_UG6 prevented TDP-$43^{K145/192Q}$ aggregation with efficacy similar to WT TDP-43 (IC_{50} of ~0.35 versus ~0.45 μM; Fig. 3C). This enhanced activity against TDP-$43^{K145/192Q}$ could not be recapitulated by introducing $(UG)_2$ at different positions in the central portion of Clip34 (Fig. 3, D to F, and fig. S15G). Overall, Clip34_UG6 has broader applicability than Clip34 and is likely less affected by pathological K145/K192 acetylation.

To understand differences in chaperone activity, we assessed whether differing IC_{50} values reflect alterations in binding affinity by determining the K_d of select TDP-43 variants for Clip34. In some cases, K_d tracked closely with IC_{50} (Fig. 3, G and H, and fig. S15, H and I). For example, TDP-43^{G295R} bound Clip34 with similar affinity as WT TDP-43, consistent with comparable IC_{50} values (Fig. 3, B and G, and fig. S15H). Additionally, TDP-$43^{K145/K192Q}$ exhibited impaired binding to Clip34 compared with Clip34_UG6, with affinity reduced ~2.9-fold relative to WT TDP-43 (Fig. 3, G and H, and fig. S15, H and I). This finding helps explain why Clip34 is less effective against TDP-$43^{K145/192Q}$. However, in other cases, K_d did not precisely track with IC_{50}. Despite exhibiting lower IC_{50} values with Clip34 than WT TDP-43, TDP-43^{P112H} and TDP-43^{K181E} did not show increased binding affinity to Clip34 (Fig. 3, B and G, and fig. S15H). In fact, TDP-43^{P112H} displayed impaired binding to Clip34 compared with WT TDP-43 (Fig. 3G and fig. S15H). We suggest that although a certain threshold of binding affinity ($K_d < 1.4$ μM) is critical for a short RNA to effectively chaperone TDP-43, other components of the interaction beyond simple binding affinity must contribute to chaperone activity.

Mining short RNA sequence space for enhanced TDP-43 chaperones

To expand our arsenal of short RNA chaperones, we identified additional RNAs that prevent aggregation of disease-relevant TDP-43 variants (Fig. 4A and fig. S16A). The synthetic RNA $(UG)_{17}$ is an extremely potent chaperone (IC_{50} ~ 0.2 μM) for WT TDP-43 (fig. S16B) and effectively chaperoned all tested variants, including RRM missense mutants (TDP-43^{P112H} and TDP-43^{K181E}) and PrLD mutants (TDP-43^{G295R} and TDP-43^{Q331K}) (fig. S16B). Thus, simple repetitive UG sequences effectively chaperone TDP-43.

We identified potent short RNA chaperones from natural TDP-43–binding sequences (Fig. 4A), including SATIII (from pericentromeric satellite III repeats), Malat1_start (from *MALAT1* long noncoding RNA), and CLN6_middle (from the *CLN6* protein-coding transcript) (*29*, *32*, *45*, *46*). Each RNA effectively chaperoned WT TDP-43 and disease-linked variants, including TDP-$43^{K145/192Q}$ (Fig. 4B and fig. S16, C to H), with response patterns resembling those of Clip34 and Clip34_UG6. However, compared with Clip34 variants, SATIII, Malat1_start, and CLN6_middle showed fewer significant IC_{50} differences between WT and disease-associated variants (Fig. 3, B and C, and fig. S16, C to E), which suggests that they engage TDP-43 more uniformly across variants. Malat1_start emerged as the most potent natural RNA chaperone with the lowest IC_{50} values against WT TDP-43 (IC_{50} ~ 0.36 μM) and disease-linked variants (IC_{50} ~ 0.17 μM to 0.44 μM) (Fig. 4B and fig. S17, A and B). These findings support development of Malat1_start as a therapeutic short RNA.

RNAs with less steep inhibition curves (lower cooperativity) tended to be more effective chaperones (fig. S17C and supplementary text). Additional RNAs derived from *MALAT1* and *CLN6* also prevented TDP-43 aggregation, although with lower potency than Malat1_start and CLN6_middle, respectively (fig. S17, D to I, and supplementary text). Short G-quadruplex–forming RNAs, such as *LTR-III* derived from HIV-1 LTR, also effectively chaperone TDP-43, expanding the structural diversity of RNA chaperones (fig. S17, J and K, and supplementary text).

Effective RNA chaperones can engage the TDP-43 RRMs differently

Binding affinity did not uniformly correlate with IC_{50} values across our RNA panel for WT TDP-43 or TDP-43^{P112H} (Fig. 4, C and D, and fig. S18, A to C), which confirms that binding affinity alone does not determine chaperone activity. Another factor that may influence chaperone activity is exactly how each RNA engages the TDP-43 RRMs. To understand whether different short RNAs engage the TDP-43 RRMs in the same way, we conducted NMR experiments on the isolated RRMs of TDP-43 in solution.

We first performed NMR experiments with WT TDP-43 RRMs and TDP-43^{5FL} RRMs in the presence of increasing concentrations of the short $A(GU)_6$ RNA. Compared with WT, TDP-43^{5FL} RRMs displayed several broadened resonances and lacked chemical shift perturbations for a subset of residues, indicating weaker binding and involvement of fewer residues in binding RNA (fig. S18, D to G). Thus, TDP-43^{5FL} exhibits defective RNA binding (Fig. 1J) (*26*).

NMR experiments with WT TDP-43 RRMs saturated with Clip34, Clip34_UG6, and Malat1_start revealed overall similarities in resonance shifts and broadening in RRM1 (residues 138 to 142 and 160 to 172), which indicates that these regions are critical for binding, independent of RNA sequence (Fig. 4, E and F, and fig. S18, H and I). However, focused regions showed RNA sequence–dependent differences in interaction and conformational dynamics (Fig. 4, E and F, and fig. S18, H and I). Clip34 produced distinctive shifts and broadening in the region of residues 145 to 151 in the third β strand of RRM1 compared with Malat1_start (Fig. 4, E and F). This region harbors K145 that can be acetylated to disrupt RNA binding (*22*) and F147 and F149 that stack to interact with a U or G base, respectively, and are essential for RNA binding in RRM1 (*17*). Broadening and distinctive shifts were also observed in the region of residues 104 to 106 on the adjacent first β strand of RRM1 (Fig. 4, E and F). Additionally, Clip34_UG6 also showed distinct perturbations compared with Clip34 in the vicinity of K145 as well as large chemical shift perturbations at three positions between 130 and 140, distinguishing these two similar sequences (fig. S18, H and I). These differences may help explain why Clip34 is less effective in chaperoning the pathological acetylation mimic, TDP-$43^{K145/192Q}$ (*22*), compared with Clip34_UG6 and Malat1_start, which

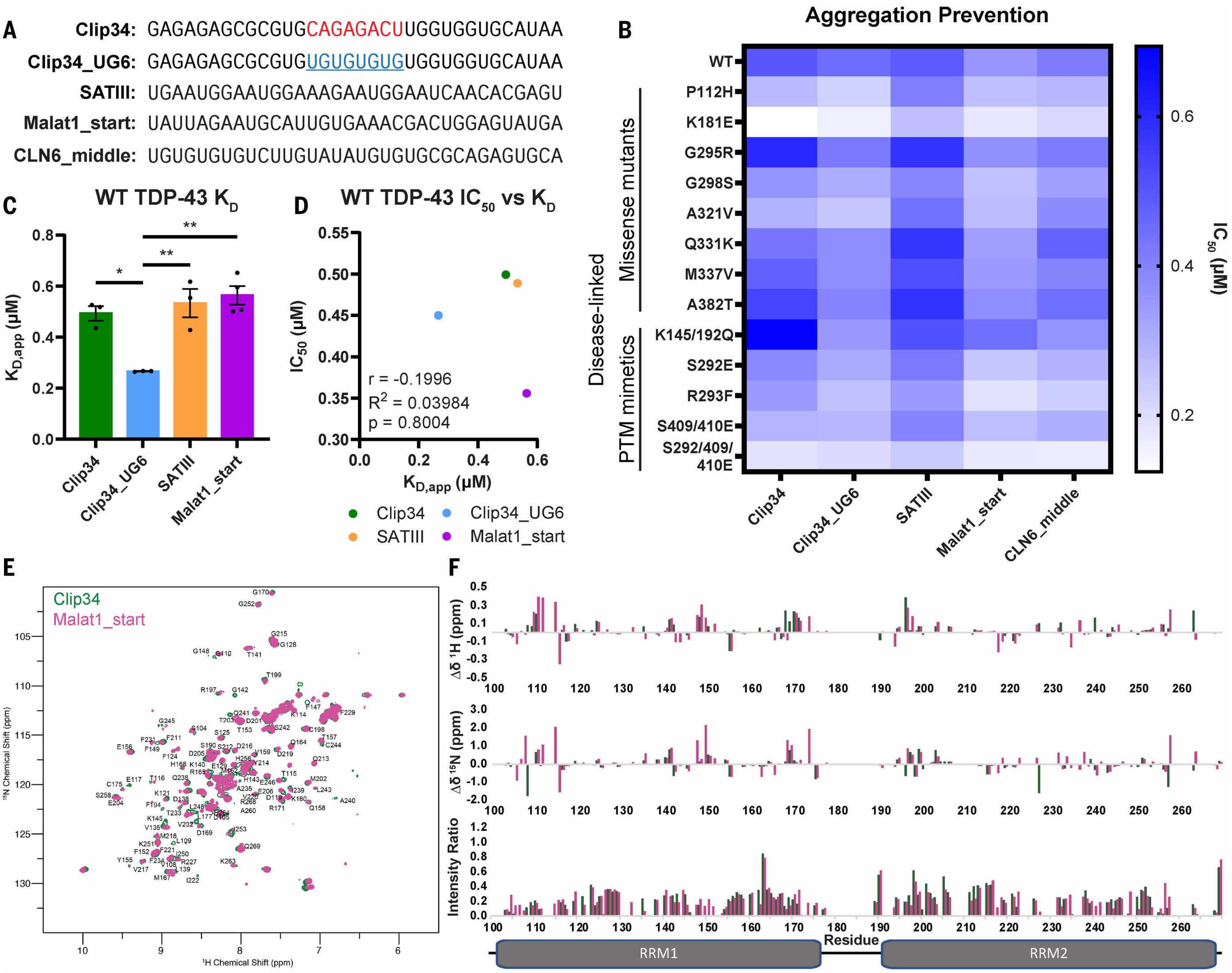

Fig. 4. Malat1_start RNA displays enhanced chaperone activity against diverse disease-linked TDP-43 variants. (**A**) RNA sequences of tested RNAs. (**B**) Heatmap displaying mean values of the individual IC_{50} data shown in Fig. 3, B, C, and F, and in fig. S16, C to E. (**C**) Apparent K_d values calculated from bound 5′ 6-FAM signal of the indicated RNAs, from individual replicates of EMSAs performed with WT TDP-43. Clip34 data are the same as shown in Fig. 3G. Data are means ± SEMs (n = 3 to 4; one-way ANOVA with Tukey's correction; $^*P < 0.05$; $^{**}P < 0.01$). (**D**) The apparent K_d values for WT TDP-43 with each indicated RNA, as shown in (C), is plotted against the IC_{50} for that RNA with WT TDP-43, as shown in (B) (Pearson correlation; not significant). (**E**) Overlay of ^{1}H–^{15}N heteronuclear single quantum coherence (HSQC) spectra of TDP-43 RRMs with Clip34 RNA (green) (2:1::[Clip34]:[TDP-43]) and Malat1_start RNA (magenta) (2:1::[Malat1_start]:[TDP-43]). (**F**) ^{1}H and ^{15}N chemical shift perturbations [$\Delta\delta^1$H (top) and $\Delta\delta^{15}$N (middle), respectively] and intensity ratios (bottom) of TDP-43 RRMs upon binding of Clip34 (green) and Malat1_start (magenta) RNA. Domain map of TDP-43 RRMs shown at the bottom, aligned to *x* axes of graphs.

are more effective (Fig. 4B). Overall, we suggest that binding affinity, the mode of RRM engagement, the cooperativity of inhibition (inversely correlated with IC_{50}), and the capacity to directly stabilize the RRMs while allosterically destabilizing the conserved helical region in the PrLD combine to influence short RNA chaperone efficacy.

Malat1_start reverses TDP-43 condensation and aberrant aggregation

Malat1_start rapidly solubilized preformed TDP-43 condensates, whereas the control RNA $(AC)_{17}$ was ineffective (fig. S19, A to C). Likewise, Malat1_start partially restored aggregated TDP-43 to the soluble fraction, whereas the control RNA $(AC)_{17}$ had no effect (fig. S20, A and B). Electron microscopy revealed that Malat1_start remodeled large aggregates into smaller structures, reducing aggregate size ~100-fold and decreasing aggregate area and density (fig. S20, C to F, and supplementary text). Thus, Malat1_start solubilizes preformed TDP-43 condensates and aggregates.

Short RNAs reduce cytoplasmic TDP-43 aggregation in an optogenetic model

We assessed short RNA efficacy in immortalized human (HEK293) cells using an optogenetic TDP-43 proteinopathy model, in which TDP-43–Cry2olig undergoes blue light–induced homo-oligomerization to form cytoplasmic puncta with disease hallmarks, including p62 and pTDP-43(pS409/410) colocalization (*13*, *14*). We tested Malat1_start (IC_{50} ~ 0.36 μM), $(UG)_{17}$ (IC_{50} ~ 0.2 μM), and CLN6_middle (IC_{50} ~ 0.42 μM) against a control RNA. Malat1_start and $(UG)_{17}$ substantially reduced cytoplasmic TDP-43 inclusion area per cell, whereas CLN6_middle did not (Fig. 5, A and B, and fig. S21, A to C). Cells treated with Malat1_start

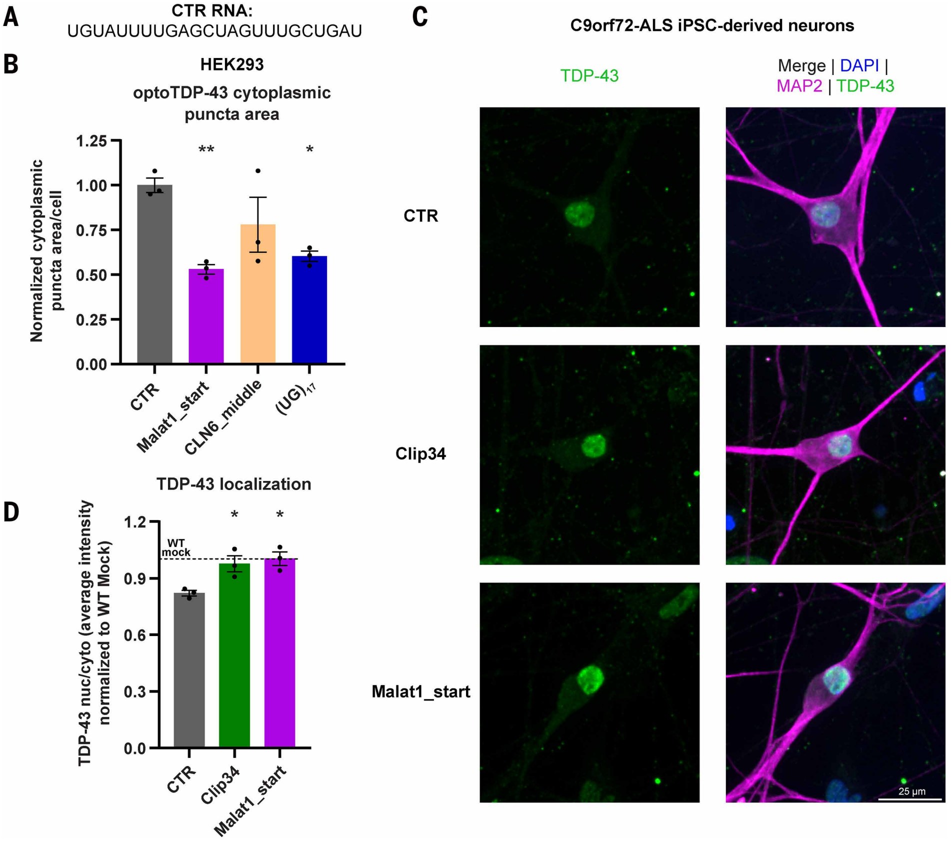

Fig. 5. Malat1_start RNA mitigates aberrant TDP-43 phenotypes in optogenetic human cell models and patient-derived neurons. (**A**) Sequence of the control (CTR) RNA. (**B**) OptoTDP-43 stable HEK293 cells were treated with the indicated RNA, followed by blue light exposure to induce Cry2olig oligomerization, and imaged after fixation. The average area of cytoplasmic puncta per cell, normalized to the average of the CTR-treated condition. Data are means ± SEMs ($n = 3$ biological replicates; one-way ANOVA with Dunnett's correction comparing with CTR; *$P < 0.05$; **$P < 0.01$). (**C**) Representative images of C9orf72-ALS patient iPSC-derived neurons treated with the indicated RNAs, stained with DAPI and for TDP-43 and MAP2. Scale bar, 25 μm. (**D**) The average ratio of TDP-43 nuclear to cytoplasmic signal, normalized to healthy control iPSC-derived neurons without RNA treatment. Data are means ± SEMs ($n = 3$ biological replicates, represented as the average of $n = 2$ technical replicates each; one-way ANOVA with Dunnett's correction comparing with CTR; *$P < 0.05$).

and (UG)$_{17}$ exhibited nuclear foci, resembling cells expressing optoTDP-43 but not exposed to blue light (dark) where optoTDP-43 forms nuclear condensates (fig. S21, A to C). Biochemical fractionation confirmed that Malat1_start solubilized optoTDP-43 in cells (fig. S21, D to F). Malat1_start and (UG)$_{17}$, the two most effective RNAs at reducing cytoplasmic puncta, also ranked highest at preventing aggregation in vitro, demonstrating that our biochemical assay provides a powerful platform for identifying RNAs with activity in human cells.

Clip34 and Malat1_start RNAs do not cause TDP-43 loss of function

A potential concern with using short RNAs is that stable binding to TDP-43 might interfere with essential RNA processing reactions. Using a CUTS biosensor to detect TDP-43 loss of function (*47*), we found that Clip34 and Malat1_start did not interfere with TDP-43 function, whereas (UG)$_{17}$ elicited undesirable TDP-43 loss of function (fig. S21G and supplementary text). Thus, (UG)$_{17}$ was excluded from further development. These results validate Clip34 and Malat1_start as therapeutic leads.

Short RNA chaperones restore physiological TDP-43 localization in ALS patient–derived motor neurons

We evaluated short RNA therapeutic potential using induced pluripotent stem cell (iPSC)–derived motor neurons from healthy control or C9-ALS patients (hexanucleotide repeat expansion in *C9orf72*). C9-ALS iPSC-derived motor neurons exhibit TDP-43 pathology characterized by decreased TDP-43 nuclear/cytoplasmic ratio (*36*, *48*). Compared with healthy control motor neurons, untreated or control RNA–treated C9-ALS neurons showed reduced TDP-43 nuclear/cytoplasmic ratio (fig. S22, A and B). Treatment with Clip34 or Malat1_start, but not control RNA, restored the TDP-43 nuclear/cytoplasmic ratio to a similar value as observed for healthy control neurons (Fig. 5, C and D, and fig. S22B). This rescue was not due to differential RNA localization because control and Malat1_start RNAs exhibited similar localization patterns in motor neurons (fig. S22C). Thus, Clip34 and Malat1_start counteract TDP-43 cytoplasmic mislocalization and restore nuclear localization in C9-ALS patient–derived motor neurons experiencing nuclear pore dysfunction (*48*, *49*).

Malat1_start restores TDP-43 functionality in stressed iPSC-derived motor neurons

We assessed whether short RNA chaperones restore TDP-43 function under stress conditions by treating control iPSC-derived human motor neurons with sodium arsenite to induce TDP-43 nuclear depletion and loss of function (fig. S23A) (*15*, *50*, *51*). Sodium arsenite triggered cryptic splicing of *STMN2* and *KCNQ2*, disrupting their normal TDP-43–dependent splicing, which is critical for axonal regeneration and neuronal excitability, respectively (*52*–*54*). Malat1_start markedly reduced cryptic splicing of both *STMN2* and *KCNQ2* compared with control RNA (fig. S23, B to E, and supplementary text). Thus, Malat1_start restores TDP-43 splicing function in stressed motor neurons.

Malat1_start does not disrupt physiological neuritic RNA granules

We confirmed that short RNA chaperones do not perturb physiological TDP-43 function in axonal RNA granules by analyzing TDP-43–containing granules in neurites of healthy control and C9-ALS iPSC-derived motor neurons (figs. S24 and S25 and supplementary text) (*55*). TDP-43–positive and Staufen-1–positive granules were unaffected by Malat1_start relative to the control RNA treatment (fig. S24 and fig. S25, A to D) (*56*). Thus, Malat1_start mitigates aberrant TDP-43 phenotypes while preserving physiological localization of TDP-43 and STAU1 to neuritic RNA granules.

Malat1_start confers neuroprotection, reverses TDP-43 aggregation, and restores TDP-43 function in mice

We tested the ability of Malat1_start to mitigate aberrant TDP-43 phenotypes in vivo using an acute spinal expression paradigm in mice (Fig. 6A) (*57*). We generated adeno-associated virus 9 (AAV9) expressing yellow fluorescent protein (YFP)–tagged TDP-43$^{\Delta NLS}$ (*58*), which results in cytoplasmic YFP-tagged TDP-43 owing to a mutated nuclear localization signal. This virus was bilaterally injected across six sites in the cervical spinal cord of p180 mice (Fig. 6A). At day 7 (D7), viral delivery to the ventral horn was highly efficient, with robust expression of

TDP-43$^{\Delta NLS}$ (fig. S26A), which formed cytoplasmic puncta (fig. S26B). At D7, animals were treated with saline or Malat1_start.

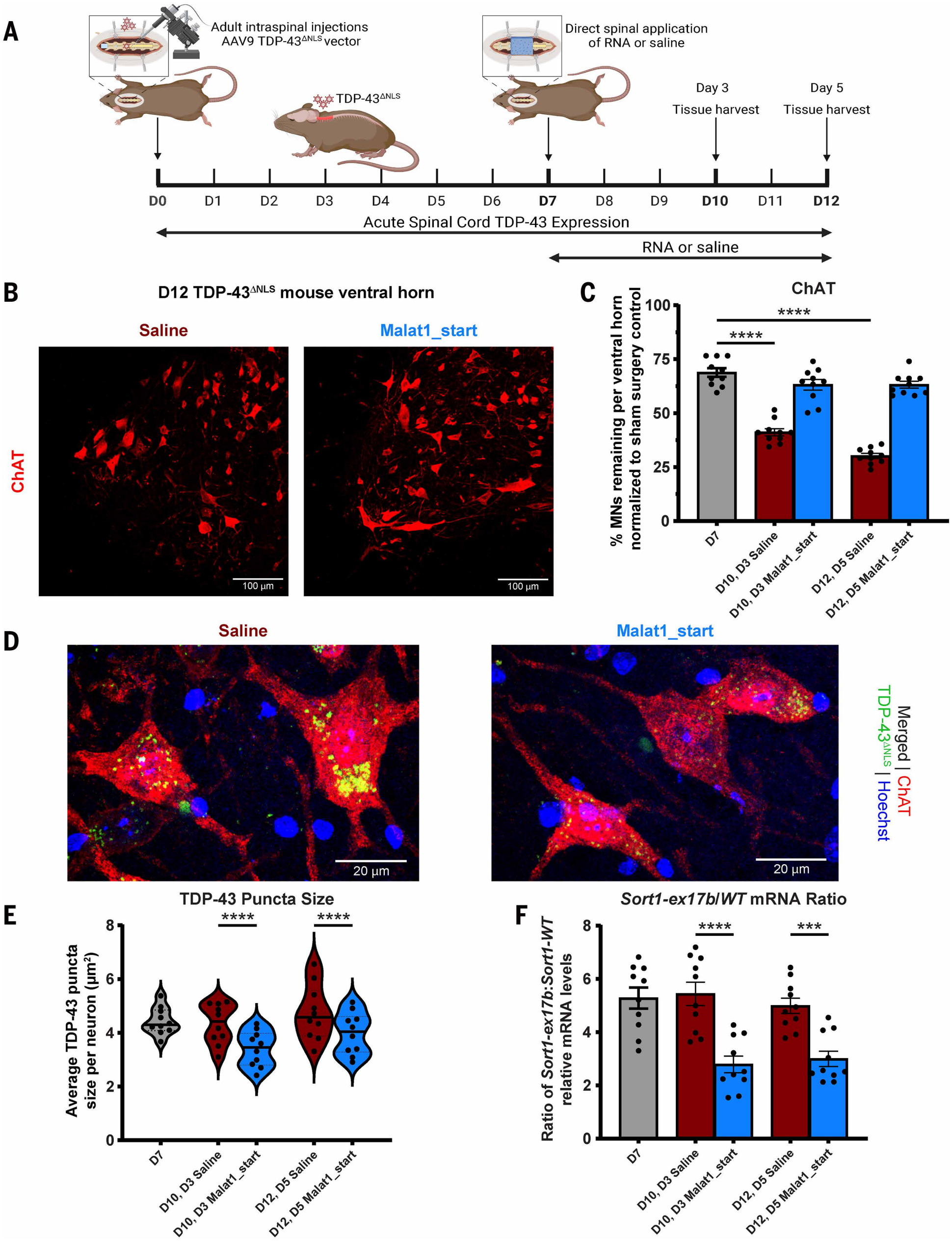

Fig. 6. Malat1_start RNA mitigates neurodegeneration, TDP-43 aggregation, and TDP-43 dysfunction in a mouse model of TDP-43 proteinopathy. (**A**) Schematic of experimental paradigm. On day 0 (D0), animals undergo laminectomy and bilateral AAV9 viral injection across the C4-C6 region, to express TDP-43$^{\Delta NLS}$ throughout the ventral horns of cervical spine. On D7, animals undergo a second surgery to receive RNA or saline. Histology was assessed at days 3 (D10) and 5 (D12) after treatment. (**B**) Representative immunohistochemistry images of ventral horns at D12, stained for ChAT. 20x magnification z-stack confocal images. Scale bar, 100 µm. (**C**) ChAT$^+$ motor neurons were manually counted within the ventral horn of spinal cord sections. Data are means ± SEMs ($n = 10$ animals per condition; shown: one-way ANOVA with Dunnett's correction comparing with D7 TDP-43; ****$P < 0.0001$; not shown: two-way ANOVA with Šídák's correction: ****$P < 0.0001$ for Malat1_start versus saline at D10 and D12). (**D**) Representative 60x magnification immunofluorescent images from 5-day (12-day expressing) saline-treated (left) and RNA-treated (right) animals. Scale bar, 20 µm. (**E**) TDP-43–positive puncta were assessed in ChAT$^+$ motor neurons at 60x magnification in the ventral horn for each animal. The average puncta size per neuron was calculated for each animal. Data shown are means ± SEMs ($n = 10$ animals per condition; average of 30 neurons per animal; shown: two-way ANOVA with Šídák's correction; ****$P < 0.0001$; not shown: one-way ANOVA with Dunnett's correction comparing with D7 TDP-43: *$P < 0.05$ for Malat1_start at D10). (**F**) The ratio of relative *Sort1* transcripts containing exon 17b to canonical *Sort1* transcripts (WT) per animal. Data shown are means ± SEMs ($n = 10$ animals per condition; shown: two-way ANOVA with Šídák's correction; ***$P < 0.001$; ****$P < 0.0001$; not shown: one-way ANOVA with Dunnett's correction comparing with D7 TDP-43: ****$P < 0.0001$ for D10 Malat1_start and ***$P < 0.001$ for D12 Malat1_start).

We verified RNA penetration to the spinal cord ventral horn and observed partial colocalization of TDP-43 puncta with Malat1_start, indicating successful target engagement (fig. S26, B and C). Motor neurons were quantified using choline acetyltransferase (ChAT) for cholinergic identity and NeuN for neuronal nuclei. Saline-treated TDP-43$^{\Delta NLS}$ animals displayed progressive loss of ChAT$^+$ motor neurons, whereas Malat1_start–treated animals maintained ChAT$^+$ motor neuron numbers (Fig. 6, B and C, and fig. S26D). Similarly, ventral horn NeuN$^+$ neurons progressively degenerated in saline-treated animals but were preserved in Malat1_start–treated animals (fig. S26E). Thus, Malat1_start mitigates TDP-43–driven neurodegeneration in vivo.

Three-dimensional image analysis revealed that average TDP-43 puncta size was reduced in Malat1_start–treated animals compared with saline controls at D10 and D12 (Fig. 6, D and E, and fig. S27A). Furthermore, the average puncta size was reduced at D10 in Malat1_start–treated animals compared with the D7 baseline (Fig. 6E). This partial reversal of TDP-43 aggregation indicates that Malat1_start acts on existing aggregates in vivo. Average TDP-43 puncta number per motor neuron increased progressively in saline-treated animals but was reduced in Malat1_start–treated animals (Fig. 6D and fig. S27, A and B). Thus, Malat1_start reduces the size and number of TDP-43 aggregates in mouse motor neurons.

We evaluated TDP-43 functionality in vivo by quantifying aberrant exon 17b inclusion in *Sort1* transcripts, a known TDP-43 splicing target in mice and humans (*43*, *59*). Total *Sort1* mRNA amounts were comparable across treatment groups (fig. S27C), but Malat1_start treatment reduced the exon 17b–containing isoform ratio by ~50% relative to saline controls (Fig. 6F). Thus, Malat1_start corrects splicing defects caused by loss of TDP-43 function in vivo. We conclude that a single dose of Malat1_start reduced motor neuron degeneration, reversed TDP-43 aggregation, and restored TDP-43 function in a mouse model of TDP-43 proteinopathy.

Discussion

We define a mechanistic and therapeutic framework in which short RNA chaperones reprogram the conformational landscape of TDP-43 to enhance solubility, restore function, and counter neurodegeneration. Central to this framework is allosteric cross-talk between the RRMs, PrLD, and RNA. Clip34 binding to the RRMs does not merely anchor TDP-43 to nucleic acid but allosterically biases the CR α helix within the PrLD toward disordered, aggregation-resistant conformations, thereby remodeling TDP-43 to depopulate aggregation-prone states. RRM2 plays a key role in transmitting RNA binding effects to the PrLD. Moreover, Clip34 imposes allosteric effects beyond destabilizing the CR α helix, broadly maintaining PrLD disorder even in CR-deletion constructs. Thus, short RNA chaperones modulate an extensive allosteric network coupling RRM occupancy to PrLD conformation, establishing a mechanistic paradigm for regulating prion-like RBPs.

Critically, regulation is bidirectional: The PrLD, particularly the α helicity of the CR, negatively regulates RRM affinity for RNA. Consistent with prior findings that the PrLD modulates TDP-43 binding at endogenous RNA regions (*29*), our data position the PrLD as a regulatory hub for tuning RNA interactions. CR deletion causes impaired neuronal function and behavioral abnormalities in mice (*60*), reinforcing the critical regulatory role of the CR. We propose that interplay between the RRMs, PrLD, and RNA maintains precise balance between TDP-43 solubility and self-assembly propensity, with TDP-43 responding dynamically to RNA availability. RNA-depleted environments, such as the cytoplasm of aging neurons or the interior of aging stress granules or alternative condensates, place TDP-43 at risk for pathological aggregation (*14*–*16*, *61*). In fact, pathological TDP-43 inclusions are typically RNA-depleted (*14*), consistent with failure of this regulatory axis.

Clip34 prevents TDP-43 aggregation even at substoichiometric amounts, a therapeutically favorable property rationalized by multivalent binding, wherein a single 34-nt RNA accommodates up to three TDP-43 molecules (*62*), depleting aggregation-permissive conformers below the nucleation threshold. Molecular dynamics simulations support this mechanism. RNA engagement remodels the TDP-43 conformational ensemble without requiring direct RNA-CR contacts, allowing limiting RNA amounts to effectively solubilize TDP-43 by depopulating aggregation-prone states.

RNA chaperones with broad applicability to sporadic and familial ALS/FTD should exhibit potent activity against disease-linked missense variants and pathological PTM mimetics. Although Clip34 effectively chaperoned diverse ALS/FTD-linked TDP-43 variants and PTM mimetics, it showed reduced activity against the acetylation mimetic K145/K192Q, which is problematic because K145-acetylated TDP-43 accumulates in ALS inclusions (*22*). Mining natural and synthetic short RNAs uncovered additional chaperones, with Malat1_start proving effective against all tested variants, including TDP-43$^{K145/K192Q}$. Notably, not all effective chaperones are suitable therapeutics: $(UG)_{17}$ prevented aggregation but interfered with TDP-43 function, disqualifying this RNA from development and cautioning against simple affinity-based screens for tight TDP-43 binders. By contrast, neither Malat1_start nor Clip34 compromised function (*13*, *27*), revealing a therapeutic window in which short RNA chaperones restore TDP-43 solubility without disrupting activity. Malat1_start also corrected TDP-43 mislocalization in patient-derived motor neurons and rescued cryptic splicing under oxidative stress in control motor neurons (*15*, *16*, *51*), demonstrating robust activity extending beyond disaggregation to restoration of nuclear TDP-43 localization and function.

To address RNA delivery challenges, we used 2'OMe-modified Malat1_start with select phosphorothioate linkages, which penetrates into the neuronal cytoplasm and targets TDP-43 aggregates in vivo. A single dose administered to mice after TDP-43 aggregation was widespread, motor neurodegeneration was underway, and TDP-43 functionality was compromised reduced TDP-43 aggregation, restored function, and prevented further degeneration. The capacity of short RNA chaperones to reverse—not merely prevent—disease-relevant TDP-43 pathology in vivo carries direct translational implications for treating patients with existing symptoms.

Our studies reveal mechanisms by which short RNA chaperones restore TDP-43 solubility and function, establishing a foundation for therapeutics targeting fatal TDP-43 proteinopathies. We envision that short RNAs preferentially engage cytoplasmic TDP-43, where competition from endogenous RNA is reduced relative to the RNA-rich nucleus (*23*), shifting equilibrium toward soluble forms competent for nuclear import. Upon binding to nuclear-import receptors, solubilized TDP-43 ejects the therapeutic RNA, freeing the RNA for further rounds of cytoplasmic solubilization (*63*). This recycling enables substoichiometric RNA to sustain TDP-43 solubilization while nuclear-import receptors return TDP-43 to the nucleus, restoring function. Notably, our short RNAs resemble US Food and Drug Administration (FDA)–approved antisense oligonucleotides in size and chemistry, which supports translational feasibility for central nervous system delivery (*24*).

Despite these advances, several limitations warrant consideration and suggest avenues for future investigation. Although short RNA chaperones reverse aberrant TDP-43 aggregation in vitro, in human cells, and in a mouse model, validation in additional mouse models that recapitulate TDP-43 pathology will be essential to establish therapeutic generalizability. Similarly, although short RNA chaperones promote TDP-43 functionality and nuclear localization in control and ALS patient–derived motor neurons, broader assessment across genetically diverse patient lines is needed to confirm efficacy across the heterogeneous ALS/FTD population. Finally, our study establishes a mechanistic framework linking RNA sequence and structure to restoration of TDP-43 solubility and functionality, yet systematic exploration of RNA sequence, structure, and chemical modification space will be required to define robust design principles and optimize therapeutic candidates. Whether we have achieved maximal potency with current short RNA chaperones remains an open question that warrants continued optimization efforts. Nonetheless, our findings establish short RNA chaperones as a promising therapeutic modality for countering TDP-43 proteinopathies.

Materials and methods

Animals

Experimental procedures were approved by the Institutional Animal Care and Use Committee (IACUC) at Thomas Jefferson University and were conducted in compliance with the Guide for the Care and Use of Laboratory Animals from the National Institutes of Health. Surgical methods and behavioral tests listed are under IACUC-approved protocol for Piera Pasinelli (01914). The Thomas Jefferson University PHS Approved animal welfare assurance ID from the NIH Office of Laboratory Animal Welfare is D16-00051 (A3085-01). Female nontransgenic C57BL/6J mice (strain no.: 000664; RRID: IMSR_JAX:000664) aged 180 days were acquired from Jackson Laboratories (https://www.jax.org/strain/000664) and housed in an animal facility with controlled humidity, temperature and light cycles, with access to ad libitum water and standard chow. As analgesics are delivered on the basis of animal weight, and to better control variance in animal starting weight, female mice were exclusively chosen for this present study.

This study represents a total of 64 animals having undergone the spinal surgeries described below. Initial characterization of viral expression used $n = 3$ animals in sham surgery, and TDP-43$^{\Delta NLS}$ groups expressing virus for 7 days. Animal numbers chosen for our large-scale cohort were based on effect sizes of ChAT+ expression noted in our test cohort. As per this assessment, guided by a power analysis assuming a desired power value of 0.80, we determined that an estimated 16 animals per time point (8 in each group) would be required. We have therefore chosen to include 10 animals per time points per group. In the main cohort of animals, there were $n = 8$ sham noninjected animals and 50 animals which received injections to express TDP-43$^{\Delta NLS}$. After 1 week, all 58 animals underwent a second surgery. Sham animals again received no treatment, whereas TDP-43$^{\Delta NLS}$ animals were subdivided into saline and RNA treatment groups ($n = 20$ for each). Of these two groups, $n = 10$ were used for each of the 3-day and

5-day endpoints for immunostaining analysis. The $n = 8$ sham animals were also collected at the 5-day endpoint.

Cell lines

iPSC lines CS15iCTR-5, CS29iALS-n1, and CS52iALS-n6A were obtained from the Cedars-Sinai RMI iPSC Core, and are male. Line JH034 was obtained from Johns Hopkins Hospital, and is female. The estimated G4C2 repeat expansion sizes are >2.5 kb for line JH034, and 6 to 8 kb for lines CS29iALS-n1 and CS52iALS-n6A.

iPSCs were differentiated into motor neurons following previously described protocols (*64*, *65*). iPSCs were cultured in Matrigel (Corning) and mTeSR+ (StemCell Technologies) and kept in a humidified chamber with regulated CO_2 (5%) and temperature (37°C). For differentiation, 1x10^6 iPSCs were plated in 6-well plates. Once cells reached ~90% confluency, media was changed from mTeSR+ to N2B27 media (50% DMEM:F12, 50% Neurobasal, plus NEAA, Glutamax, N2 and B27; all from Gibco) plus 10 µM SB431542 (StemCell Technologies), 100 nM LDN-193189 (Sigma-Aldrich), 1 µM RA (Sigma-Aldrich) and 1 µM Smoothened-Agonist (SAG, Cayman Chemical). Media was changed daily for a total of 6 days. Cells were then switched to N2B27 including 1 µM RA, 1 µM SAG, 4 µM SU5402 (Cayman Chemical) and 5 µM DAPT (Cayman Chemical), and media was changed daily until day 13. Neurons were dissociated on day 14 using TrypLE and DNAse I, and plated in Matrigel-coated 24-well plates with glass coverslips for confocal imaging studies. Cells were fed every other day and maintained for 13 days after plating in Neurobasal media + NEAA, Glutamax, N2, B27, plus 10 ng/ml BDNF, GDNF, CNTF (all from PeproTech) and 0.2 µg/ml Ascorbic acid (Sigma-Aldrich).

HEK293 cells were obtained from ATCC (catalog no. CRL-1573).

Microbe strains

Escherichia coli BL21 (DE3)-RIL cells (Agilent 230245) and BL21 Star (DE3) Chemically competent cells (Thermo Fisher C601003) were used for protein purification, with growth conditions as described in the purification sections. *E. coli* XL10-Gold Ultracompetent cells (Agilent 200314) were used for cloning and plasmid propagation and were grown at 37°C with the appropriate antibiotic.

Cloning

pJ4M was from Addgene (plasmid no. 104480; https://www.addgene.org/104480/; RRID:Addgene_104480) (*66*). All other TDP-43 constructs purified were generated using the pJ4M plasmid. Partial PrLD deletion plasmids were generated previously (*29*). TDP-43^{5FL} was generated previously (*14*). TDP-43^{S292E}, TDP-43^{R293F}, TDP-$43^{S409/410E}$, and TDP-$43^{S292/409/410E}$ plasmids were generated previously (*36*). All other TDP-43 disease-relevant variants and domain deletion plasmids, as well as the MBP-His plasmid, were generated via QuikChange Site-Directed Mutagenesis (Agilent 210518). MBP-FUS was generated previously (*67*).

Purification of TEV protease

TEV protease was purified as previously described (*13*). His-TEV plasmid was transformed into BL21 (DE3)-RIL *E. coli* and grown on an LB-ampicillin plate at 37°C for 16 hours. The cells were then transferred to a starter culture of LB containing 100 µg/ml ampicillin and 34 µg/ml chloramphenicol, and incubated at 37°C for 2 hours while shaking at 250 rpm. After 2 hours, the starter culture was diluted 1:100 into the main culture of LB containing 100 µg/ml ampicillin and 34 µg/ml chloramphenicol. The main culture was shaken at 37°C and 250 rpm until the optical density measured at a wavelength of 600 nm (OD_{600}) reached ~0.7, then stored at 4°C for ~30 min while the incubator cooled to 15°C. The culture was then induced with 1 mM isopropyl-β-D-thiogalactopyranoside (IPTG) (MilliporeSigma 420322), and grown shaking at 250 rpm for 16 hours at 15°C. After 16 hours, the culture was harvested by centrifugation at 4658 rcf at 4°C for 25 min. The pelleted cells were resuspended in 30 ml Lysis Buffer {500 mM NaCl, 25 mM Tris-HCl pH 8.0, supplemented with 10 mM β-mercaptoethanol and cOmplete, EDTA-free Protease Inhibitor Cocktail [MilliporeSigma (Roche) 5056489001] at 1 tablet/50 ml buffer}. The resuspended cells were lysed on ice with 1 mg/ml lysozyme (MilliporeSigma L6876) for 30 min, then sonication. The lysate was then centrifuged at 30,597 rcf at 4°C for 20 min.

A CV of 2.67 ml of Ni-NTA resin (QIAGEN 30250) was used per 1 liter of prep, and the Ni-NTA resin was equilibrated with 10 CV of MilliQ and 6 CV of Lysis Buffer. The clarified supernatant was rotated with Ni-NTA resin for 1.5 hours at 4°C, then centrifuged at 179 rcf at 4°C for 5 min. The Ni-NTA resin was then washed with 25 CV of Wash Buffer (500 mM NaCl, 25 mM Tris-HCl pH 8.0, 25 mM imidazole, supplemented with 10 mM β-mercaptoethanol), with centrifugations performed at 179 rcf at 4°C for 2 min. The Ni-NTA resin was then resuspended in 2 CV of Wash Buffer and applied to a chromatography column. Protein was eluted with 5 CV of Elution Buffer (500 mM NaCl, 25 mM Tris-HCl pH 8.0, 300 mM imidazole, supplemented with 10 mM β-mercaptoethanol). Eluted protein was pooled and concentrated to ~10 ml using an Amicon Ultra-15 Centrifugal Filter Unit, MWCO 30 kDa (Millipore UFC9030), by centrifugation at 716 rcf at 4°C. Concentrated protein was centrifuged at 716 rcf at 4°C for 3 min. Dialysis tubing was equilibrated in Dialysis Buffer (25 mM HEPES-NaOH pH 7.0, 5% glycerol, supplemented with 5 mM β-mercaptoethanol) for ~10 min. The protein was dialyzed in 5 liters of Dialysis Buffer overnight, stirring at 4°C.

Dialyzed protein was centrifuged at 716 rcf at 4°C for 10 min. Filtered supernatant was purified using fast protein liquid chromatography (FPLC) with a HiTrap SP XL column, equilibrated in Low-Salt ion exchange (IEX) Buffer [25 mM HEPES-NaOH pH 7.0, 5% glycerol, supplemented with 5 mM dithiothreitol (DTT)]. The column was washed with 2 CV of Low-Salt IEX Buffer, then protein was eluted using a 0 to 80% gradient with Low-Salt IEX Buffer as the base buffer, and High-Salt IEX Buffer (750 mM NaCl, 25 mM HEPES-NaOH pH 7.0, 5% glycerol, supplemented with 5 mM DTT) as the elution buffer. Based on the chromatogram, elution fractions were pooled and concentrated to ~40 mg/ml using an Amicon Ultra-15 Centrifugal Filter Unit, MWCO 30 kDa (Millipore), by centrifugation at 716 rcf at 4°C. The concentrated protein was supplemented to 50% glycerol with 100% glycerol, then aliquoted, flash-frozen in liquid nitrogen, and stored at −80°C until use.

Purification of TDP-43–MBP-His

TDP-43–MBP-His, or MBP-His alone, plasmids were transformed into BL21 (DE3)-RIL *E. coli* and grown on LB-Kanamycin plates at 37°C for 16 hours. The cells were then transferred to a starter culture of LB containing 50 µg/ml kanamycin and 34 µg/ml chloramphenicol, and incubated at 37°C for 4 hours while shaking at 250 rpm. After 4 hours, the starter culture was diluted 1:100 into the main culture of 1 liter of LB containing 50 µg/ml kanamycin, 34 µg/ml chloramphenicol, and 0.2% glucose. The main culture was shaken at 37°C and 250 rpm until the OD_{600} reached ~0.25, then continued to grow while cooling to 16°C, and induced with 1 mM IPTG after reaching 16°C and an OD_{600} of ~0.5 to 0.6. The induced culture was grown shaking at 250 rpm for 16 hours at 16°C. After 16 hours, the culture was harvested by centrifugation at 4658 rcf at 4°C for 20 min. The pelleted cells were resuspended in 20 ml of Resuspension/Wash Buffer [1 M NaCl, 20 mM Tris-HCl pH 8.0, 10% glycerol, 10 mM imidazole pH 8.0, supplemented with 1 mM DTT, 5 µM Pepstatin A, 100 µM phenylmethylsulfonyl fluoride (PMSF), and cOmplete, EDTA-free Protease Inhibitor Cocktail at 1 tablet/50 ml buffer]. The resuspended cells were lysed on ice with 1 mg/ml lysozyme for 30 min, then sonication. The lysate was then centrifuged at 30,966 rcf at 4°C for 20 min.

A CV of 5 ml of Ni-NTA resin (QIAGEN) was used per 1 liter of prep, and the Ni-NTA resin was equilibrated with 18 CV of MilliQ and 3 CV of Resuspension/Wash Buffer. The clarified supernatant was rotated with Ni-NTA resin for 1 hour at 4°C, then centrifuged at 179 rcf (2000 rpm; 50 ml tubes) at 4°C for 4 min. The Ni-NTA slurry was then applied to a chromatography column, with the flow-through reapplied once. At 4°C, the column was washed with 10 CV of Resuspension/Wash buffer, then eluted in 3 CV of Nickel Elution Buffer (1 M NaCl, 20 mM Tris-HCl pH 8.0, 10% glycerol, 300 mM imidazole pH 8.0, supplemented with 1 mM DTT, 5 μM Pepstatin A, 100 μM PMSF, and cOmplete, EDTA-free Protease Inhibitor Cocktail at 1 tablet/50 ml buffer). Eluted fractions were stored overnight at 4°C.

Eluted fractions were pooled based on purity determined by SDS–polyacrylamide gel electrophoresis (SDS-PAGE). Approximate protein concentration was determined by Bradford, and 1 ml amylose resin (New England Biolabs E8021L) per 6 mg protein was used as the amylose resin CV. Amylose resin was equilibrated in ~10 CV MilliQ and 3 CV Resuspension/Wash Buffer. The protein was rotated with amylose resin at 4°C for 30 min, then centrifuged at 179 rcf at 4°C for 4 min. The amylose slurry was then applied to a chromatography column, with the flow-through reapplied once. At 4°C, the column was washed with 5 CV of Resuspension/Wash buffer, then eluted in 3 CV of Amylose Elution Buffer (1 M NaCl, 20 mM Tris-HCl pH 8.0, 10% glycerol, 10 mM imidazole pH 8.0, supplemented with 1 mM DTT, 5 μM Pepstatin A, 100 μM PMSF, 10 mM maltose). Eluted fractions were pooled based on purity determined by SDS-PAGE, then concentrated using an Amicon Ultra-15 Centrifugal Filter Unit, MWCO 50 kDa (Millipore UFC9050), by centrifugation at 716 rcf at 4°C, until a concentration of ~150 to 200 μM was achieved. The protein was aliquoted, flash-frozen in liquid nitrogen, and stored at −80°C until use.

Purification of TDP-43–MBP-His used for condensation assays

Purification was performed based on a previously described protocol (*66*). TDP-43–MBP-His plasmid was transformed into One Shot BL21 Star (DE3) *E. coli* (Thermo Fisher Scientific) and grown on LB-Kanamycin plates at 37°C for 16 hours. The cells were then transferred to a starter culture of LB containing 50 μg/ml kanamycin, and grown at 37°C and 250 rpm. The starter culture was diluted into a main culture of 1 liter of LB containing 50 μg/ml kanamycin and 0.2% glucose, which was grown at 37°C and 250 rpm until reaching an OD_{600} of ~0.5 to 0.6. The culture was then incubated at 4°C for 30 to 45 min, then induced with 1 mM IPTG and grown at 16°C and 250 rpm for 16 hours. After 16 hours, the culture was harvested by centrifugation at 4658 rcf at 4°C for 20 min. The pelleted cells were resuspended in 30 ml of Lysis Buffer (1 M NaCl, 20 mM Tris-HCl pH 8.0, 10 mM imidazole pH 8.0, 10% glycerol, and supplemented with 2.5 mM β-mercaptoethanol and cOmplete, EDTA-free Protease Inhibitor Cocktail at 1 tablet/50 ml buffer). The resuspended cells were lysed by sonication, then centrifuged at 48,384 rcf at 4°C for 1 hour, then filtered.

The filtered lysate was purified using an FPLC with a XK 50/20 column (Cytiva) packed with Ni-NTA agarose beads (Qiagen), equilibrated in Lysis Buffer. The column was washed with 3 CV of Buffer A (Lysis Buffer without Protease Inhibitor Cocktail), then protein was eluted using a 0 to 80% gradient with Buffer A as the base buffer, and Buffer B (1 M NaCl, 20 mM Tris-HCl pH 8.0, 500 mM imidazole pH 8.0, 10% glycerol, and supplemented with 2.5 mM β-mercaptoethanol) as the elution buffer. Desired elution fractions were pooled, concentrated with an Amicon Ultra-15 Centrifugal Filter Unit, MWCO 50 kDa (Millipore), and filtered. The filtered protein was then further purified using an FPLC with a 26/600 Superdex 200 pg column (Cytiva), equilibrated in SEC Buffer (300 mM NaCl, 20 mM Tris-HCl pH 8.0, and supplemented with 1 mM DTT). The fractions from the second out of three peaks, as determined by absorbance at 280 nm, were pooled and concentrated with an Amicon Ultra-15 Centrifugal Filter Unit, MWCO 50 kDa (Millipore) until a concentration of at least 250 μM. The protein was aliquoted, flash-frozen in liquid nitrogen, and stored at −80°C until use.

Purification of MBP-FUS

MBP-FUS was purified based on previous protocols (*67*). In brief, MBP-FUS plasmid DNA was transformed into One Shot BL21 Star (DE3) *E. coli* (Thermo Fisher Scientific) cells via heat shock, plated on LB agar plates containing 100 μg/ml ampicillin and incubated overnight at 37°C. The next day, bacterial cultures were scaled-up in LB media supplied with 100 μg/ml ampicillin and 0.2% glucose and grown to an OD_{600} of 0.6 at 37°C. Expression was induced by adding 1 mM IPTG followed by incubation for 16 hours at 16°C and 250 rpm. Cells were harvested by centrifugation for 20 min at 4658 rcf and 4°C. Cells were resuspended in lysis buffer (20 mM HEPES-NaOH, pH 7.4, 50 mM NaCl, 2 mM EDTA, 10% glucose, 2 mM DTT), supplied with 20 mg/ml lysozyme and incubated on ice for 30 min. After sonication, the lysate was centrifuged for 20 min at 30,966 rcf and 4°C.

The supernatant was pooled and added to 5 ml amylose beads (New England Biolabs) equilibrated with resuspension buffer and nutated for 2 hours at 4°C. Subsequently, the beads were washed with resuspension buffer and eluted using the same buffer supplied with 10 mM maltose. For further purification and RNA removal, the eluted sample was loaded onto a Heparin column (HiTrap Heparin HP, Cytiva) equilibrated with resuspension buffer using an FPLC. The sample was eluted with a linear gradient ranging from 0 to 80% high-salt buffer (20 mM HEPES-NaOH, pH 7.4, 1 M NaCl, 2 mM EDTA, 10% glucose, 2 mM DTT) over 90 ml. Protein-containing fractions were pooled, concentrated using an Amicon spin concentrator (Merck Millipore, MWCO 50 kDa) and flash-frozen in liquid nitrogen.

Purification of TDP-43 RRMs used for NMR experiments

The TDP-43^{5FL} RRMs plasmid was synthesized in the pJ411 vector by GenScript. WT TDP-43 RRMs (102 to 269) was expressed via a codon-optimized sequence in the pJ411 vector. Protein growth and purification protocols were adapted from the literature (*17*). The protein was grown in BL21 Star (DE3) *E. coli* cells in M9 minimal media supplemented with $^{15}NH_4Cl$ for isotopic labeling. Bacterial cultures were grown at 37°C with agitation at 200 rpm to an optical density of 0.8. The cultures were induced with 1 mM IPTG and grown for 4 additional hours before harvesting by centrifugation at 6000 rpm and 4°C for 15 min and resuspended in lysis buffer (20 mM HEPES-NaOH pH 7.5, 1 M NaCl, 30 mM imidazole, 1 mM DTT) supplemented with an EDTA-free protease inhibitor cocktail (Roche). The cells were lysed using an EmulsiFlex C3 homogenizer (Avestin), and the lysate was cleared by centrifugation at 20,000 rpm and 4°C for 1 hour. The protein was eluted via a nickel HisTrap HP column (GE Healthcare) by affinity chromatography with a linear gradient of elution buffer (20 mM HEPES pH 7.5, 1 M NaCl, 300 mM imidazole, 1 mM DTT). The hexahistidine tag was cleaved by overnight dialysis with 0.03 mg/ml TEV protease at room temperature (RT) (20 mM HEPES-NaOH pH 7.5, 500 mM NaCl, 1 mM DTT). The tag and TEV protease were removed with an additional elution over the HisTrap HP column. The purified protein was buffer exchanged into NMR buffer (20 mM KP_i pH 6.8, 1 mM DTT), concentrated to ~1 mM, flash-frozen, and stored at −80°C.

RNA oligonucleotides

All RNA oligonucleotides used were purchased from Integrated DNA Technologies (IDT) or Horizon Discovery. All RNAs used for in vitro pure protein assays were unmodified and purified with standard desalting [except for RNAs used for NMR, which were high-performance liquid chromatography (HPLC) purified], and were resuspended in ribonuclease (RNase)–free water, with nanodrop measurement performed to calculate the RNA concentration. RNAs used for cellular experiments were HPLC purified and were fully 2'OMe modified; the Clip34 RNA also had five phosphorothioate backbone modifications on each end of the RNA. RNAs used for mouse experiments were purified with in vivo HPLC, were fully 2'OMe modified, and had five phosphorothioate backbone modifications on each end of the RNA. A subset of RNA used for mouse experiments contained a 5′ Cy5 fluorophore.

In vitro TDP-43 aggregation prevention assay

RNA was thawed on ice, then serially diluted in water to achieve the desired working concentrations. Protein was thawed on ice, then centrifuged at 21,300 rcf for 10 min at 4°C. Protein was then buffer exchanged into aggregation assay buffer (166.66 mM NaCl, 22.22 mM HEPES-NaOH pH 7.0, 1.11 mM DTT) using Micro Bio-Spin Chromatography Columns (BIO-RAD 7326200), following manufacturer's instructions. After buffer exchange, nanodrop measurements were performed to calculate protein concentration. Aggregation assay buffer, and subsequently protein, were added to the tubes containing water/RNA, to achieve sample reactions with final concentrations of 5 μM TDP-43, 150 mM NaCl, 20 mM HEPES-NaOH pH 7.0, 1 mM DTT, with varying concentrations of RNA. The reactions were incubated for 15 min at RT after the addition of protein. To a 96-well nonbinding plate (Greiner Bio-One 655906), 0.25 μg TEV protease was added for a final concentration of 2.5 μg/ml, or TEV protease elution buffer for the No TEV control. The reactions were then added to the 96-well plate. The 96-well plate was sealed using parafilm. Turbidity was measured at absorbance 395 nm in a Tecan plate reader (Infinite M1000 or Safire2) for 16 hours, measuring every 1 min. Plate reader measurements were conducted at ambient temperature, typically ~25° to 30°C.

For quantification, turbidity data were first standardized by setting the initial value for each well to 0. For the standardized data, any negative values were also set to 0. For normalization, the maximum value of the standardized "no RNA" condition data for a replicate was set to 100, with all other conditions for that protein in the replicate normalized based on this. Area under the curve (AUC) was calculated for the normalized data. To then normalize the AUC data, the AUC for the no RNA condition was set to 100. This analysis was performed separately for each replicate. The normalized AUC was then used to calculate an IC_{50} value for each replicate, using nonlinear regression: [inhibitor] versus normalized response with variable slope. The IC_{50} value for each replicate was then combined to generate summary data.

In vitro FUS phase separation prevention assay

RNA was thawed on ice and diluted in water and 2x PS buffer to achieve the desired RNA concentration in 1x FUS PS buffer (20 mM HEPES-NaOH pH 7.4, 1 mM DTT). Protein was thawed on ice, then centrifuged at 21,300 rcf for 5 min at 4°C. Protein was diluted to 6 μM in FUS elution buffer (570 mM NaCl, 20 mM HEPES-NaOH pH 7.4, 2 mM EDTA, 10% glycerol, 0.5 mM DTT). TEV protease was diluted to 0.12 mg/ml in 1x FUS LLPS buffer. Equal volumes of protein and RNA were mixed, then transferred to a 384-well glass bottom plate (Azenta MGB101-1-2-LG-L). Diluted TEV protease was then added directly to the samples in the 384-well plate, to achieve final concentrations of 2 μM FUS protein, varying concentrations of RNA, 0.04 mg/ml TEV protease, 190 mM NaCl, 20 mM HEPES-NaOH pH 7.4, 0.83 mM DTT, 0.67 mM EDTA, and 3.33% glycerol. Turbidity was measured at absorbance 395 nm in a BMG Labtech plate reader (CLARIOstar Plus) for ~2 to 2.5 hours at 26°C, measuring every 1 min. At the endpoint of turbidity measurements, samples were imaged within the plate by brightfield microscopy with a 100x objective (EVOS M5000).

Electrophoretic mobility shift assay (EMSA)

Protein was thawed on ice, then centrifuged at 21,300 rcf for 10 min at 4°C. Protein was then buffer exchanged into 150 mM NaCl, 20 mM HEPES-NaOH pH 7.0 (or pH 6.0 where indicated), 10% glycerol, 1 mM DTT using BIO-RAD Micro Bio-Spin Chromatography Columns, following manufacturer's instructions. After buffer exchange, nanodrop measurements were performed to calculate protein concentration. Protein was diluted in buffer to achieve a working concentration of 50 μM, in EMSA assay buffer [150 mM NaCl, 20 mM HEPES-NaOH pH 7.0 (or pH 6.0 where indicated), 10% glycerol, 1 mM DTT, 20 ng/μl bovine serum albumin (BSA) (Thermo Fisher 23209), 2.5 ng/μl yeast tRNA (Thermo Fisher AM7119), 0.4 U/μl RNasin (Promega N2511)]. Protein was then serially diluted in EMSA assay buffer to achieve a range of protein concentrations. 20 μM 5′ 6-FAM RNA resuspended in RNase-free water was diluted to 1 μM in EMSA assay buffer (10x working concentration). 10x RNA was then added to protein samples to achieve 100 nM (1x) RNA and a range of protein concentrations in EMSA assay buffer. Samples were incubated at RT for 30 min. During this incubation, 6% DNA Retardation gels (Thermo Fisher EC63655BOX) were prerun in 0.5x TBE buffer at 150 V for ~20 min. 1x dye was prepared by dilution of 5x dye (20 mM EDTA, 50% sucrose, 0.25% bromophenol blue) in EMSA assay buffer. After incubation, heparin (MilliporeSigma H3393) was added to each sample to achieve a final concentration of 0.5 mg/ml heparin. 15 μl of 1x dye was loaded in the first lane to monitor sample progression while 15 μl of undyed sample was loaded in remaining lanes. Gels were run at 150 V for 40 min. Gels were then imaged on a Typhoon Scanner using FAM fluorescence measurement. The signal of bound TDP-43 in each lane was quantified using Image Studio Lite.

SDS-PAGE

Samples were diluted in 3x sample buffer (187.5 mM Tris-HCl, 6% SDS, 30% glycerol, 0.05% bromophenol blue, pH 6.8, 1.42 M β-mercaptoethanol) and boiled at 95°C for 5 min. Precision Plus Protein Dual Color Standard (BIO-RAD 1610374) and samples were loaded on Tris-HCl gels (4 to 15% or 4 to 20% as indicated) (BIO-RAD 3450027, 3450033), and run at 175 V for 1 hour 15 min. Gels were stained with Coomassie Brilliant Blue, followed by incubation with Destain I (40% methanol, 7% acetic acid), then Destain II (5% methanol, 7% acetic acid) overnight before imaging.

Fluorescence 5′ 6-FAM Clip34 3′ BHQ1 assay

Protein was thawed on ice, then centrifuged at 21,300 rcf for 10 min at 4°C. Protein was then buffer exchanged into fluorescence assay buffer (150 mM NaCl, 20 mM HEPES-NaOH pH 7.0, 1 mM DTT) using BIO-RAD Micro Bio-Spin Chromatography Columns, following manufacturer's instructions. After buffer exchange, nanodrop measurements were performed to calculate protein concentration. Protein was diluted in fluorescence assay buffer to achieve a working concentration of 50 μM. Protein was then serially diluted in fluorescence assay buffer to achieve a range of protein concentrations. 20 μM 5′ 6-FAM 3′ BHQ1 RNA resuspended in RNase-free water was diluted to 1 μM in fluorescence assay buffer (10x working concentration). 10x RNA was then added to a 96-well nonbinding plate (Greiner). Protein samples were then also added to the 96-well plate, to achieve final concentrations of 100 nM 5′ 6-FAM Clip34 3′ BHQ1, and a range of protein concentrations, in 150 mM NaCl, 20 mM HEPES-NaOH pH 7.0, 1 mM DTT. Samples were incubated at RT for 30 min.

Fluorescence was measured in a Tecan plate reader (Spark) at 25°C. Excitation: 475 nm; bandwidth: 15 nm. Emission: 520 nm; bandwidth: 20 nm. A gain value of 80 was used for all trials. The turbidity value at 30 min was used. For each protein variant, it was validated that the signal was stable at the 30 min time point by measuring after sample addition to the plate, for 1 hour every 1 min, for at least one replicate. For quantification, $(F-F_0)/F_0$ values were calculated for each condition: the average signal for the RNA alone (no TDP-43) condition was subtracted from the signal for a condition, which was then divided by the average signal for the RNA alone (no TDP-43) condition. Half-maximal effective concentration (EC_{50}) values were determined from these data, by performing nonlinear regression: [agonist] versus response with variable slope for each replicate.

HXMS

RNA was thawed on ice where needed. Protein was thawed on ice, then centrifuged at 21,300 rcf for 10 min at 4°C. For "free" conditions, protein was buffer exchanged into nondeuterated buffer (150 mM NaCl, 20 mM HEPES-NaOH pH 7.0, 1 mM DTT) using BIO-RAD Micro Bio-Spin Chromatography Columns, following manufacturer's instructions. After buffer exchange, nanodrop measurements were performed to calculate protein concentration. Protein was then diluted in nondeuterated buffer to make a protein sample consisting of 20 μM TDP-43–MBP-His in 150 mM NaCl, 20 mM HEPES-NaOH pH 7.0, 1 mM DTT. Deuterium on-exchange was performed at 25°C by mixing 10 μl of sample with 40 μl of deuterium on-exchange buffer (D_2O-based; 150 mM NaCl, 20 mM HEPES-NaOD pH 7.0, 1 mM DTT), resulting in a D_2O concentration of 80%. At the indicated time point, the exchange reaction was quenched by addition of 10 μl of ice-cold 250 mM phosphoric acid, to achieve a final pH of pH 2.5. For nondeuterated samples, 10 μl of sample was mixed with 40 μl of nondeuterated buffer, then quenched by addition of 10 μl of ice-cold 250 mM phosphoric acid. For the fully deuterated sample, 10 μl of sample was mixed with 40 μl of on-exchange buffer, incubated at 30°C for ~18 hours, then quenched by addition of 10 μl of ice-cold 250 mM phosphoric acid. For "Clip34-bound" conditions, all procedures were the same, except that the protein was buffer exchanged into 166.67 mM NaCl, 22.22 mM HEPES-NaOH pH 7.0, 1.11 mM DTT, then diluted into the same buffer along with RNA and water, to achieve final sample concentrations of 20 μM TDP-43–MBP-His and 40 μM Clip34 in 150 mM NaCl, 20 mM HEPES-NaOH pH 7.0, 1 mM DTT.

HX measurements from 20 s to 14.5 hours were performed at pH 7.0. To measure less protected, faster exchanging parts of the protein, another set of measurements was performed at pH 6.0. Due to the direct dependence of the intrinsic exchange rate on OH^- concentration, these measurements can be put on the same time axis as the pH 7.0 measurements by dividing the actual exchange time by 10 (*68*). For the subset of time points done with pH 6–based buffer, all procedures were the same, except that the HEPES-NaOH component of both the nondeuterated buffer and on-exchange buffer was at pH 6.0, and the quench reagent used was ice-cold 145 mM phosphoric acid (to achieve a final pH of pH 2.5). All 1 s, 2 s, 6 s, and 18 s time points were collected using pH 6.0 buffer; 1 min and 3 min time points were collected with some replicates using pH 6.0 buffer and others using pH 7.0 buffer; 20 s, and 10 min and longer time points were collected using pH 7.0 buffer. For example, the 1-min time points were measured by 1 min of on-exchange at pH 7.0, or 10 min of on-exchange at pH 6.0. The agreement between these duplicated replicates indicates that the protein structural stability measured by HX is not affected by the pH change. In addition, WT TDP-43 and Clip34 were confirmed to maintain binding at pH 6.0.

For MS analysis, the sample was digested by loading 50 μl onto a homemade pepsin column maintained at 0°C, where pepsin was immobilized by coupling to POROS 20 AL support (Applied Biosystems) and packed into a column housing of 2 mm × 2 cm (64 μl) (Upchurch) (*69*). The protease-generated fragments were then collected onto a TARGA C8 5 μM Piccolo HPLC column (1.0 × 5.0 mm, Higgins Analytical) and separated on a C8 analytical column using a shaped 10 to 45% Buffer B gradient at 8 μl/min (Buffer A: 0.1% formic acid; Buffer B: 0.1% formic acid, 99.9% acetonitrile). The effluent was electrosprayed into the mass spectrometer. Peptides were identified from nondeuterated samples by tandem mass spectrometry (MS/MS) (Thermo Q Exactive), by analyzing MS/MS data using SEQUEST Proteome Discoverer (ThermoFisher). Peptide identification was performed separately for WT TDP-43 and TDP-43^{5FL}. Deuterated samples, and additional nondeuterated reference samples, were analyzed by MS (Thermo Q Exactive or Thermo Exactive Plus EMR).

HDExaminer software was used to process and analyze the HXMS data. The time points for samples performed at pH 6.0 were input as one-tenth of the actual on-exchange time. ExMS2, a MATLAB-based program, was used to prepare the peptide pool used by HDExaminer, from the SEQUEST output files for MS/MS data analysis. HDExaminer uses a nondeuterated sample as the reference for identifying deuterated peptides. Manual adjustment of retention times and m/z windows was performed as needed to correct any initial errors. Each deuterated peptide is corrected for back exchange after quenching, by normalizing to the maximal deuteration of that peptide as detected in the fully deuterated sample. For calculating the peptide deuteration at each time point, HDExaminer identifies the peptide envelope centroid values for both the nondeuterated and deuterated peptides.

HXMS data visualization

For visualizing the difference in peptide deuteration for each peptide, the HDExaminer data were visualized using MATLAB. At each time point, the average deuteration percent for a peptide in either the free or bound condition was calculated by taking the average deuteration percent of all replicates for the peptide at that time point that were identified with medium or high confidence. These values were then analyzed in MATLAB by subtracting the average deuteration percent of the peptide in the Clip34-bound state from the average deuteration percent of the peptide in the free state. These data are plotted in MATLAB according to the colors shown in the color legends in the figures (as in Fig. 2). Peptides of the same sequence but different charge states are plotted to allow visualization of the agreement across separate charge states for a specific peptide sequence.

To generate plots of consensus exchange difference for each time point, the exchange differences of the peptides at that time point were manually analyzed, with the consensus exchange difference determined based on the average classification of all peptides including a specific residue. This was done via a scoring system, where a peptide with a difference of less than 10% receives a score of 0, a peptide with a difference of ≥10% (light blue according to legend) receives a score of −1, a peptide with a difference of ≥20% (medium blue) receives a score of −2, a peptide with a difference of ≥30% (dark blue) receives a score of −3, a peptide with a difference of ≤−10% (light red) receives a score of +1, a peptide with a difference of ≤−20% (medium red) receives a score of +2, and a peptide with a difference of ≤−30% (dark red) receives a score of +3. As peptides were binned according to this scoring system, the displayed consensus percentage differences in exchange do not report the exact value of the percentage difference for each peptide, and do not report the proximity of each peptide's behavior to the cutoff value for each score. The average score for each residue was rounded to the nearest whole number, and these data were plotted in GraphPad Prism, with the rounded score value for each residue colored according to the same scoring system as described for the manual analysis above.

To generate plots of HX data for representative peptides displaying exchange as the number of deuterons, the HDExaminer output of these data was visualized using GraphPad Prism. For a peptide, the values for the number of deuterons from HDExaminer was taken for each replicate with high or medium confidence at each time point, for both free and bound states. This was then plotted in GraphPad Prism.

To generate plots of mass spectra, HDExaminer output was visualized in GraphPad Prism. The raw mass spectrum data for a particular replicate of a specific time point in either the free or bound state were copied into GraphPad Prism. These data were manually analyzed to determine the signal that corresponded to the desired peptide, based on the signal corresponding to the appropriate m/z values. All signal is displayed in the mass spectra plots, but the signal determined to correspond to the correct peptide is colored red, for ease of visualization. Dashed guidelines for visualization are also displayed, with the blue line corresponding to the value of the monoisotopic peak for that peptide, and the purple line corresponding to the centroid value of the peptide in the fully deuterated condition. Representative spectra for each state at each time point were chosen by determining the average value of the centroid for all replicates with peptides of high or medium confidence, for that state and time point. The spectrum displayed as the representative spectrum corresponds to the replicate with the centroid value closest to the average of these centroid values.

Simulation system preparation

The all-atom model of full-length and ΔNTD TDP-43 in complex with RNA was constructed using MODELLER, based on multiple experimentally resolved structures (for NTD PDB: 5MDI, for RRM1/2 PDB:4BS2, for CTD PDB:2N3X) and a well-tempered ensemble for the PrLD generated in our previous work (70) as templates. To create the TDP-43^{5FL} construct, five Phe residues (positions 147, 149, 194, 229, and 231) were mutated to leucine using the "swapaa" module in ChimeraX. The resulting structures were solvated using GROMACS v2022.5. Specifically, the initial model was placed in an octahedral simulation box (l = 15.0 nm for FL TDP-43 and l = 14 nm for TDP-43$^{\Delta NTD}$) and solvated with explicit water molecules. Na$^+$ and Cl$^-$ ions were added to achieve a salt concentration of 100 mM, along with additional counterions to ensure overall charge neutrality.

MD simulations used AUG12 RNA, a 12-nt sequence derived from TDP-43 CLIP data and designed by Lukavsky *et al.* (17), rather than Clip34. Because experimental data show that neither the NTD nor PrLD directly involve RNA binding, the 12-nt sequence captures the essential RRM-RNA interactions, and we determined that AUG12 inhibits TDP-43 aggregation, this sequence is sufficient to investigate allosteric regulation upon RRM binding.

Selection of protein and RNA force fields

Proteins were modeled using the Amber03ws force field with TIP4P/2005 water and improved ion parameters from Luo and Roux (71). This force field was chosen for its optimized protein-water interactions that prevent artifactual compaction in intrinsically disordered regions (72, 73). RNA was modeled using the χOL3 force field with refined glycosidic torsions (74), adjusted phosphate oxygen radii (75), and scaled RNA-water interactions to address known RNA simulation artifacts including unrealistic ladder-like structures and overestimated electrostatic interactions. Force field compatibility was validated in our prior work (76).

Simulation protocol

The solvated protein systems were first subjected to energy minimization using the steepest descent algorithm in GROMACS (77). This was followed by an initial configuration relaxation, consisting of a 100 ps NVT equilibration using the V-rescale thermostat (78) at a 2 fs time step, and an additional 100 ps NPT equilibration using the Parrinello–Rahman barostat (79) with isotropic coupling and a pressure relaxation time of 5 ps. After equilibration, the topology(.top) and coordinate(.gro) files generated by GROMACS were converted into AMBER-compatible input formats (.parm7 and .rst7) using the ParmEd module in AmberTools22 (80). To enable a 4 fs time step during production runs, hydrogen atom masses were increased to 1.5 amu (81).

Production simulations were performed in AMBER22 under constant pressure (1 bar) and temperature (300 K) conditions (80). Temperature was maintained using Langevin dynamics with a friction coefficient of 1 ps^{-1}, and pressure was controlled using a Monte Carlo barostat with isotropic coupling (relaxation time of 1.0 ps) (82). Short-range non-bonded interactions were calculated with a cutoff of 0.9 nm, and long-range electrostatic interactions were treated using the particle mesh Ewald (PME) method (83). All bonds involving hydrogen atoms were constrained using the SHAKE algorithm (84).

Sedimentation analysis

At the end time point of in vitro TDP-43 aggregation prevention assays ($t = 16$ hours), a portion of select conditions was transferred to a tube. Tubes were spun at 21,300 rcf for 10 min at RT to sediment the pellet. The supernatant was transferred to a fresh tube. The pellet was resuspended in assay buffer of equal volume. Equal volumes of supernatant from multiple conditions were then run on SDS-PAGE gels. To determine the relative amounts of protein in the supernatant, Image Studio Lite was used to quantify the TDP-43 band signal for supernatant samples for each condition.

In vitro TDP-43 condensate reversal assay

TDP-43 was thawed on ice and centrifuged for 10 min at 16,000 rcf at 4°C. TDP-43 and TEV protease were diluted into PS buffer (150 mM NaCl, 20 mM HEPES-NaOH pH 7.4, 1 mM DTT), then mixed and incubated at RT for 75 min (reaction concentrations: 4.22 μM TDP-43, 150 mM NaCl, 20 mM HEPES-NaOH pH 7.4, 1 mM DTT, 10.56 μg/ml TEV protease). Portions of solution were then transferred to wells of a ultraviolet (UV)–transparent half-area 96-well plate (Greiner) or a glass slide, and allowed to settle. After 15 additional minutes (90 min total incubation), the preaddition sample on the slide was imaged by brightfield microscopy with 100x objective (EVOS M5000). The solution in the 96-well plate was scanned once at 350 nm in a BMG Labtech plate reader (CLARIOstar Plus), then RNA or buffer was added to the solution in the wells or tubes for final concentrations of 0 or 2 μM RNA, 4 μM TDP-43, 150 mM NaCl, 20 mM HEPES-NaOH pH 7.4, 1 mM DTT, 10 μg/ml TEV protease. Turbidity was then measured at 350 nm once per minute for 60 min at 25°C. After 1 hour of incubation, samples in tubes were imaged by brightfield microscopy with 100x objective (EVOS M5000). For quantification of the turbidity data, preaddition readings at $t = 0$ were standardized by subtracting the turbidity value of a sample of PS buffer alone. For each condition, values were then normalized to set the value at $t = 0$ to 100 for each condition.

In vitro TDP-43 disaggregation assay

TDP-43 was thawed on ice and centrifuged for 10 min at 21,300 rcf at 4°C. TDP-43 was buffer exchanged into 166.66 mM NaCl, 22.22 mM HEPES-NaOH pH 7.0, 1.11 mM DTT (BIO-RAD Micro Bio-Spin Chromatography Columns, following manufacturer's instructions) and concentration was determined via NanoDrop, $e_{280} = 114250\ \mathrm{cm}^{-1}\ \mathrm{M}^{-1}$. TDP-43 was diluted into buffer and RNase-free water to achieve a final concentration of 4 μM TDP-43, 150 mM NaCl, 20 mM HEPES-NaOH pH 7.0, 1mM DTT. TEV protease was added at a final concentration of 7.5 μg/ml. A Safire2 Tecan plate reader was used to assess turbidity once per minute at 395 nm in a nonbinding 96-well plate (Greiner) over 4 hours at ~25° to 30°C. After 4 hours, turbidity readings were paused. RNA (or water for controls without RNA) was added to samples, resulting in final concentrations of 40 μM RNA (for samples with RNA), 3.648 μM TDP-43, 136.8 mM NaCl, 18.24 mM HEPES-NaOH pH 7.0, 0.912 mM DTT. Turbidity readings in the Tecan plate reader were resumed for an additional 16 hours after addition of RNA or water. Sedimentation was performed at the end time point of the assay, as described above. At the end time point of the assay, samples were also prepared for electron microscopy.

Transmission electron microscopy

300-mesh carbon-coated copper grids (Electron Microscopy Sciences) were glow-discharged. 5 μl of sample from the end time point of disaggregation assays was added to the grid and incubated for 40 s. Grids were blotted dry with filter paper. 5 μl of 1% uranyl acetate was added to the grid, then immediately blotted dry with filter paper. Grids were then stored at RT until imaging. Samples were viewed and imaged using a JEOL JEM-1011 electron microscope. Quantification of electron micrographs was performed with ImageJ. The image scale in pixels per μm was set based on the scale bar. Images were inverted to have dark backgrounds, then thresholded to determine regions of interest (ROIs) corresponding to aggregates. Particle analysis was constrained to particles ≥2 pixels. ROIs definitively corresponding to the scale bar and any broken remnants of grid were manually excluded from the quantification calculations. Quantification was reported as the values determined for each micrograph, with four to six micrographs of the same magnification quantified per condition. Parameters measured per micrograph were the average size of aggregates in square micrometers, the percentage of micrograph area occupied by aggregates, and the average integrated density of aggregates.

NMR data collection and processing

All NMR experiments were heteronuclear single quantum coherence (HSQC) spectra conducted on Bruker Avance 600 MHz ^{1}H Larmor frequency spectrometers with HCN TCI z-gradient cryoprobe at 298K. TDP-43 RRMs NMR samples contained 50 μM protein in 20 mM KP_i pH 6.8, 1 mM DTT, 5% D_2O (v/v). NMR samples of RRMs with RNA included 100 μM (2x molar equivalent) RNA. Backbone chemical shift assignments were transferred from BMRB deposited data (BMRB ID 27613). NMR data were processed and analyzed with Bruker TopSpin, NMRPipe (*85*), and CCPNMR (*86*). Chemical shift perturbations were quantified by comparison of the ^{1}H–^{15}N cross-peak measurements in the RNA-containing and RNA-free HSQCs. Intensity ratios were calculated from the intensity of the ^{1}H–^{15}N cross-peaks with the formula I/I_o where I is the RNA-containing sample and I_o is the RNA-free control sample.

G-quadruplex RNA annealing

RNA was thawed on ice. RNA was diluted to achieve working concentrations of 20 μM RNA, 150 mM NaCl, 20 mM HEPES-NaOH pH 7.0, 1 mM DTT. RNA was then annealed in a polymerase chain reaction (PCR) machine by heating at 95°C for 2 min, followed by decreasing temperature at a rate of 1°C per minute, until reaching RT. RNA was added to the desired assay within a maximum of 30 min after the end of the annealing process.

Circular dichroism

RNA was first prepared as described in the “G-quadruplex RNA annealing” section. RNA was then diluted to achieve a final concentration of 5 μM RNA, 150 mM NaCl, 20 mM HEPES-NaOH pH 7.0, 1 mM DTT. The absorbance spectra were recorded in a 1 mm pathlength cuvette at 25°C with an Aviv Circular Dichroism Spectrometer, Model 202. Parameters for measuring the spectra were a measurement range of 220 to 320 nm, a bandwidth of 2 nm, a wavelength step of 2 nm, and an averaging time of 60 s. Data were standardized by subtracting the absorbance spectrum of the blank. The standardized data were then normalized using the equation: $\Delta\varepsilon(M^{-1}\,cm^{-1}) = \theta/(32980 \times c \times l)$, where θ is the reported CD signal in millidegrees, c is the RNA molar concentration, and l is the pathlength in centimeters.

HEK293 cell oligonucleotide treatment

Glass bottom 24-well plates were coated with 50 μg/ml collagen overnight. OptoTDP-43 stable HEK293 cells were plated at either 150,000 cells per well for imaging, or 1,000,000 cells per well in 6-well plates for Western blot analysis, in DMEM (Fisher Scientific) with 10% BGS (Hyclone; Fisher Scientific) and 1% Glutamax (Thermo Fisher). 16 hours after plating, optoTDP-43 expression was induced by media change to phenol-free DMEM/10%BGS/1%Glutamax with 750 ng/ml (for imaging) or 1000 ng/ml (for Western blot) doxycycline-hyclate. Immediately after the media change, oligo treatments were started. 2’OMe_RNA oligos were transfected using lipofectamine RNAiMAX according to manufacturer’s instructions (Invitrogen). Briefly, 500 nM of each oligo was diluted in OptiMEM (Thermo Fisher) and mixed with 1 μl lipofectamine per well, incubated at RT for 10 min, and added dropwise to the cells. Plates were loosely wrapped in aluminum foil to prevent light exposure and subsequent light-induced TDP-43 oligomerization. 43 hours after doxycycline-hyclate induction, plates were removed from the foil and placed on an LED array (Amuza) for blue light stimulation (465 nm) for 5 hours at 37°C. After blue light stimulation, cells were pelleted for downstream protein analysis, or for imaging cells were washed once with phosphate-buffered saline (PBS) and fixed with 4% paraformaldehyde (PFA) (in PBS) for 20 min at RT. Cells were permeabilized in 0.3% Triton X-100 in PBS and stained with Hoechst (1:1000; Thermo Fisher) overnight.

HEK293 cell imaging and analysis

Image acquisition was performed using a Nikon Eclipse Ti2 Inverted Microscope with a 40X air objective. 20 fields of view (FOVs) were randomly selected by the NIS-Elements software per well. All image visualization and quantification were performed using NIS-Elements AR1 Analysis 4.51. The microscopy images were collected across three independent experiments and maximum intensity projection images were used for analysis. Binary thresholds (594 nm and 405 nm channel) and spot detection were used to capture and separate nuclei and puncta objects. Puncta overlapping with the nuclear signal were removed from the analysis, leaving only cytoplasmic puncta for quantification. Puncta area (square micrometers) was divided by nuclei count and expressed as puncta area per cell. Puncta area/cell was normalized against the average value for the control (CTR) oligo. Out-of-focus images were removed, and FOVs with mean puncta area >100 μm^2/cell were excluded and considered outliers. Twenty FOVs were analyzed per well, and at least two to three wells were imaged per experiment. Mean values per experiment were normalized to control oligonucleotide treatment and considered a biological replicate, and the mean values of three biological replicates ($n = 3$ experiments) were used to analyze the effect of the oligonucleotide.

Stable HEK293 CUTS cell line

Stable HEK293 cells expressing CUTS were generated as previously described (*47*). Briefly, HEK293 cells were seeded in 6-well plates and transfected at roughly 70% confluency with 2.5 μg of PiggyBac plasmids encoding CUTS along with 0.5 μg of a Super PiggyBac Transposase Expressing plasmid (PB200PA-1), using Lipofectamine 3000 (Invitrogen) as per the manufacturer’s instructions. A control group lacking the transposase plasmid was included. After 48 hours, cells were subjected to selection with 5 μg/ml puromycin (Sigma, P8833), with media being refreshed every 2 days. Nontransfected control cells typically died within 5 days under selection. Surviving cells were expanded and cultured in media containing a reduced puromycin concentration (2.5 μg/ml) to establish stable cell lines. Successful transgene expression was validated through live imaging.

Live confocal microscopy of HEK CUTS cell line

Live-cell imaging was carried out using a Nikon A1 laser-scanning confocal microscope equipped with a 10X objective lens. Environmental conditions during imaging were maintained using a Tokai HIT stage-top incubator. Images were acquired and analyzed using Nikon Elements software. Representative images were selected from a minimum of three independent experiments to ensure reproducibility.

siRNA reverse transfection and RNA oligonucleotide transfection of HEK CUTS cell line

siRNA-mediated gene knockdown was performed via reverse transfection using Lipofectamine RNAiMAX reagent (Invitrogen, 13778150), following the manufacturer’s instructions. To reduce TDP-43 expression, ON-TARGETplus SMARTpool siRNA targeting *TARDBP* (Dharmacon, L-012394-00-0005) was used. Nontargeting siRNA (Dharmacon, D-001206-13-05) served as a control in these experiments. RNA oligonucleotide transfections were performed using Lipofectamine RNAiMAX reagent (Invitrogen) in accordance with the manufacturer’s protocol.

Detergent solubility assay

The detergent solubility assay was performed as previously described (*14*). In brief, cells were collected in RIPA buffer, incubated on ice for 10 min, and sonicated. Samples were centrifuged at 100,000 rcf for 1 hour at 4°C. The supernatant was collected and labeled as the detergent-soluble fraction. Protein concentrations were determined using Pierce BCA protein assay (Thermo Fisher). The remaining pellet was resuspended in RIPA buffer, briefly sonicated, and centrifuged at 100,000*g* for 30 min at 4°C. Supernatant was removed, and the remaining cell pellet was resuspended in urea buffer, sonicated, and centrifuged at 100,000 rcf for 1 hour at RT. The final supernatant was collected as the detergent-insoluble, urea-soluble fraction. Protein from each fraction was separated using SDS-PAGE and analyzed by Western blot analysis.

SDS-PAGE and Western blotting

Protein samples were prepared in 4x Laemmli buffer (BIO-RAD) with β-mercaptoethanol and boiled at 95°C for 10 min. Precision Plus Protein Western C ladder (BIO-RAD) and samples were separated via SDS-PAGE (4 to 20% Mini-PROTEAN TGX precast gels, BIO-RAD) and transferred to nitrocellulose membranes (BIO-RAD) at 10 V for 90 min in mini-gel tanks (Invitrogen). Membranes were then incubated in Ponceau for 10 min and imaged. Membranes were washed and blocked for 1 hour at RT in 5% milk in TBST, then incubated with primary antibody overnight at 4°C. After TBST washes, membranes were incubated at RT for 1 hour with secondary antibody and streptactin HRP-conjugate (BIO-RAD 1:10000). All Western blot images were taken on the GE Amersham ImageQuant 800. Membranes were stripped for 10 min (Restore PLUS Western blot stripping buffer; Thermo Fisher) and reblotted as needed.

Primary antibodies included: mCherry 1C51 (mouse; Novus Biologicals, Cat: NBP1-96752; 1:1000; RRID: AB_11034849); TDP-43 (rabbit; Proteintech, Cat: 10782-2-AP; 1:2500; RRID: AB_615042); GAPDH (mouse; Proteintech, Cat: 60004-1-IG; 1:10000; RRID: AB_2107436). Secondary antibodies included: Donkey Anti-Mouse IgG (H+L)-HRP Conjugate (Invitrogen, Cat: SA1100; 1:10000); Goat Anti-Rabbit IgG (H+L)-HRP Conjugate (Jackson Immuno Research, Cat: 111035046; 1:10000).

iPSC-derived neuron treatment and immunostaining

RNA treatments started on day 13 after plating (DIV27) and lasted 24 hours. RNAs were transfected using Lipofectamine RNAiMAX (Invitrogen) according to the manufacturer's instructions. Briefly, each RNA was diluted in OptiMEM (Gibco) and combined with 1 μl Lipofectamine per well, also diluted in OptiMEM. The mixture was incubated at RT for 10 min, and then added dropwise to the cells with each RNA at a final concentration of 500 nM. Neurons were fixed 24 hours after RNA treatment on day 14 after plating (DIV28).

On DIV28, cells were washed once in PBS (Gibco) and fixed in 4% PFA (Electron Microscopy Sciences) immediately after treatments ended. Cells were kept in PFA for 20 min, then washed three times in PBS and blocked with 5% Donkey Serum (Jackson ImmunoResearch) + 0.3% TX-100 (Sigma-Aldrich) in PBS for 30 min at RT. Primary antibodies (goat MAP2 1:1000, Phosphosolutions 1099, RRID: AB_2752241; rabbit TDP-43 1:300, Proteintech 10782-2-AP, RRID: AB_615042) were diluted in blocking solution and incubated overnight at 4°C. Secondary antibodies (donkey Alexa Fluor, Jackson ImmunoResearch) were used at 1:1000 dilution in blocking solution and incubated for 60 min at RT. All treatments and cell lines were treated and probed simultaneously to decrease variability. Coverslips were mounted on slides using Prolong Glass mounting media (Invitrogen).

Images were acquired (20 per group) using an A1R Nikon Confocal Microscope and FOVs were processed for analyses using Nikon NIS Elements Software. Settings were kept consistent across treatments. Within each FOV, neurons that were isolated (not over glial cells or other neurons) were selected and nuclear TDP-43 signal was measured by overlaying an ROI using 4′,6-diamidino-2-phenylindole (DAPI) as a guide. Cytosolic area was hand-drawn using MAP2 signal as a guide. Raw intensity values for nuclear signal in the 488 channel (TDP-43) were normalized against cytosolic intensity values and the output was referred to as "nuclear/cytosolic ratio."

For analysis of neuritic puncta, a Cy5-labeled Malat1_start and CTR oligo were used at the same concentration and timing as described above. We used Staufen-1, another RBP, as a control to assess possible interactions between TDP-43 and Malat1_start. Staufen-1 antibody was from Proteintech (14225-1-AP; RRID: AB_2302744) and was used at a 1:300 dilution. After imaging, Malat1_start and CTR oligo puncta were detected using ROI autodetection on NIS-Elements. Pearson coefficient between Malat1_start/CTR oligo and either TDP-43 or Staufen-1 was calculated for each ROI, and we considered Pearson ≥ 0.5 as colocalizing. The number of total Malat1_start, CTR oligo, TDP-43, and Staufen-1 puncta were expressed as puncta/100 μm, same as the number of puncta within each group with Pearson ≥ 0.5. Values were graphed as the average of 20 to 25 neurites in four technical replicates of the same lines.

Sodium arsenite treatment and immunofluorescence

Control iPSC-derived MNs were plated on coverslips at a density of 150,000 cells per well. On DIV27 cells received either no treatment (NT), CTR RNA, or Malat1_start RNA. RNAs were delivered at a concentration of 500 nM with RNAiMAX Lipofectamine. On DIV28, 22 hours after the RNA treatments, neurons were exposed to 250 μM sodium arsenite for 2 hours. Cells were then fixed in 4% PFA, washed three times in PBS, blocked in 0.3% TX-100 + 5% Normal Donkey Serum in PBS, and incubated overnight at 4°C in primary antibodies diluted in blocking solution at the following concentrations: TDP-43 (Proteintech 10782-2-AP; RRID: AB_615042) at 1:300; G3BP1 (Santa Cruz sc-365338; RRID: AB_10846950) at 1:100; MAP2 (PhosphoSolutions 1099-MAP2; RRID: AB_2752241) at 1:1000. Coverslips were then washed in PBS and incubated in secondary antibodies (Jackson ImmunoResearch) at a concentration of 1:1000 in blocking solution for 90 min at RT, then washed in PBS three times and mounted on glass slides with Prolong Glass with NucBlue mounting media (Invitrogen P36983). Images were acquired on a confocal Nikon A1R confocal microscope.

Reverse transcription PCR (RT-PCR)

Total RNA from differentiated iPSC-derived motor neurons was extracted using the RNeasy Mini Kit (Qiagen, 74106) according to the manufacturer's instructions. RNA concentration and purity were assessed with a NanoDrop ND-1000 spectrophotometer (Thermo Fisher). cDNA was synthesized from total RNA using the iScript Reverse Transcription Supermix (BIO-RAD, 1708841). RT-PCR was conducted on 5 ng of RNA per reaction. Primers used to detect *KCNQ2* cryptic splicing: *KCNQ2-CE-F*, 5′-TATGCCCACAGCAAGATCAC-3′; *KCNQ2-CE-R*, 5′-AGACACCGATGAGGGTGAAG-3′. As a loading control, 18S was amplified using the following primers: 18S-FWD 5′ GCAGAATCCACGCCAGTACA and 18S-REV 5′ TTCACGGAGCTTGTTGTCCA. For *STMN2* we used previously described primers (87); we ran the full length transcript using the following primers: *STMN2-F*, 5′- AGCTGTCCATGCTGTCACTG-3′; *STMN2-R*, 5′- GGTGGCTTCAAGATCAGCTC -3′ and its truncated version: *STMN2a-F*, 5′- GGACTCGGCAGAAGACCTTC -3′; *STMN2a-R*, 5′- GCAGGCTGTCTGTCTCTCTC-3′, and values were normalized against β-actin *ACTB-F*, 5′-TTGTTACAGGAAGTCCCTTGCC-3′; *ACTB-R*, 5′-ATGCTATCACCTCCCCTGTGTG-3′. For RT-PCR, PCR products were amplified by Quick-Load Taq 2X Master Mix (NEB, M0271L) using the following PCR program in S1000 Thermal Cycler (BIO-RAD): 95°C for 30 s, followed by 40 cycles of 95°C for 15 s, 55°C for 30 s, 68°C for 30 s and extension time of 68°C for 5 min. PCR products were separated by agarose gel electrophoresis, and the bands were visualized with Amersham ImageQuant 800 GxP biomolecular imager system. Band intensity was quantified using ImageLab from BIO-RAD.

Virus production

AAV9 virus was generated by Vector Biolabs using a plasmid designed as follows. The CMV-promoter driven pcDNA3.2 TDP-43 NLS1 YFP plasmid, a gift from Aaron Gitler (Addgene plasmid no. 84912; RRID:Addgene_84912) (58), was packaged into AAV9 viral particles.

Intraspinal delivery of AAV9 virus

Intraspinal delivery of AAV9 in p180 mice was carried out as previously described (57). Mice deeply under anesthesia underwent an incision of their dorsal skin and underlying muscle with retraction, revealing the spinous processes between vertebrae C2 and T1. After laminectomy at spinal levels C4, C5, and C6, six total bilateral injections were given across this area. Each injection contained 1×10^{11} GC of the AAV9-TDP-43 NLS1 virus (TDP-43$^{\Delta NLS}$) in a 1 μl total volume. A gas-tight Hamilton syringe mounted on a UMP3 electronic micropump (World Precision International) was used for these injections, with a 33-gauge 45° beveled needle. Targeting of injections was guided on the lateral axis by the midpoint of each spinal segment, and on the rostral-caudal axis by the location of dorsal root entry for C4, C5, and C6. The needle was lowered to a depth 0.8 mm below the dorsal surface for ventral horn targeting, with injections then delivered over a 5-min interval at a constant rate. Sham surgery control animals underwent identical procedures and laminectomies, as well as needle placement and insertion. In sham animals, the Hamilton syringe was filled with sterile PBS and the micropump was not initiated. After the final injection, the dura was removed from the dorsal spinal cord of the injection region, and a nonadhering dressing (Adaptic nonadhering dressing by Systagenix) was applied. Overlying muscles were then closed in layers, using sterile silk sutures. The skin incision was also closed using both sutures and sterile wound clips. Animals recovered on a heating pad until awake, and were then returned to their home cage. To minimize pain and distress, at the time of surgery and at 12-hour intervals for the first 24 hours after surgery, animals were given subcutaneous sterile saline for fluid balance, buprenorphine analgesic (0.05 mg/kg), and cefazolin antibiotic (10 mg/kg). Animals were monitored daily and were checked for signs of pain and/or distress, as well as ambulatory potential and ability to obtain food/water.

Spinal delivery of RNA

After 1 week of viral expression, animals were again deeply anesthetized. The original surgical incision was reopened and skin and muscle retracted to expose the spinal cord. The nonadhering dressing was removed from the spinal cord surface, and was replaced with a presaturated gelfoam sponge (sterile gelfoam dental sponge, Pharmacia and Upjohn). TDP-43$^{\Delta NLS}$-expressing animals were randomized into saline control, or RNA treatment groups, with the sponge being presoaked either in sterile saline solution, or sterile saline reconstituted RNA at a 100 μg/mouse dosing. This dosing penetrates to the ventral spinal cord by 3 days postapplication in a robust and reproducible manner, and causes no detrimental side effects when evaluated out to 2 weeks postadministration. Sham surgery control animals underwent identical procedures, and received a saline-saturated gelfoam sponge. After this application, overlying muscles and skin were again closed with sterile silk sutures, with the skin also being bound with sterile wound clips. Animals again recovered on a heating pad until awake, before return to home cages. Animals received the same set of compounds to minimize pain and distress, at the time of surgery and at 12-hour intervals for the first 24 hours after surgery: subcutaneous sterile saline for fluid balance, buprenorphine analgesic (0.05 mg/kg), and cefazolin antibiotic (10 mg/kg). Animals were again monitored daily for signs of pain and/or distress, as well as ambulatory potential and ability to obtain food/water. Assessment of motor neuron numbers was carried out at 3 and 5 days after RNA application, to determine potential beneficial therapeutic effects and longevity.

Animal harvesting for spinal cord immunofluorescence

Mice were euthanized using carbon dioxide asphyxiation, and perfused and fixed following standard laboratory procedures. A perfusion needle connected to a peristaltic pump was inserted into the left ventricle of the heart, and animals were then perfused with ~20 ml of PBS followed by 25 ml 4% PFA. The animal was dissected to obtain the cervical spinal cord, which was then placed in 4% PFA overnight. PFA was briefly rinsed off the tissue with PBS, with spinal cords then placed in 30% sucrose until tissue sinking (24 to 48 hours). Spinal cords were frozen into Tissue-Tek OCT solution and were subsequently sectioned using a Cryostar NX50 cryostat (Epredia) at a section depth of 30 μm. Sections were placed onto charged glass slides. Tissue blocking, permeabilization, and staining were performed according to laboratory standard protocols and according to antibody manufacturer recommendations. 30 μm spinal cord sections on slides were heated overnight at 55°C and were then rinsed with PBS. Sections were next blocked in 5% BSA for 1 hour at RT and then incubated in primary antibodies at 4°C overnight (NeuN) or for 48 hours (ChAT). Primary antibodies included: anti-ChAT (Millipore RRID:AB_2079751, 1:1,000) and anti-NeuN (Cell Signaling catalog no. 24307, RRID:AB_2651140, 1:400). After this incubation and PBS washing, secondary labeling for visualization was attained with AlexaFluor594 (Life Technologies). To label cell nuclei, Hoechst stain (ThermoFisher) was used. Slides were mounted with coverslips using Citifluor AF3 (Electron Microscopy Sciences). Microscopy imaging was accomplished using a Nikon A1+ confocal microscope and NIS-Elements software. ChAT$^+$ and NeuN$^+$ cells were assessed using bilateral ventral horn images with manual counting by a blinded assessor. TDP-43 puncta, visualized using the YFP tag of the virally expressed protein, and colocalization of these puncta with Cy5-tagged Malat1_start molecules were assessed using NIS-Elements software.

RT-qPCR analysis of *Sort1* transcripts

RNA was extracted from fixed mouse spinal cords using the Thermofisher PureLink RNA Mini Kit. Reverse transcription was accomplished using the Qiagen QuantiTech Reverse Transcription Kit. cDNA samples were then prepared for qPCR assessment using SYBR Green qPCR master mix from Thermofisher, and were evaluated using the QuantStudio 5 Real-Time PCR System. Samples were measured in triplicate for each transcript of interest, with data normalized to *GAPDH* transcript expression. The ratio of the misspliced variant (*Sort1-ex17b*) to *Sort1-WT* transcripts is graphically represented, as has been reported in previous studies (*43*, *59*). Fold change between groups for total *Sort1* is also represented.

The previously described and validated primer pairs for total, WT, and TDP-43 misspliced (*Sort1-ex17b*) mouse *Sort1* transcripts (*43*, *59*) were obtained from Integrated DNA Technologies (IDT). Primer pairs are as follows: Sort1_Total fwd: CGTGTTCCCTGGAGGACTTCCT; Sort1_Total rev: TTCAGGCTGCTCCACGCACT; Sort1_WT fwd: CCCCACAAAGCAGAATTCCAAGTC; Sort1_WT rev: TGACAAGCATCAGTCCCACGAT; Sort1_ex17b fwd: AAATCCCAGGAGACAAATGC; Sort1_ex17b rev: GAGCTGGATTCTGGGACAAG; GAPDH fwd: AACAGCAACTCCCACTCTTC; GAPDH rev: CCTGTTGCTGTAGCCGTATT.

Animal data analysis considerations

Animals were numbered according to surgery order and were randomized into treatment groups. Counting of motor neuron numbers was performed by a second, blinded individual. All surgical animals were considered for inclusion and assessment based on confirmation of YFP fluorescence in spinal cord motor neurons. No animals reached IACUC-based endpoint criteria for early euthanasia and study exclusion. All 10 animals per time point per group were considered.

Quantification and statistical analysis

All statistical details of experiments can be found in the figure legends. Data visualization and statistical analyses were performed with GraphPad Prism (GraphPad Software Inc.; La Jolla, CA, USA). Quantification of gel images was performed with Image Studio Lite (LI-COR Biosciences; Lincoln, NE, USA). Quantification of micrographs was performed with ImageJ (National Institutes of Health; Bethesda, Maryland, USA). HX analysis was performed with HDExaminer (Trajan Scientific and Medical; Melbourne, Australia). MATLAB was used for some HX data visualization (MathWorks; Natick, MA, USA). ExMS2, a MATLAB-based tool, was used to prepare the peptide pool for HX (*88*). Immunofluorescence analysis was performed using NIS-Elements (Nikon; Minato City, Tokyo, Japan).

REFERENCES AND NOTES

1. A. F. Harrison, J. Shorter, RNA-binding proteins with prion-like domains in health and disease. *Biochem. J.* **474**, 1417–1438 (2017). doi: 10.1042/BCJ20160499; pmid: 28389532
2. B. Portz, B. L. Lee, J. Shorter, FUS and TDP-43 Phases in Health and Disease. *Trends Biochem. Sci.* **46**, 550–563 (2021). doi: 10.1016/j.tibs.2020.12.005; pmid: 33446423
3. A. Meneses *et al.*, TDP-43 Pathology in Alzheimer's Disease. *Mol. Neurodegener.* **16**, 84 (2021). doi: 10.1186/s13024-021-00503-x; pmid: 34930382
4. P. T. Nelson *et al.*, Limbic-predominant age-related TDP-43 encephalopathy (LATE): Consensus working group report. *Brain* **142**, 1503–1527 (2019). doi: 10.1093/brain/awz099; pmid: 31039256
5. R. Nicks *et al.*, Repetitive head impacts and chronic traumatic encephalopathy are associated with TDP-43 inclusions and hippocampal sclerosis. *Acta Neuropathol.* **145**, 395–408 (2023). doi: 10.1007/s00401-023-02539-3; pmid: 36681782
6. D. Arseni *et al.*, TDP-43 forms amyloid filaments with a distinct fold in type A FTLD-TDP. *Nature* **620**, 898–903 (2023). doi: 10.1038/s41586-023-06405-w; pmid: 37532939
7. D. Arseni *et al.*, Structure of pathological TDP-43 filaments from ALS with FTLD. *Nature* **601**, 139–143 (2022). doi: 10.1038/s41586-021-04199-3; pmid: 34880495
8. M. Neumann *et al.*, Ubiquitinated TDP-43 in frontotemporal lobar degeneration and amyotrophic lateral sclerosis. *Science* **314**, 130–133 (2006). doi: 10.1126/science.1134108; pmid: 17023659
9. P. R. Mehta, A. L. Brown, M. E. Ward, P. Fratta, The era of cryptic exons: Implications for ALS-FTD. *Mol. Neurodegener.* **18**, 16 (2023). doi: 10.1186/s13024-023-00608-5; pmid: 36922834
10. S. Yang, Z. Lei, J. U. Guo, TDP-43 loss brings RNA to a twist ending. *Nat. Neurosci.* **28**, 2176–2177 (2025). doi: 10.1038/s41593-025-02065-3; pmid: 41120749
11. C. M. Fare, J. Shorter, (Dis)Solving the problem of aberrant protein states. *Dis. Model. Mech.* **14**, dmm048983 (2021). doi: 10.1242/dmm.048983; pmid: 33942880
12. F. Gasset-Rosa *et al.*, Cytoplasmic TDP-43 De-mixing Independent of Stress Granules Drives Inhibition of Nuclear Import, Loss of Nuclear TDP-43, and Cell Death. *Neuron* **102**, 339–357.e7 (2019). doi: 10.1016/j.neuron.2019.02.038; pmid: 30853299
13. L. Guo *et al.*, Defining RNA oligonucleotides that reverse deleterious phase transitions of RNA-binding proteins with prion-like domains. *Mol. Cell* **86**, 114–134.e10 (2026). doi: 10.1016/j.molcel.2025.12.009; pmid: 41512823
14. J. R. Mann *et al.*, RNA Binding Antagonizes Neurotoxic Phase Transitions of TDP-43. *Neuron* **102**, 321–338.e8 (2019). doi: 10.1016/j.neuron.2019.01.048; pmid: 30826182
15. L. McGurk *et al.*, Poly(ADP-Ribose) Prevents Pathological Phase Separation of TDP-43 by Promoting Liquid Demixing and Stress Granule Localization. *Mol. Cell* **71**, 703–717.e9 (2018). doi: 10.1016/j.molcel.2018.07.002; pmid: 30100264
16. X. Yan *et al.*, Intra-condensate demixing of TDP-43 inside stress granules generates pathological aggregates. *Cell* **188**, 4123–4140.e18 (2025). doi: 10.1016/j.cell.2025.04.039; pmid: 40412392
17. P. J. Lukavsky *et al.*, Molecular basis of UG-rich RNA recognition by the human splicing factor TDP-43. *Nat. Struct. Mol. Biol.* **20**, 1443–1449 (2013). doi: 10.1038/nsmb.2698; pmid: 24240615
18. A. E. Conicella *et al.*, TDP-43 α-helical structure tunes liquid-liquid phase separation and function. *Proc. Natl. Acad. Sci. U.S.A.* **117**, 5883–5894 (2020). doi: 10.1073/pnas.1912055117; pmid: 32132204
19. A. E. Conicella, G. H. Zerze, J. Mittal, N. L. Fawzi, ALS Mutations Disrupt Phase Separation Mediated by α-Helical Structure in the TDP-43 Low-Complexity C-Terminal Domain. *Structure* **24**, 1537–1549 (2016). doi: 10.1016/j.str.2016.07.007; pmid: 27545621
20. B. S. Johnson *et al.*, TDP-43 is intrinsically aggregation-prone, and amyotrophic lateral sclerosis-linked mutations accelerate aggregation and increase toxicity. *J. Biol. Chem.* **284**, 20329–20339 (2009). doi: 10.1074/jbc.M109.010264; pmid: 19465477
21. E. Buratti, TDP-43 post-translational modifications in health and disease. *Expert Opin. Ther. Targets* **22**, 279–293 (2018). doi: 10.1080/14728222.2018.1439923; pmid: 29431050
22. T. J. Cohen *et al.*, An acetylation switch controls TDP-43 function and aggregation propensity. *Nat. Commun.* **6**, 5845 (2015). doi: 10.1038/ncomms6845; pmid: 25556531
23. S. Maharana *et al.*, RNA buffers the phase separation behavior of prion-like RNA binding proteins. *Science* **360**, 918–921 (2018). doi: 10.1126/science.aar7366; pmid: 29650702
24. C. J. Sumner, T. M. Miller, The expanding application of antisense oligonucleotides to neurodegenerative diseases. *J. Clin. Invest.* **134**, e186116 (2024). doi: 10.1172/JCI186116; pmid: 39352381
25. C. N. Cook *et al.*, *C9orf72* poly(GR) aggregation induces TDP-43 proteinopathy. *Sci. Transl. Med.* **12**, eabb3774 (2020). doi: 10.1126/scitranslmed.abb3774; pmid: 32878979
26. E. Buratti, F. E. Baralle, Characterization and functional implications of the RNA binding properties of nuclear factor TDP-43, a novel splicing regulator of *CFTR* exon 9. *J. Biol. Chem.* **276**, 36337–36343 (2001). doi: 10.1074/jbc.M104236200; pmid: 11470789
27. X. Zhang *et al.*, Multivalent GU-rich oligonucleotides sequester TDP-43 in the nucleus by inducing high molecular weight RNP complexes. *iScience* **27**, 110109 (2024). doi: 10.1016/j.isci.2024.110109; pmid: 38989321
28. N. Mollasalehi *et al.*, An Allosteric Modulator of RNA Binding Targeting the N-Terminal Domain of TDP-43 Yields Neuroprotective Properties. *ACS Chem. Biol.* **15**, 2854–2859 (2020). doi: 10.1021/acschembio.0c00494; pmid: 33044808
29. M. Hallegger *et al.*, TDP-43 condensation properties specify its RNA-binding and regulatory repertoire. *Cell* **184**, 4680–4696.e22 (2021). doi: 10.1016/j.cell.2021.07.018; pmid: 34380047
30. A. Rizuan *et al.*, Structural details of helix-mediated multimerization of the conserved region of TDP-43 C-terminal domain. *Nat. Commun.* **16**, 10528 (2025). doi: 10.1038/s41467-025-65546-w; pmid: 41298366
31. M. Polymenidou *et al.*, Long pre-mRNA depletion and RNA missplicing contribute to neuronal vulnerability from loss of TDP-43. *Nat. Neurosci.* **14**, 459–468 (2011). doi: 10.1038/nn.2779; pmid: 21358643
32. J. R. Tollervey *et al.*, Characterizing the RNA targets and position-dependent splicing regulation by TDP-43. *Nat. Neurosci.* **14**, 452–458 (2011). doi: 10.1038/nn.2778; pmid: 21358640
33. J. S. Reuter, D. H. Mathews, RNAstructure: Software for RNA secondary structure prediction and analysis. *BMC Bioinformatics* **11**, 129 (2010). doi: 10.1186/1471-2105-11-129; pmid: 20230624
34. S. W. Englander, Hydrogen exchange and mass spectrometry: A historical perspective. *J. Am. Soc. Mass Spectrom.* **17**, 1481–1489 (2006). doi: 10.1016/j.jasms.2006.06.006; pmid: 16876429
35. J. Jumper *et al.*, Highly accurate protein structure prediction with AlphaFold. *Nature* **596**, 583–589 (2021). doi: 10.1038/s41586-021-03819-2; pmid: 34265844
36. M. Aikio *et al.*, Opposing roles of p38α-mediated phosphorylation and PRMT1-mediated arginine methylation in driving TDP-43 proteinopathy. *Cell Rep.* **44**, 115205 (2025). doi: 10.1016/j.celrep.2025.115386; pmid: 39977265
37. S. Agrawal, M. Jain, W. Z. Yang, H. S. Yuan, Frontotemporal dementia-linked P112H mutation of TDP-43 induces protein structural change and impairs its RNA binding function. *Protein Sci.* **30**, 350–365 (2021). doi: 10.1002/pro.3990; pmid: 33151007
38. F. Moreno *et al.*, A novel mutation P112H in the *TARDBP* gene associated with frontotemporal lobar degeneration without motor neuron disease and abundant neuritic amyloid plaques. *Acta Neuropathol. Commun.* **3**, 19 (2015). doi: 10.1186/s40478-015-0190-6; pmid: 25853458
39. H. J. Chen *et al.*, RRM adjacent *TARDBP* mutations disrupt RNA binding and enhance TDP-43 proteinopathy. *Brain* **142**, 3753–3770 (2019). doi: 10.1093/brain/awz313; pmid: 31605140
40. M. Neumann *et al.*, Phosphorylation of S409/410 of TDP-43 is a consistent feature in all sporadic and familial forms of TDP-43 proteinopathies. *Acta Neuropathol.* **117**, 137–149 (2009). doi: 10.1007/s00401-008-0477-9; pmid: 19125255
41. H. Yu *et al.*, HSP70 chaperones RNA-free TDP-43 into anisotropic intranuclear liquid spherical shells. *Science* **371**, eabb4309 (2021). doi: 10.1126/science.abb4309; pmid: 33335017
42. P. Wang, C. M. Wander, C. X. Yuan, M. S. Bereman, T. J. Cohen, Acetylation-induced TDP-43 pathology is suppressed by an HSF1-dependent chaperone program. *Nat. Commun.* **8**, 82 (2017). doi: 10.1038/s41467-017-00088-4; pmid: 28724966
43. J. C. Necarsulmer *et al.*, RNA-binding deficient TDP-43 drives cognitive decline in a mouse model of TDP-43 proteinopathy. *eLife* **12**, RP85921 (2023). doi: 10.7554/eLife.85921.3; pmid: 37819053
44. A. Bhardwaj, M. P. Myers, E. Buratti, F. E. Baralle, Characterizing TDP-43 interaction with its RNA targets. *Nucleic Acids Res.* **41**, 5062–5074 (2013). doi: 10.1093/nar/gkt189; pmid: 23519609
45. C. Y. Chung *et al.*, Aberrant activation of non-coding RNA targets of transcriptional elongation complexes contributes to TDP-43 toxicity. *Nat. Commun.* **9**, 4406 (2018). doi: 10.1038/s41467-018-06543-0; pmid: 30353006
46. C. Jolly *et al.*, Stress-induced transcription of satellite III repeats. *J. Cell Biol.* **164**, 25–33 (2004). doi: 10.1083/jcb.200306104; pmid: 14699086
47. L. Xie *et al.*, CUTS RNA Biosensor for the Real-Time Detection of TDP-43 Loss-of-Function. *eLife* **13**, RP101216 (2024). doi: 10.7554/eLife.101216.2; pmid: 39026766
48. K. Zhang *et al.*, The *C9orf72* repeat expansion disrupts nucleocytoplasmic transport. *Nature* **525**, 56–61 (2015). doi: 10.1038/nature14973; pmid: 26308891
49. A. N. Coyne *et al.*, Nuclear accumulation of CHMP7 initiates nuclear pore complex injury and subsequent TDP-43 dysfunction in sporadic and familial ALS. *Sci. Transl. Med.* **13**, eabe1923 (2021). doi: 10.1126/scitranslmed.abe1923; pmid: 34321318
50. L. Xie *et al.*, Context-dependent Interactors Regulate TDP-43 Dysfunction in ALS/FTLD. bioRxiv 2025.04.07.646890 [Preprint] (2025). doi: 10.1101/2025.04.07.646890
51. V. Casiraghi *et al.*, Modeling of TDP-43 proteinopathy by chronic oxidative stress identifies rapamycin as beneficial in ALS patient-derived 2D and 3D iPSC models. *Exp. Neurol.* **383**, 115057 (2025). doi: 10.1016/j.expneurol.2024.115057; pmid: 39536963
52. B. J. Joseph *et al.*, TDP-43-dependent mis-splicing of *KCNQ2* triggers intrinsic neuronal hyperexcitability in ALS/FTD. *Nat. Neurosci.* **28**, 2476–2492 (2025). doi: 10.1038/s41593-025-02096-w; pmid: 41174170
53. Z. Melamed *et al.*, Premature polyadenylation-mediated loss of stathmin-2 is a hallmark of TDP-43-dependent neurodegeneration. *Nat. Neurosci.* **22**, 180–190 (2019). doi: 10.1038/s41593-018-0293-z; pmid: 30643298
54. S. Seddighi *et al.*, Mis-spliced transcripts generate de novo proteins in TDP-43–related ALS/FTD. *Sci. Transl. Med.* **16**, eadg7162 (2024). doi: 10.1126/scitranslmed.adg7162; pmid: 38277467

55. N. H. Alami *et al.*, Axonal transport of TDP-43 mRNA granules is impaired by ALS-causing mutations. *Neuron* **81**, 536–543 (2014). doi: 10.1016/j.neuron.2013.12.018; pmid: 24507191
56. J. P. Vessey *et al.*, A loss of function allele for murine Staufen1 leads to impairment of dendritic Staufen1-RNP delivery and dendritic spine morphogenesis. *Proc. Natl. Acad. Sci. U.S.A.* **105**, 16374–16379 (2008). doi: 10.1073/pnas.0804583105; pmid: 18922781
57. B. K. Jensen *et al.*, Targeting TNFα produced by astrocytes expressing amyotrophic lateral sclerosis-linked mutant fused in sarcoma prevents neurodegeneration and motor dysfunction in mice. *Glia* **70**, 1426–1449 (2022). doi: 10.1002/glia.24183; pmid: 35474517
58. A. C. Elden *et al.*, Ataxin-2 intermediate-length polyglutamine expansions are associated with increased risk for ALS. *Nature* **466**, 1069–1075 (2010). doi: 10.1038/nature09320; pmid: 20740007
59. M. Prudencio *et al.*, Misregulation of human sortilin splicing leads to the generation of a nonfunctional progranulin receptor. *Proc. Natl. Acad. Sci. U.S.A.* **109**, 21510–21515 (2012). doi: 10.1073/pnas.1211577110; pmid: 23236149
60. J. Gao *et al.*, Translational regulation in the brain by TDP-43 phase separation. *J. Cell Biol.* **220**, e202101019 (2021). doi: 10.1083/jcb.202101019; pmid: 34427634
61. P. Zhang *et al.*, Chronic optogenetic induction of stress granules is cytotoxic and reveals the evolution of ALS-FTD pathology. *eLife* **8**, e39578 (2019). doi: 10.7554/eLife.39578; pmid: 30893049
62. Z. R. Grese *et al.*, Specific RNA interactions promote TDP-43 multivalent phase separation and maintain liquid properties. *EMBO Rep.* **22**, e53632 (2021). doi: 10.15252/embr.202153632; pmid: 34787357
63. B. Khalil, M. Linsenmeier, C. L. Smith, J. Shorter, W. Rossoll, Nuclear-import receptors as gatekeepers of pathological phase transitions in ALS/FTD. *Mol. Neurodegener.* **19**, 8 (2024). doi: 10.1186/s13024-023-00698-1; pmid: 38254150
64. J. A. Ortega *et al.*, Nucleocytoplasmic Proteomic Analysis Uncovers eRF1 and Nonsense-Mediated Decay as Modifiers of ALS/FTD *C9orf72* Toxicity. *Neuron* **106**, 90–107.e13 (2020). doi: 10.1016/j.neuron.2020.01.020; pmid: 32059759
65. M. J. Ziller *et al.*, Dissecting the Functional Consequences of *De Novo* DNA Methylation Dynamics in Human Motor Neuron Differentiation and Physiology. *Cell Stem Cell* **22**, 559–574.e9 (2018). doi: 10.1016/j.stem.2018.02.012; pmid: 29551301
66. A. Wang *et al.*, A single N-terminal phosphomimic disrupts TDP-43 polymerization, phase separation, and RNA splicing. *EMBO J.* **37**, e97452 (2018). doi: 10.15252/embj.201797452; pmid: 29438978
67. E. Bogaert *et al.*, Molecular Dissection of FUS Points at Synergistic Effect of Low-Complexity Domains in Toxicity. *Cell Rep.* **24**, 529–537.e4 (2018). doi: 10.1016/j.celrep.2018.06.070; pmid: 30021151
68. Y. Hamuro, Quantitative Hydrogen/Deuterium Exchange Mass Spectrometry. *J. Am. Soc. Mass Spectrom.* **32**, 2711–2727 (2021). doi: 10.1021/jasms.1c00216; pmid: 34749499
69. L. Mayne *et al.*, Many overlapping peptides for protein hydrogen exchange experiments by the fragment separation-mass spectrometry method. *J. Am. Soc. Mass Spectrom.* **22**, 1898–1905 (2011). doi: 10.1007/s13361-011-0235-4; pmid: 21952777
70. P. Mohanty *et al.*, A synergy between site-specific and transient interactions drives the phase separation of a disordered, low-complexity domain. *Proc. Natl. Acad. Sci. U.S.A.* **120**, e2305625120 (2023). doi: 10.1073/pnas.2305625120; pmid: 37579155
71. Y. Luo, B. Roux, Simulation of Osmotic Pressure in Concentrated Aqueous Salt Solutions. *J. Phys. Chem. Lett.* **1**, 183–189 (2009). doi: 10.1021/jz900079w
72. R. B. Best, W. Zheng, J. Mittal, Balanced Protein–Water Interactions Improve Properties of Disordered Proteins and Non-Specific Protein Association. *J. Chem. Theory Comput.* **10**, 5113–5124 (2014). doi: 10.1021/ct500569b; pmid: 25400522
73. G. H. Zerze, W. Zheng, R. B. Best, J. Mittal, Evolution of All-Atom Protein Force Fields to Improve Local and Global Properties. *J. Phys. Chem. Lett.* **10**, 2227–2234 (2019). doi: 10.1021/acs.jpclett.9b00850; pmid: 30990694
74. M. Zgarbová *et al.*, Refinement of the Cornell et al. Nucleic Acids Force Field Based on Reference Quantum Chemical Calculations of Glycosidic Torsion Profiles. *J. Chem. Theory Comput.* **7**, 2886–2902 (2011). doi: 10.1021/ct200162x; pmid: 21921995
75. T. Steinbrecher, J. Latzer, D. A. Case, Revised AMBER parameters for bioorganic phosphates. *J. Chem. Theory Comput.* **8**, 4405–4412 (2012). doi: 10.1021/ct300613v; pmid: 23264757
76. B. Ozguney, P. Mohanty, J. Mittal, RNA binding tunes the conformational plasticity and intradomain stability of TDP-43 tandem RNA recognition motifs. *Biophys. J.* **123**, 3844–3855 (2024). doi: 10.1016/j.bpj.2024.09.031; pmid: 39354713
77. M. J. Abraham *et al.*, GROMACS: High performance molecular simulations through multi-level parallelism from laptops to supercomputers. *SoftwareX* **1-2**, 19–25 (2015). doi: 10.1016/j.softx.2015.06.001
78. G. Bussi, D. Donadio, M. Parrinello, Canonical sampling through velocity rescaling. *J. Chem. Phys.* **126**, 014101 (2007). doi: 10.1063/1.2408420; pmid: 17212484
79. M. Parrinello, A. Rahman, Polymorphic transitions in single crystals: A new molecular dynamics method. *J. Appl. Phys.* **52**, 7182–7190 (1981). doi: 10.1063/1.328693
80. D. A. Case *et al.*, AmberTools. *J. Chem. Inf. Model.* **63**, 6183–6191 (2023). doi: 10.1021/acs.jcim.3c01153; pmid: 37805934
81. C. W. Hopkins, S. Le Grand, R. C. Walker, A. E. Roitberg, Long-Time-Step Molecular Dynamics through Hydrogen Mass Repartitioning. *J. Chem. Theory Comput.* **11**, 1864–1874 (2015). doi: 10.1021/ct5010406; pmid: 26574392
82. J. Åqvist, P. Wennerström, M. Nervall, S. Bjelic, B. O. Brandsdal, Molecular dynamics simulations of water and biomolecules with a Monte Carlo constant pressure algorithm. *Chem. Phys. Lett.* **384**, 288–294 (2004). doi: 10.1016/j.cplett.2003.12.039
83. T. Darden, D. York, L. Pedersen, Particle mesh Ewald: An *N*·log(*N*) method for Ewald sums in large systems. *J. Chem. Phys.* **98**, 10089–10092 (1993). doi: 10.1063/1.464397
84. J.-P. Ryckaert, G. Ciccotti, H. J. C. Berendsen, Numerical integration of the cartesian equations of motion of a system with constraints: Molecular dynamics of *n*-alkanes. *J. Comput. Phys.* **23**, 327–341 (1977). doi: 10.1016/0021-9991(77)90098-5
85. F. Delaglio *et al.*, NMRPipe: A multidimensional spectral processing system based on UNIX pipes. *J. Biomol. NMR* **6**, 277–293 (1995). doi: 10.1007/BF00197809; pmid: 8520220
86. S. P. Skinner *et al.*, CcpNmr AnalysisAssign: A flexible platform for integrated NMR analysis. *J. Biomol. NMR* **66**, 111–124 (2016). doi: 10.1007/s10858-016-0060-y; pmid: 27663422
87. J. Ganssauge *et al.*, Rapid and inducible mislocalization of endogenous TDP43 in a novel human model of amyotrophic lateral sclerosis. *eLife* **13**, RP95062 (2025). doi: 10.7554/eLife.95062.3; pmid: 40704991
88. Z. Y. Kan, X. Ye, J. J. Skinner, L. Mayne, S. W. Englander, ExMS2: An Integrated Solution for Hydrogen–Deuterium Exchange Mass Spectrometry Data Analysis. *Anal. Chem.* **91**, 7474–7481 (2019). doi: 10.1021/acs.analchem.9b01682; pmid: 31082210
89. Y. Perez-Riverol *et al.*, The PRIDE database at 20 years: 2025 update. *Nucleic Acids Res.* **53**, D543–D553 (2025). doi: 10.1093/nar/gkae1011; pmid: 39494541
90. J. Shorter, Data from: Short RNA chaperones promote aggregation-resistant TDP-43 conformers to mitigate neurodegeneration, *Dryad* (2026). doi: 10.5061/dryad.9s4mw6mx4

ACKNOWLEDGMENTS

We thank L. Miller, E. Barbieri, and J. Lin for critiques and K. Lynch for access to the Typhoon scanner. We thank N. Bryan for preliminary digestion and HXMS conditions and HX rate determination of TDP-43. We thank E. Smith for assistance with HMXS data visualization and MS data deposition. We thank C. Yang for assistance with the electron microscope. Some figure subpanels were created with BioRender.com. **Funding:** This research was supported by National Institutes of Health (NIH) grants T32GM132039 (K.E.C.), F31NS129101 (K.E.C.), R35GM156396 (Y.-W.C.), R01NS109150 (P.P.), R01NS116176 (J.M. and N.L.F.), R01NS127187 (C.J.D.), R21AG064940 (C.J.D.), R01NS105756 (C.J.D.), UL1TR001878 (J.S.), and RF1AG090910 (C.J.D. and J.S.); the National Science Foundation Graduate Research Fellowship Program (H.L.D.); an ALSA Milton Safenowitz Postdoctoral Fellowship (M.L.); an Alzheimer's Association Research Fellowship (M.L. and H.M.O.); a Mildred Cohn Distinguished Postdoctoral Award (M.L.); an ALS Scholars in Therapeutics Award (Sean M. Healey and AMG Center for ALS, Massachusetts General Hospital, ALS Finding a Cure, FightMND) (M.L.); an American Heart Association Postdoctoral Fellowship (B.P.); a BrightFocus Postdoctoral Fellowship (B.P.); an AstraZeneca Postdoctoral Fellowship (H.M.O.); a Johnson Foundation Fellowship (H.M.O.); the Motor Neurone Disease Association (Ule/Apr22/886-791) (M.H.); the UK Dementia Research Institute (award no. UK DRI-RE21605) through UK DRI Ltd., principally funded by the UK Medical Research Council and by the Francis Crick Institute, which receives its core funding from Cancer Research UK (CC0102), the UK Medical Research Council (CC0102), and the Wellcome Trust (CC0102) (J.U.); a Structural Biology Pilot Award from the University of Pennsylvania Department of Biochemistry and Biophysics (B.E.B. and J.S.); the LiveLikeLou Center for ALS Research at the University of Pittsburgh (C.J.D.); the Farber Family Foundation (P.P. and B.K.J.); Family Strong 4 ALS (P.P. and B.K.J.); the Packard Center for ALS Research at Johns Hopkins (J.S.); Target ALS (C.J.D. and J.S.); the Association for Frontotemporal Degeneration (J.S.); the Amyotrophic Lateral Sclerosis Association (J.S.); the Office of the Assistant Secretary of Defense for Health Affairs through the Amyotrophic Lateral Sclerosis Research Program W81XWH-20-1-0242 (J.S.); the Institute for Translational Medicine and Therapeutics (ITMAT) Transdisciplinary Program in Translational Medicine and Therapeutics (J.S.); the Kissick Family Foundation and the Milken Institute Science Philanthropy Accelerator for Research and Collaboration (C.J.D. and J.S.); and an Alzheimer's Association Zenith Research Fellows Award (J.S.). **Author contributions:** Conceptualization: K.E.C., C.J.D., J.S.; Data curation: K.E.C., J.C.M., H.L.D., Q.C., B.O., M.N., L.X., A.S., M.L., C.A.B., J.M., C.J.D., B.K.J., J.S.; Formal analysis: K.E.C., J.C.M., H.L.D., Q.C., B.O., M.D., A.S., L.M., M.L., C.A.B., J.M., B.K.J., J.S.; Funding acquisition: K.E.C., H.L.D., M.L., B.P., H.M.O., P.P., J.M., N.L.F., B.E.B., C.J.D., B.K.J., J.S.; Investigation: K.E.C., J.C.M., H.L.D., Q.C., B.O., M.N., L.X., A.S., M.D., L.M., M.L., J.D.R., C.A.B., B.P., B.L.L., H.M.O., L.L., B.K.J.; Methodology: K.E.C., J.C.M., H.L.D., Q.C., B.O., M.N., L.X., L.M., M.L., J.D.R., C.A.B., B.P., L.L., M.H., J.U., P.P., Y.P., J.M., N.L.F., B.E.B., C.J.D., B.K.J., J.S.; Project administration: K.E.C., P.P., J.M., N.L.F., B.E.B., C.J.D., B.K.J., J.S.; Resources: K.E.C., J.C.M., H.L.D., L.X., A.S., L.M., M.L., J.D.R., C.A.B., M.H., J.U., P.P., J.M., N.L.F., B.E.B., C.J.D., B.K.J., J.S.; Supervision: K.E.C., L.M., Y.-W.C., P.P., J.M., N.L.F., B.E.B., C.J.D., B.K.J., J.S.; Validation: K.E.C., J.C.M., H.L.D., Q.C., B.O., M.N., L.X., A.S., L.M., M.L., J.D.R., C.A.B., B.P., B.L.L., H.M.O., J.M., B.K.J., J.S.; Visualization: K.E.C., J.C.M., H.L.D., Q.C., B.O., M.N., L.X., A.S., L.M., C.A.B., J.M., N.L.F., B.E.B., C.J.D., B.K.J., J.S.; Writing – original draft: K.E.C., H.L.D., B.K.J., J.S.; Writing – review & editing: K.E.C., J.C.M., H.L.D., Q.C., B.O., M.N., L.X., A.S., M.D., L.M., M.L., J.D.R., C.A.B., B.P., B.L.L., H.M.O., L.L., Y.-W.C., M.H., J.U., P.P., Y.P., J.M., N.L.F., B.E.B., C.J.D., B.K.J., J.S. **Competing interests:** B.P., C.J.D., and J.S. are inventors on US patent 12,521,412 (Nucleic acids and nucleic acid analogs for treating, preventing, and disrupting pathological polynucleotide-binding protein inclusions) held by the University of Pennsylvania and the University of Pittsburgh. K.E.C., C.J.D., and J.S. are inventors on patent application

PCT/US2025/058953 (Compositions and methods for reducing aggregation, neurodegeneration and/or proteinopathies) filed by the University of Pennsylvania and the University of Pittsburgh. The remaining authors have no competing interests. **Data, code, and materials availability:** Plasmids generated in this study will be made readily available to the scientific community. All requests will be honored in a timely manner. Material transfers will be made with no more restrictive terms than in the Simple Letter Agreement or the Uniform Biological Materials Transfer Agreement and without reach through requirements. All data used for this study are available in the manuscript or the supplementary materials or are deposited at the indicated data repositories. The mass spectrometry proteomics data for HXMS experiments have been deposited at the ProteomeXchange Consortium through the PRIDE partner repository (*89*) with the dataset identifier PXD071117. All tabulated data underlying the figures are deposited at Dryad (*90*). This paper does not report original code. This research was funded in whole or in part by UK Dementia Research Institute (award no. UK DRI-RE21605) through UK DRI Ltd., principally funded by the UK Medical Research Council, and by Wellcome Trust (CC0102), cOAlition S organizations. The author will make the Author Accepted Manuscript (AAM) version available under a CC BY public copyright license.

SUPPLEMENTARY MATERIALS

science.org/doi/10.1126/science.adv3301
Supplementary Text; Figs. S1 to S27; Tables S1 to S4; References (*91*–*100*);
MDAR Reproducibility Checklist

Submitted 14 December 2024; resubmitted 21 November 2025; accepted 10 February 2026
10.1126/science.adv3301

Short RNA chaperones promote aggregation-resistant TDP-43 conformers to mitigate neurodegeneration

Katie E. Copley, Jocelyn C. Mauna, Helen L. Danielson, Qizan Chen, Busra Ozguney, Marilyn Ngo, Longxin Xie, Ashleigh Smirnov, Matt Davis, Leland Mayne, Miriam Linsenmeier, Jack D. Rubien, Cristian A. Bergmann, Bede Portz, Bo Lim Lee, Hana M. Odeh, Longsheng Lai, Yi-Wei Chang, Martina Hallegger, Jernej Ule, Piera Pasinelli, Yan Poon, Jeetain Mittal, Nicolas L. Fawzi, Ben E. Black, Christopher J. Donnelly, Brigid K. Jensen, and James Shorter

Science **392** (6798), eadv3301. DOI: 10.1126/science.adv3301

Editor's summary

TDP-43 aggregation plays a prominent pathogenic role in several neurodegenerative diseases including amyotrophic lateral sclerosis and related proteinopathies. Reducing TDP-43 aggregation is critical for limiting neuronal loss. Copley *et al*. developed a therapeutic strategy in which short RNAs work as chaperones that bind to and inhibit TDP-43 aggregation. These RNAs bind to TDP-43's RNA recognition motifs, stabilizing the protein and preventing aggregation by destabilizing regions prone to self-assembly. Treatment with short RNAs restored TDP-43 nuclear localization in patient-derived neurons carrying a pathogenic mutation and alleviated TDP-43 aggregation and prevented neuronal death in a mouse model. These results pave the way for the development of therapeutic strategies for TDP-43–related disorders. —Mattia Maroso

View the article online
https://www.science.org/doi/10.1126/science.adv3301
Permissions
https://www.science.org/help/reprints-and-permissions

Science (ISSN 1095-9203) is published by the American Association for the Advancement of Science. 1200 New York Avenue NW, Washington, DC 20005. The title *Science* is a registered trademark of AAAS.

Supplementary Materials for

Short RNA chaperones promote aggregation-resistant TDP-43 conformers to mitigate neurodegeneration

Katie E. Copley *et al*.

Corresponding author: James Shorter, jshorter@pennmedicine.upenn.edu

Science **392**, eadv3301 (2026)
DOI: 10.1126/science.adv3301

The PDF file includes:

Supplementary Text
Figs. S1 to S27
Tables S1 to S4
References

Other Supplementary Material for this manuscript includes the following:

MDAR Reproducibility Checklist

Supplementary Text:

The PrLD antagonizes Clip34 chaperone activity

To explore whether the inhibitory effect of the PrLD on RNA binding impacts the ability of Clip34 to prevent TDP-43 aggregation, we assessed the ability of Clip34 to antagonize aggregation of TDP-43 variants with specific deletions within the PrLD: TDP-43$^{\Delta IDR1}$, TDP-43$^{\Delta CR}$, TDP-43$^{\Delta CR/IDR2(Q/N)}$, TDP-43$^{\Delta IDR2(G/S)}$, and TDP-43$^{\Delta CR/IDR2}$ (fig. S3A). As anticipated, TDP-43$^{\Delta CR}$ and TDP-43$^{\Delta CR/IDR2}$ exhibited reduced aggregation, whereas TDP-43$^{\Delta IDR1}$, TDP-43$^{\Delta CR/IDR2(Q/N)}$, and TDP-43$^{\Delta IDR2(G/S)}$ aggregated to a similar extent as full-length TDP-43 (fig. S3B) (*29*). Notably, Clip34 exhibited enhanced ability to antagonize aggregation of these partial PrLD deletion variants (fig. S3, C to I). Thus, the entire PrLD antagonizes the ability of Clip34 to reduce TDP-43 aggregation. Collectively, these findings reveal allosteric crosstalk between the TDP-43 RRMs, PrLD, and RNA, which regulates the balance of soluble and aggregation-prone forms of TDP-43.

Clip34 exhibits reduced ability to stabilize the RRMs and disrupt CR helicity in TDP-43^{5FL}

To further evaluate how Clip34 chaperones TDP-43, we performed HXMS analyses of TDP-43^{5FL} in the absence or presence of Clip34. Clip34 binds weakly to TDP-43^{5FL} (Fig. 1J and fig. S2B) and fails to inhibit TDP-43^{5FL} aggregation (Fig. 1K), indicating a reduced capacity to induce an aggregation-resistant conformation. Consistent with this observation, HXMS revealed markedly diminished or absent stabilization of the TDP-43^{5FL} RRMs in the presence of Clip34 (Table S3 and fig. S8, A and B, and fig. S9, A to E). Moreover, the CR of TDP-43^{5FL} retained bimodal exchange spectra, including a prominent slow-exchanging population, in the presence of Clip34 (fig. S9A and fig. S10, A to D). These findings demonstrate that Clip34 exhibits reduced ability to stabilize the RRMs and disrupt the bimodal behavior of the CR in TDP-43^{5FL}, thereby limiting chaperone activity. We conclude that stabilization of the RRMs and destabilization of the CR within the PrLD are both induced by Clip34 binding to the RRMs.

Interpretation of HXMS data for bimodal peptides reveals reduced allosteric coupling in TDP-43^{5FL}

For HXMS experiments, interpretation of stabilization changes based on differences in exchange percentage is complicated when peptides exhibit bimodal behavior. This complexity arises because differences in exchange percentage are derived from peptide deuteration values calculated using envelope centroid values (*91*). The centroid values reported by HDExaminer are less informative for bimodal peptides, since a single centroid does not readily capture the relative populations of peptides in stabilized versus destabilized states (*92*). Mass spectra therefore provide a more reliable measure for these bimodal peptides, as they reveal clear shifts in the proportion of stabilized and destabilized populations (*93*).

For example, although Clip34 appears to destabilize the CR of TDP-43^{5FL} when visualized by exchange percentage (fig. S9A), inspection of the mass spectra shows that the effect is minimal and of greatly reduced magnitude compared with the impact of Clip34 on the CR of wild-type TDP-43 (fig. S10, A to D). Thus, Clip34 strongly destabilizes the CR only in the wild-type protein, whereas spectra for TDP-43^{5FL} retain pronounced bimodality similar to the free state (fig. S10, A to D). The modest destabilizing effect of Clip34 on the CR of TDP-43^{5FL} parallels the correspondingly weak stabilizing effect on the RRMs, reflecting the reduced affinity of

Clip34 for the RRMs in this variant (Fig. 1J and fig. S9, A to E). In addition, exchange percentage data for CR peptides indicate that the CR in TDP-43^{5FL} is slightly more stable in the free state than in wild-type TDP-43 (fig. S4A and fig. S8A). This mildly increased intrinsic stability further limits the capacity of Clip34 to destabilize the CR upon binding to the RRMs. Together, these findings indicate that mutation of the five conserved Phe residues in TDP-43^{5FL} increases the intrinsic stability of the CR while weakening short RNA binding to the RRMs. These effects combine to attenuate the chaperone activity of Clip34 against TDP-43^{5FL}. Furthermore, these data suggest that the five Phe residues mutated in TDP-43^{5FL} likely contribute to priming CR unfolding in the free state, and disruption of these residues weakens the allosteric coupling between the RRMs and CR.

Molecular dynamics simulations reveal allosteric remodeling of the PrLD upon RNA engagement with the tandem RRMs

Mechanistically explaining how a short RNA chaperone binding to folded domains, such as the tandem RRMs, favors a distinct ensemble of conformations of a distant disordered region like the PrLD presents a significant experimental challenge. Such effects may arise from a combination of forces that are propagated through the protein upon RNA engagement. These processes are often described as allosteric, although this term has been applied broadly and does not always capture the full range of mechanisms involved, even within well-structured proteins and especially within intrinsically disordered proteins (IDPs) (*94*). Previous studies have proposed that IDPs can undergo allosteric regulation through enthalpic mechanisms such as binding-site competition (*95, 96*) or entropic mechanisms such as entropic redistribution (*97*). These mechanisms range from direct local contacts to global conformational rewiring, both of which are particularly relevant for TDP-43. We therefore asked whether a short RNA chaperone binding to the RRMs influences the distant PrLD through direct RNA–PrLD contacts that immediately alter PrLD conformation, or through indirect mechanisms in which RNA engagement remodels the TDP-43 interaction landscape and thereby shifts the PrLD conformational ensemble.

To evaluate these mechanisms and complement experimental findings, we performed multi-microsecond all-atom molecular dynamics simulations of both TDP-43$^{\Delta NTD}$ and full-length TDP-43 in the absence and presence of the AUG12 short RNA chaperone (Table S1 and Table S4 and fig. S11 and S12). The AUG12 RNA (GUGUGAAUGAAU) is a synthetic GU-rich 12-mer originally used to solve the NMR structure of the TDP-43 RRMs bound to RNA (*17*), and serves here as a defined model ligand. AUG12 inhibits TDP-43 aggregation in a concentration-dependent manner (fig. S11A). Consistent with experimental observations (Fig. 2F), the α-helical CR was disrupted in the presence of RNA in both TDP-43$^{\Delta NTD}$ and full-length TDP-43 (fig. S11B and fig. S12A). The simulations further revealed that the NTD destabilizes RNA binding (fig. S12C), consistent with experimental findings showing that Clip34 binds to full-length TDP-43 with reduced affinity compared to TDP-43$^{\Delta NTD}$ (Fig. 1L). Given that RNA chaperone activity is independent of the NTD (Fig. 1F), we focused subsequent analyses on TDP-43$^{\Delta NTD}$.

We next examined the molecular determinants of RNA binding in the presence of the PrLD (fig. S11C). Both RRMs display UG-rich sequence specificity through hydrophobic interactions between conserved Phe residues (F147, F149, F194, F229, and F231) and U/G bases. In addition, positively charged Arg residues within IDR1 form electrostatic interactions with the negatively charged RNA backbone, which may compete with RRM–RNA contacts and contribute to the negative regulatory influence of the PrLD (Fig. 1, L and N). Notably, neither the CR nor IDR2 exhibited substantial interactions with RNA, indicating that changes in CR helicity upon RNA binding likely arise from indirect, allosteric effects rather than direct RNA engagement (fig. S11C). Consistent with this interpretation, the TDP-43^{5FL} construct, which disrupts conserved Phe–RNA interactions and promotes RNA dissociation, displayed no alteration in CR helicity (fig. S13, A and B).

Having ruled out direct RNA–CR contacts, we next examined how short RNA chaperone binding indirectly remodels the PrLD by altering its conformational ensemble and underlying interaction network. To quantify these effects, we calculated the radius of gyration (R_g) and intrachain distance (R_{ij}) to assess global compaction and long-range contacts, respectively. Short RNA chaperone binding shifted the PrLD toward a more expanded and flexible state, disrupting long-range interactions and producing behavior characteristic of an ideal chain (fig. S11D and fig. S12B). Simultaneously, RNA binding restricted the tandem RRMs to a compact conformation that prevents RRM1 unfolding (fig. S12B and fig. S14, A to C) (*16, 76*). Analysis of intramolecular contacts showed that RNA engagement disrupts IDR1–IDR2 interactions as IDR1 engages the RNA backbone (fig. S11, E and F). At the same time, RRM1–RRM2 contacts remain intact, a defining feature of the RNA-bound state (fig. S11, E and F) (*76, 98*). Notably, neither RRM directly interacts with the CR under either condition (fig. S11F).

Collectively, these computational results reinforce the experimental observations and support an indirect mechanism in which short RNA chaperone binding to the tandem RRMs remodels the PrLD conformational ensemble and interaction network without requiring direct contact with the CR. The data demonstrate that the short RNA exerts chaperone activity specifically when the tandem RRMs engage UG-rich sequences through conserved Phe residues. RNA binding reorganizes intramolecular interactions, shifting the PrLD toward a more disordered ensemble associated with loss of CR helicity, while constraining RRM conformational heterogeneity to suppress aggregation-prone states (fig. S11G) (*16, 76*).

Cooperativity-efficacy trade-off in RNA-mediated inhibition of TDP-43 aggregation

A feature that emerged across the tested short RNA chaperones and TDP-43 variants was a positive correlation between the IC_{50} value and the steepness of the hill slope for inhibition (fig. S17C). In general, RNAs inhibited TDP-43 aggregation in a cooperative manner with h ranging from -1.2 to -20 (fig. S17C). However, increased cooperativity correlated with decreased efficacy of the RNA at preventing TDP-43 aggregation.

Additional RNAs derived from MALAT1 and CLN6 also prevent TDP-43 aggregation

In addition to Malat1_start and CLN6_middle, we tested two additional RNAs derived from both the *MALAT1* and *CLN6* RNAs: Malat1_middle, Malat1_end, CLN6_start, and CLN6_end (fig. S17A). These RNAs were effective at preventing WT TDP-43 aggregation, although less potently than Malat1_start or CLN6_middle, respectively, based on IC_{50} values (fig. S17, D to G). Each of these four RNAs also prevented aggregation of the TDP-43 RRM1 missense variant TDP-43^{P112H} and the RRM1-RRM2 linker variant TDP-43^{K181E} (fig. S17, D to G). Out of all tested natural RNAs, CLN6_end had the lowest potency against WT TDP-43 (IC_{50}~0.67 μM;

Fig. 3B and fig. S16, C to E, and fig. S17, D to G). This trend was also captured by sedimentation analysis of the end timepoint of aggregation assays, where CLN6_end was less effective at maintaining WT TDP-43 in the soluble fraction (fig. S17, H and I).

Short G-quadruplex RNAs are potent TDP-43 chaperones

To identify additional natural RNAs that effectively chaperone TDP-43, we also considered findings that G-quadruplex DNAs and RNAs can serve as protein chaperones (*99*). Indeed, a 28nt G-quadruplex-forming DNA sequence, *LTR-III*, can effectively chaperone denatured TagRFP675 protein (*99*). As TDP-43 binds to HIV-1 LTR DNA (*100*), and the *LTR-III* RNA derived from this HIV-1 LTR sequence contains UG dinucleotides, we tested the ability of this RNA to prevent TDP-43 aggregation (fig. S17, A and J). We found that this short G-quadruplex-forming RNA effectively prevents aggregation of WT TDP-43 (fig. S17, J and K). Thus, short G-quadruplex RNAs can potently chaperone TDP-43.

Malat1_start reverses TDP-43 condensation and aberrant aggregation

Having identified Malat1_start as the most potent naturally derived inhibitor of TDP-43 aggregation, we next asked whether this RNA could also reverse TDP-43 condensation and aggregation. TDP-43 aggregates are already present in neurons of patients with ALS/FTD, so the ability to dissolve existing cytoplasmic condensates and aggregates would substantially enhance the therapeutic potential of this RNA chaperone. Under physiological concentrations and buffer conditions, purified TDP-43 spontaneously phase separates into condensates (*13, 29*). Preformed TDP-43 condensates remained intact after addition of buffer or the negative control RNA $(AC)_{17}$ (fig. S19, A to C). However, brightfield microscopy revealed that TDP-43 condensates were initially spherical, but over time morphed into more irregular structures in the presence of buffer or $(AC)_{17}$, indicating an aberrant phase transition (fig. S19C). In striking contrast, TDP-43 condensates were rapidly solubilized by Malat1_start (fig. S19, A to C). Thus, Malat1_start potently reverses TDP-43 condensation.

Purified TDP-43 can also rapidly aggregate into tangled fibrillar aggregates (*12-14, 20*). These preformed TDP-43 aggregates were stable and unaffected by addition of water or the negative control RNA $(AC)_{17}$ (fig. S20, A and B). In striking contrast, Malat1_start partially restored TDP-43 to the soluble fraction (fig. S20, A and B). Electron microscopy revealed that large TDP-43 aggregates persisted in the presence of water or the negative control RNA $(AC)_{17}$ (fig. S20, C to F). Strikingly, Malat1_start remodeled large aggregates into smaller structures (fig. S20, C to F). Indeed, TDP-43 aggregate size was reduced ~100-fold by Malat1_start compared to the no RNA control (fig. S20D). Likewise, Malat1_start greatly reduced TDP-43 aggregate area and density (fig. S20, E and F). Thus, Malat1_start directly solubilizes TDP-43 aggregates.

Clip34 and Malat1_start RNAs do not cause TDP-43 loss of function

A possible concern with employing short RNAs in this way is that they might remain too stably bound to TDP-43 and interfere with essential RNA-processing reactions. However, when RBPs are engaged by nuclear-import receptors in the cytoplasm for transport to the nucleus, bound RNA is ejected, such that the short RNA would be recycled for further rounds of chaperone activity (*63*). Clip34 is not toxic to human cells and does not affect nuclear localization of endogenous TDP-43 (*13*). Moreover, Clip34 does not inhibit TDP-43 function in pre-mRNA splicing reactions (*13*).

To assess whether Malat1_start, Clip34, and $(UG)_{17}$ might interfere with TDP-43 function, we employed the CUTS (CFTR UNC13A TDP-43 Loss-of-Function) biosensor, a cryptic exon RNA biosensor enabling real-time detection of TDP-43 loss of splicing function (*47*). CUTS can detect even an ~10% decrease in TDP-43 functionality (*47*). Clip34 and Malat1_start did not interfere with TDP-43 function (fig. S21G). By contrast, $(UG)_{17}$ interfered with TDP-43 function, and this effect was larger than a siRNA positive control that reduces TDP-43 expression by ~2% (fig. S21G) (*47*). Thus, $(UG)_{17}$ displays undesirable properties and hence did not advance to studies with human induced pluripotent stem cell (iPSC)-derived motor neurons or mice.

Malat1_start restores TDP-43 functionality in stressed iPSC-derived motor neurons

We examined how short RNA chaperones affect the functional activity of TDP-43 as a splicing regulator. Oxidative stress can induce TDP-43 mislocalization, dysfunction, and cryptic exon retention (*15, 50, 51*). Thus, we treated control iPSC-derived motor neurons with sodium arsenite, which induces TDP-43 nuclear depletion, TDP-43 loss of function, and G3BP1-positive stress granules (fig. S23A) (*15, 50, 51*). Loss of TDP-43 function induces cryptic splicing of numerous genes (*9, 52-54*). In particular, TDP-43 dysfunction promotes inclusion of a cryptic exon in *STMN2*, leading to premature polyadenylation and loss of STMN2 protein, which is essential for axonal regeneration (*9, 53*). TDP-43 loss-of-function also causes exon skipping in *KCNQ2*, which encodes a voltage-gated potassium channel critical for neuronal excitability (*52*). Sodium arsenite treatment of iPSC-derived motor neurons induced cryptic splicing of both *STMN2* and *KCNQ2* (fig. S23, B to E). Compared with the control RNA, Malat1_start markedly reduced the abundance of both cryptic products in sodium arsenite–treated motor neurons (fig. S23, B to E). These findings demonstrate that Malat1_start restores TDP-43 splicing function in iPSC-derived motor neurons undergoing stress-induced TDP-43 loss of function.

Malat1_start does not disrupt physiological neuritic RNA granules

Although TDP-43 is predominantly nuclear, it also serves as a key component of axonal RNA granules. To confirm that short RNA chaperones do not perturb these physiological granules, we analyzed TDP-43–containing RNA granules in neurites of healthy isogenic and C9-ALS iPSC-derived motor neurons (fig. S24 and fig. S25). The abundance of TDP-43 puncta in neurites was similar following treatment with Malat1_start or the CTR RNA (fig. S24 and fig. S25A). Furthermore, the abundances of neuritic TDP-43 puncta in the CTR and Malat1_start conditions for the isogenic line were no different from healthy control iPSC-derived motor neurons without RNA treatment. To further assess effects on physiological RNA granules, we examined Staufen-1 (STAU1), another RBP with established roles in neuritic RNA transport and localization (*56*). Both Malat1_start and the CTR RNA showed minimal colocalization with STAU1 in neurites (fig. S24 and fig. S25, B and C). Moreover, the abundance of STAU1-containing puncta remained comparable across treatments with Malat1_start and the CTR RNA (fig. S24 and fig. S25D). Together, these findings indicate that Malat1_start mitigates aberrant TDP-43 phenotypes without disturbing the physiological localization of TDP-43 or STAU1 to neuritic RNA granules.

Figure S1

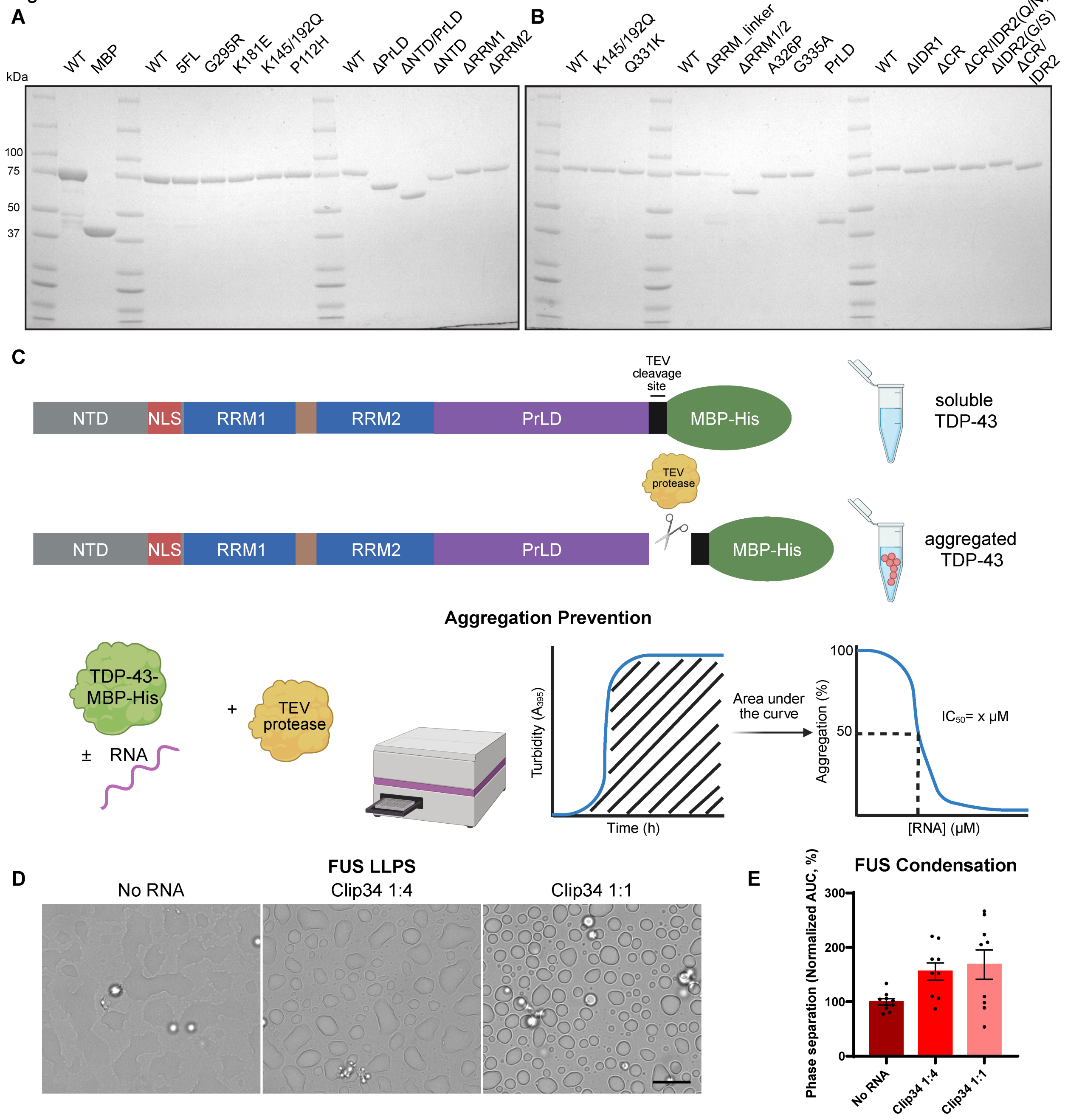

Fig. S1. TDP-43 purification, aggregation assay, and inefficacy of Clip34 against FUS phase separation. (A, B) 4-15% Tris-HCl SDS-PAGE gels loaded with 1 µg of each indicated purified TDP-43-MBP-His variant (or MBP-His alone) and subsequently stained with Coomassie Brilliant Blue. **(C)** Schematic of *in vitro* TDP-43 aggregation prevention assay. TDP-43-MBP-His (5 µM) was incubated with TEV protease (to cleave off the solubilizing MBP-His tag) in the presence or absence of RNA for 16 h, measuring turbidity (absorbance at 395nm) every minute in a plate reader. The standardized turbidity data are normalized so that the No RNA condition maximum value is set to 100; subsequently, the normalized area under the curve (AUC) of these data is taken, which is then utilized to calculate an IC_{50} value (nonlinear regression: [inhibitor] vs. normalized response with variable slope). **(D)** Representative 100x brightfield microscopy images of FUS condensates in the presence or absence of Clip34 RNA, after ~2-2.5 h of measurement in the plate reader. The scale bar represents 10 µm (n=9; 3 biological replicates, each consisting of 3 technical triplicates; [RNA]:[FUS]; 2 µM FUS). **(E)** AUC of turbidity data for the same FUS samples imaged in (D), normalized to the average No RNA value for the respective technical triplicate. Data are mean ± SEM (n=9; 3 biological replicates, each consisting of 3 technical triplicates; [RNA]:[FUS]; 2 µM FUS).

Figure S2

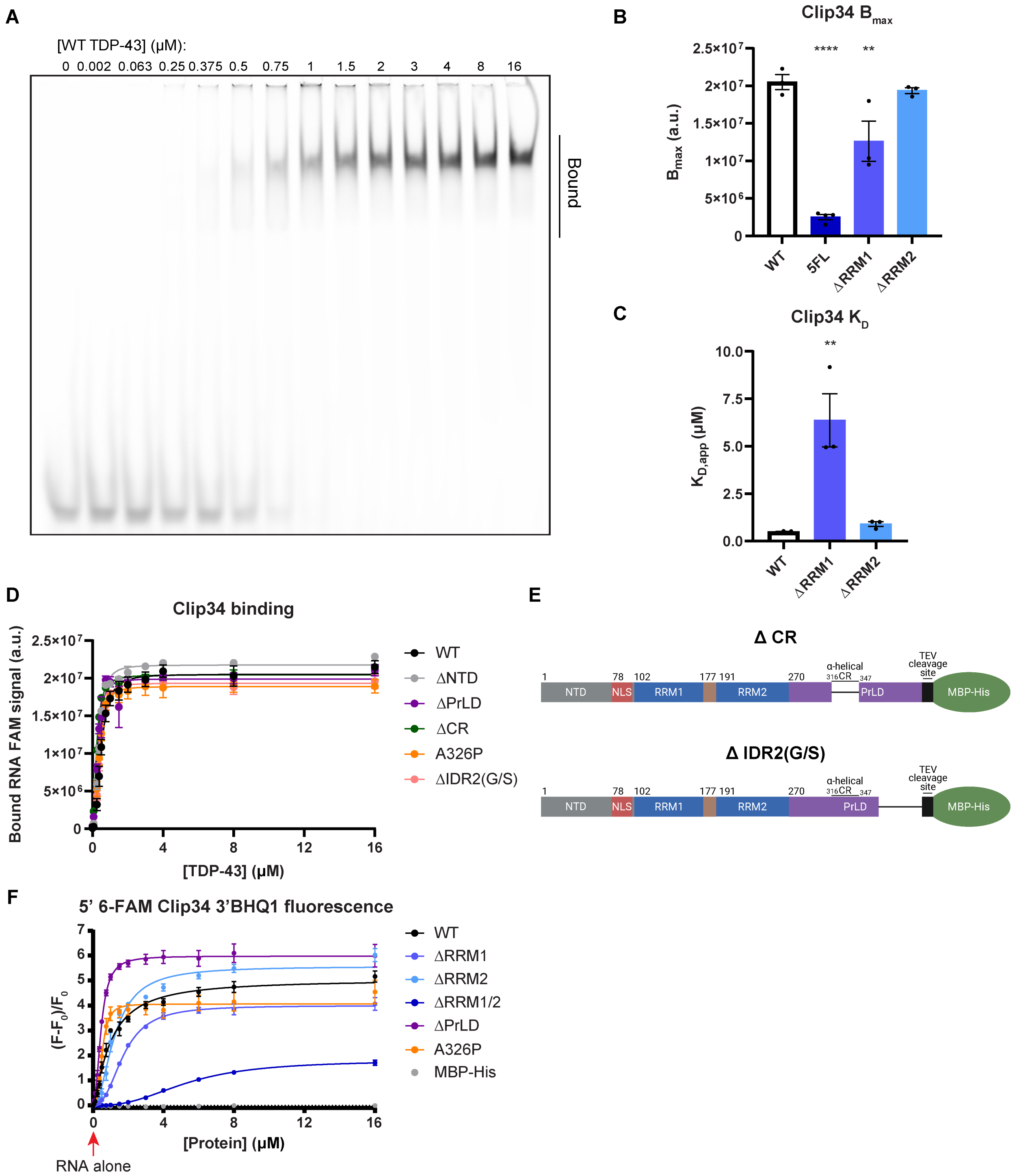

Fig. S2. RNA binding and remodeling activity of TDP-43 variants. (A) Representative image of an EMSA for 100 nM 5' 6-FAM Clip34 with indicated WT TDP-43-MBP-His concentrations, run on a 6% DNA Retardation gel. The vertical bar indicates the approximate area quantified for the bound fraction. **(B, C)** B$_{max}$ (B) and apparent K$_D$ (C) values calculated from the bound signal from individual replicates of EMSAs performed with 5' 6-FAM Clip34 and WT TDP-43-MBP-His or the indicated TDP-43 variant, corresponding to summary data in Fig. 1J. WT data shown is the same data as in Fig. 1L. Data are mean ± SEM (n=3-4; one-way ANOVA with Dunnett's correction comparing to WT; $^{**}p < 0.01$; $^{****}p < 0.0001$). **(D)** Bound 5' 6-FAM Clip34 signal for EMSAs performed with indicated TDP-43-MBP-His variants. WT data shown is the same in Fig. 1J. This is the summary data corresponding to K_D values calculated from individual replicates, shown in Fig. 1L. Data are mean ± SEM (n=2-3; shown is the nonlinear regression: [agonist] vs. response with variable slope, of the combined replicates). **(E)** Domain maps of TDP-43 partial PrLD deletion constructs. Amino acids deleted, inclusive, are: ΔCR, aa316-346; ΔIDR2(G/S), aa367-414. **(F)** Relative fluorescence intensity values for 5' 6-FAM Clip34 3' BHQ1 with indicated TDP-43-MBP-His variants or MBP-His. The red arrow indicates the RNA alone condition, which exhibits low fluorescence and is set at zero for relative fluorescence intensity. Data are mean ± SEM (n=3 for TDP-43 variants; n=2 for MBP-His; 100 nM RNA; shown is the nonlinear regression: [agonist] vs. response with variable slope, of the combined replicates). Half maximal effective concentration (EC_{50}) values were calculated from individual replicates and are shown in Fig. 1N.

Figure S3

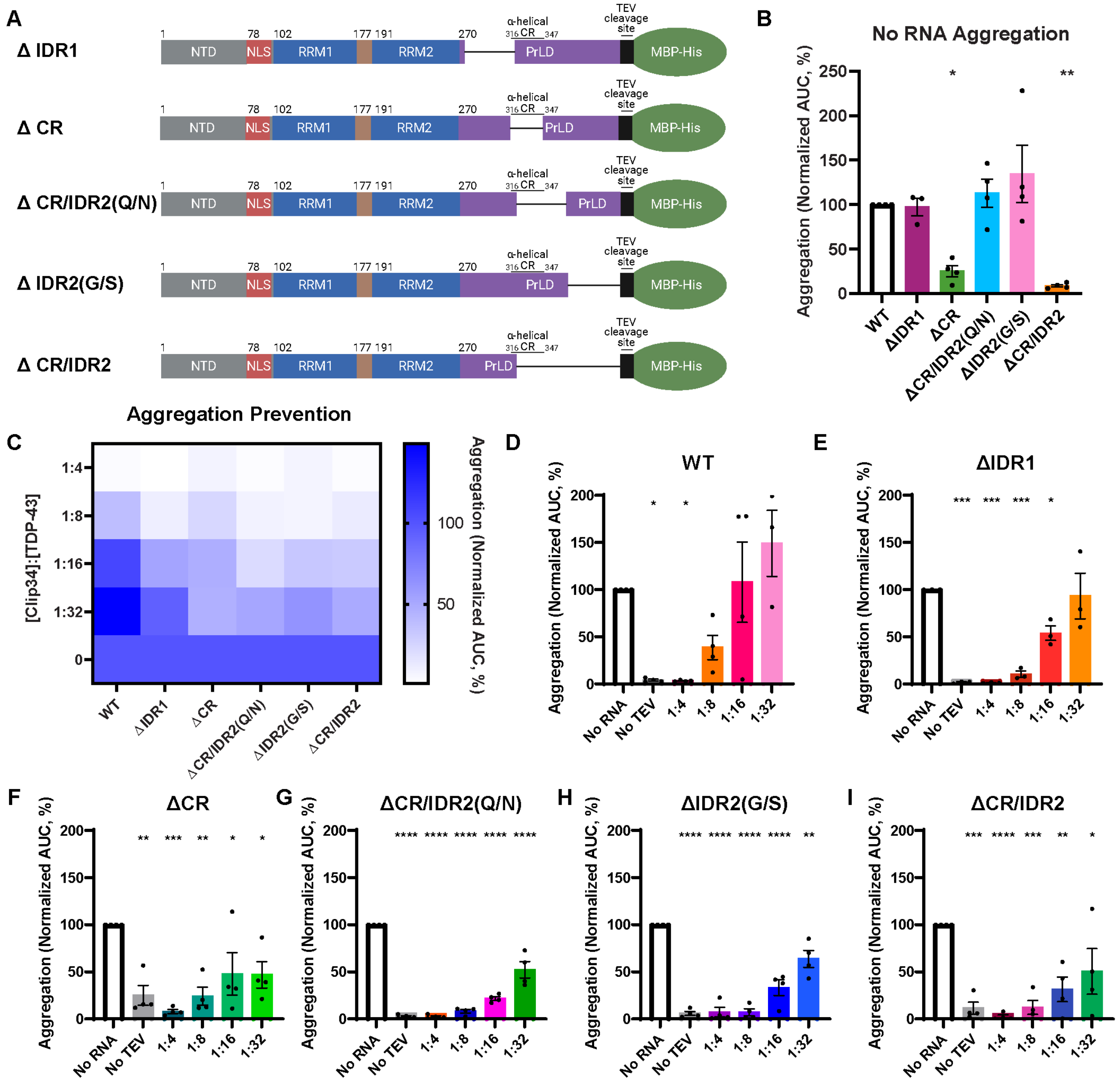

Fig. S3. Clip34 exhibits enhanced chaperone activity against partial PrLD-deletion variants. (A) Domain maps of the TDP-43 partial PrLD deletion constructs. Amino acids deleted, inclusive, are: ΔIDR1, aa274-320; ΔCR, aa316-346; ΔCR/IDR2(Q/N), aa321-366; ΔIDR2(G/S), aa367-414; and ΔCR/IDR2, aa321-414. **(B)** Area under the curve (AUC) of standardized aggregation turbidity data for the No RNA condition for each partial PrLD deletion construct, normalized to WT TDP-43 No RNA, tested by *in vitro* aggregation prevention assays. Data are mean ± SEM (n=3-4; one-way ANOVA with Dunnett's correction comparing to WT; $*p < 0.05$, $**p < 0.01$). **(C)** Heatmap displaying the mean AUC values from *in vitro* aggregation prevention assays for each TDP-43 variant at the indicated molar concentration ratios, normalized to the respective variant's No RNA condition. **(D-I)** Individual replicates of the summary data shown in (C) for each TDP-43 variant. Data are mean ± SEM (n=3-4; one-way ANOVA with Dunnett's correction comparing to No RNA; $*p < 0.05$, $**p < 0.01$, $***p < 0.001$, $****p < 0.0001$).

Figure S4

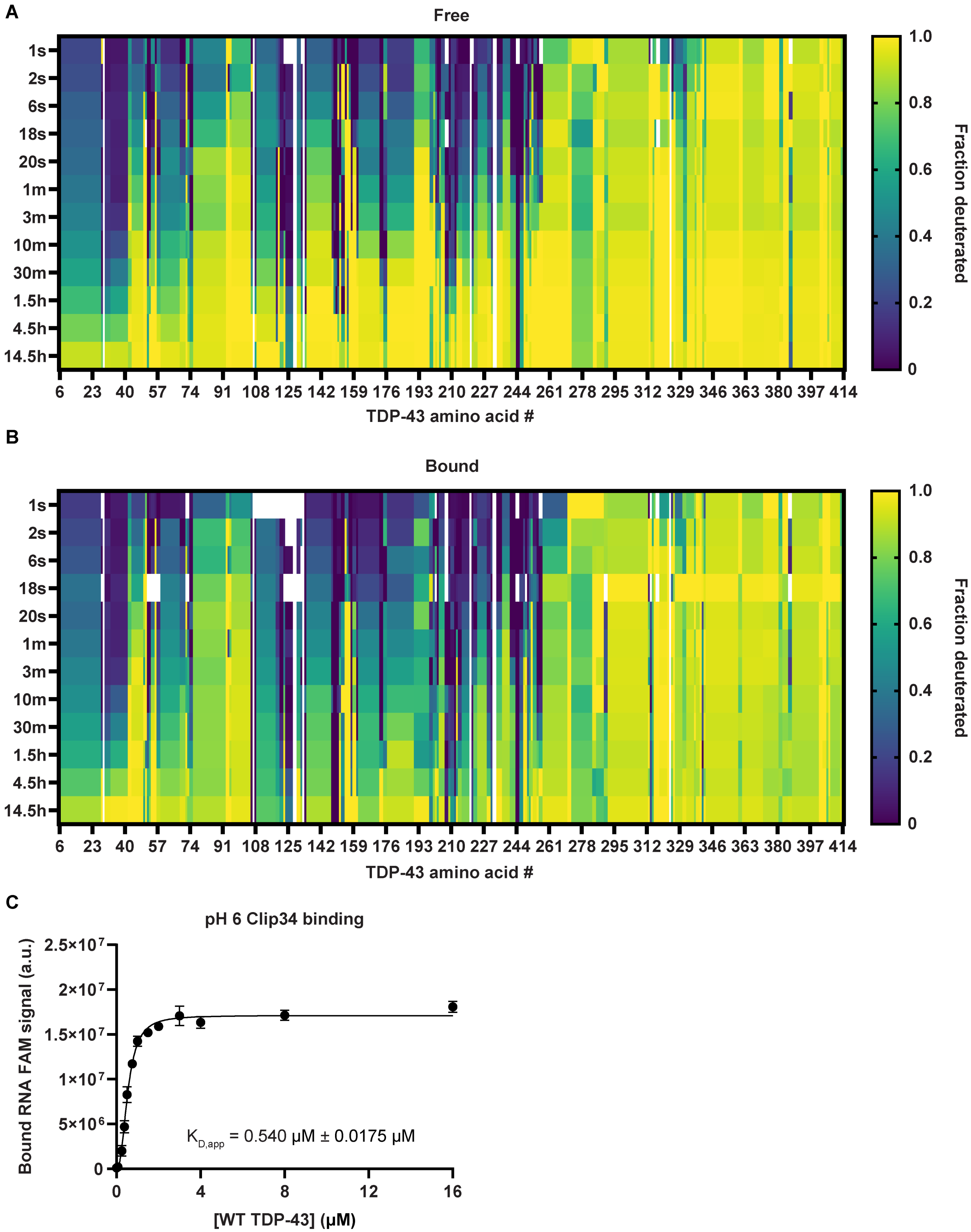

Fig. S4. Hydrogen/deuterium-exchange for TDP-43 in the absence or presence of Clip34 RNA. (A, B) Heatmaps displaying hydrogen/deuterium-exchange for each TDP-43 amino acid in the free (A) and bound (B) states at each timepoint, normalized so that 1 represents fully deuterated and 0 represents not deuterated. White spaces represent small gaps in coverage. Sub-localization between peptides to determine the exchange value at each amino acid was performed by HDExaminer. All 1 s, 2 s, 6 s, and 18 s timepoints were collected utilizing pH 6.0 buffer; 20 s, 1 min, and 3 min timepoints were collected with some replicates utilizing pH 6.0 buffer and others utilizing pH 7.0 buffer; 10 min and longer timepoints were collected utilizing pH 7.0 buffer. **(C)** Bound 5’ 6-FAM Clip34 signal for EMSAs performed with WT TDP-43 in pH 6.0 buffer. Data are mean ± SEM (n=3; shown curve is the nonlinear regression: [agonist] vs. response with variable slope, of the combined replicates; apparent K_D value was calculated from individual replicates).

Figure S5

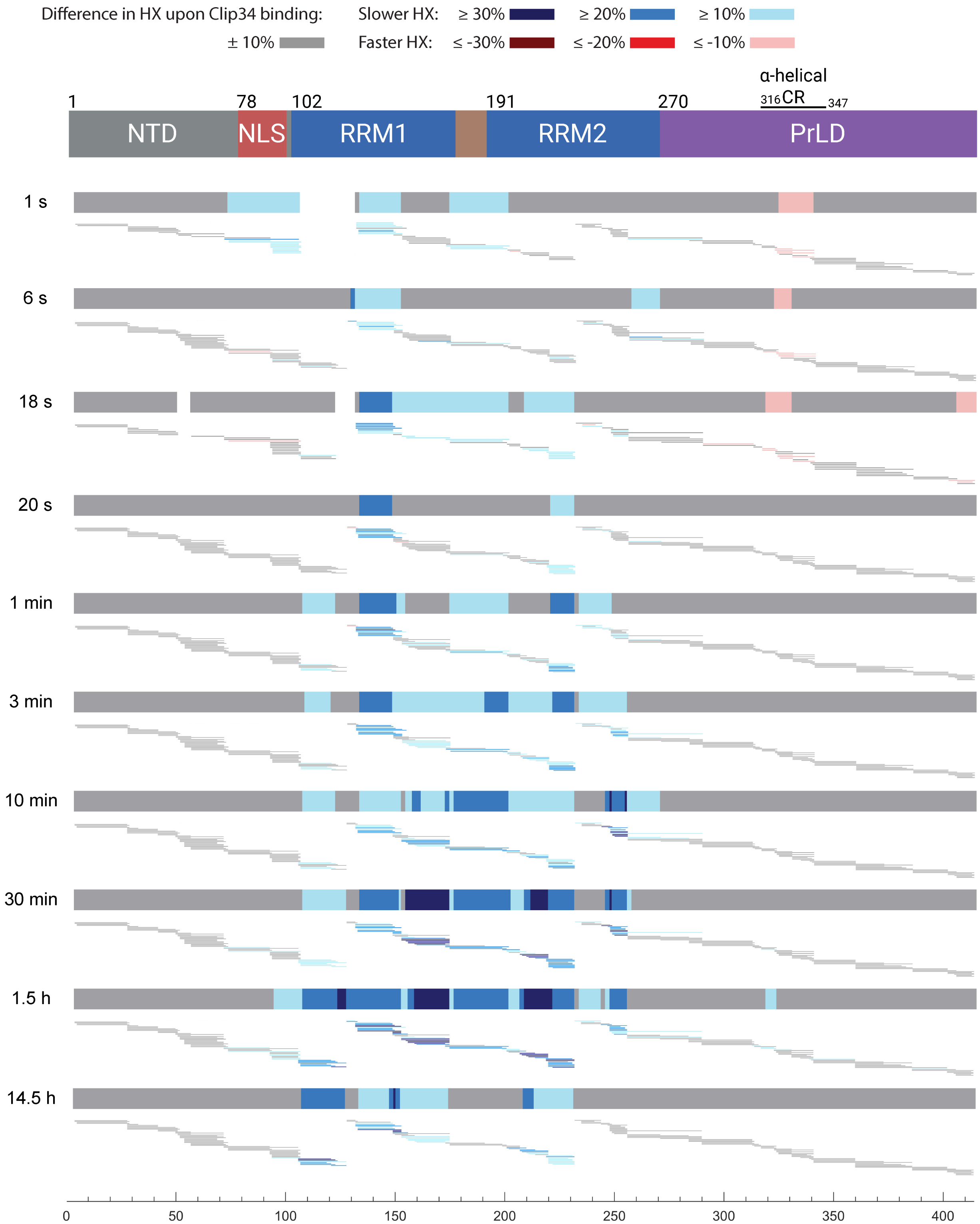

Fig. S5. Hydrogen/deuterium-exchange reveals stabilization of the TDP-43 RRMs and destabilization of the α-helical conserved region in the PrLD upon Clip34 RNA binding. *Top:* domain map of TDP-43, aligned with data underneath. *Bottom:* The consensus percentage difference in exchange between the Clip34-bound and free states at each indicated timepoint is shown again as in Fig. 2A. Aligned beneath each consensus percentage difference in exchange plot are the peptides analyzed at the respective timepoint, with percentage differences in exchange between the Clip34-bound and free states for each peptide colored as shown in the legend. The amino acid number is indicated on the axis below.

Figure S6

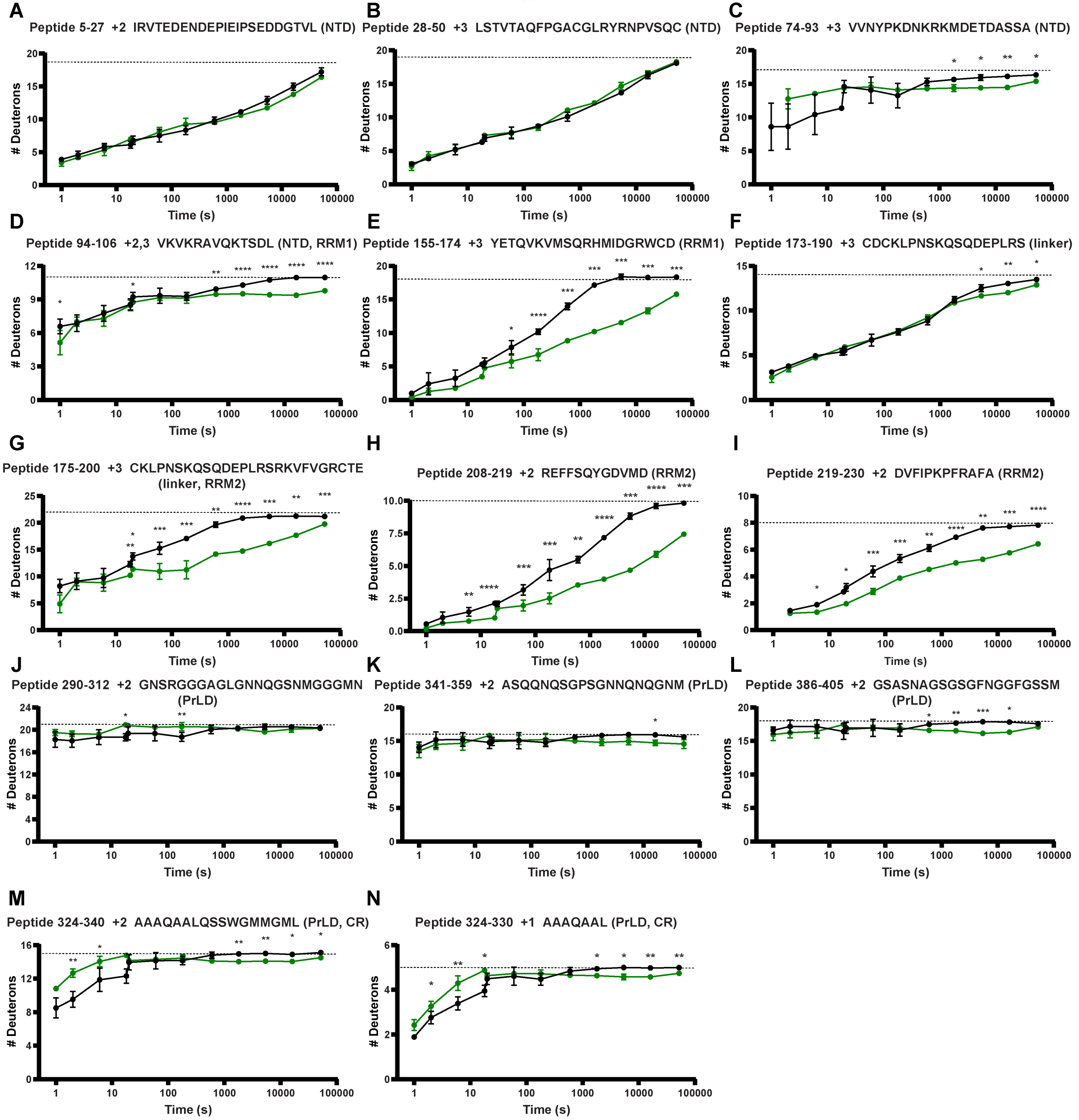

Fig. S6. Hydrogen/deuterium-exchange deuteration curves illustrate the effects of Clip34 RNA binding on TDP-43 structure. (A-N) HX for representative peptides, with charge state and peptide sequence indicated in the graph titles. Representative examples are shown of peptides in the NTD (A-C); bridging the NTD and RRM1 (D); in RRM1 (E); bridging RRM1 and the linker between RRMs (F); bridging RRM1, the linker between RRMs, and RRM2 (G); in RRM2 (H, I); in the PrLD primarily outside of the CR (J-L); and primarily within the α-helical conserved region (CR) of the PrLD (M, N). Other regional features of interest include peptides with residues in the nuclear localization sequence (NLS) (C, D) and peptides located in different parts of the PrLD: within IDR1 (J), at the end of the CR and extending into IDR2 (K), and within the glycine- and serine-rich region of IDR2 (L). The dashed line represents the fully-deuterated condition. Data are mean ± SD (3-7 replicates run on mass spectrometry per timepoint; n=1-14 replicates per peptide per timepoint based on medium or high confidence peptide detection across one or two charge states as indicated in graph titles; error is too small to visualize for a subset of timepoints; Welch's t-test comparing bound and free at each timepoint; *$p < 0.05$, **$p < 0.01$, ***$p < 0.001$, ****$p < 0.0001$).

Figure S7

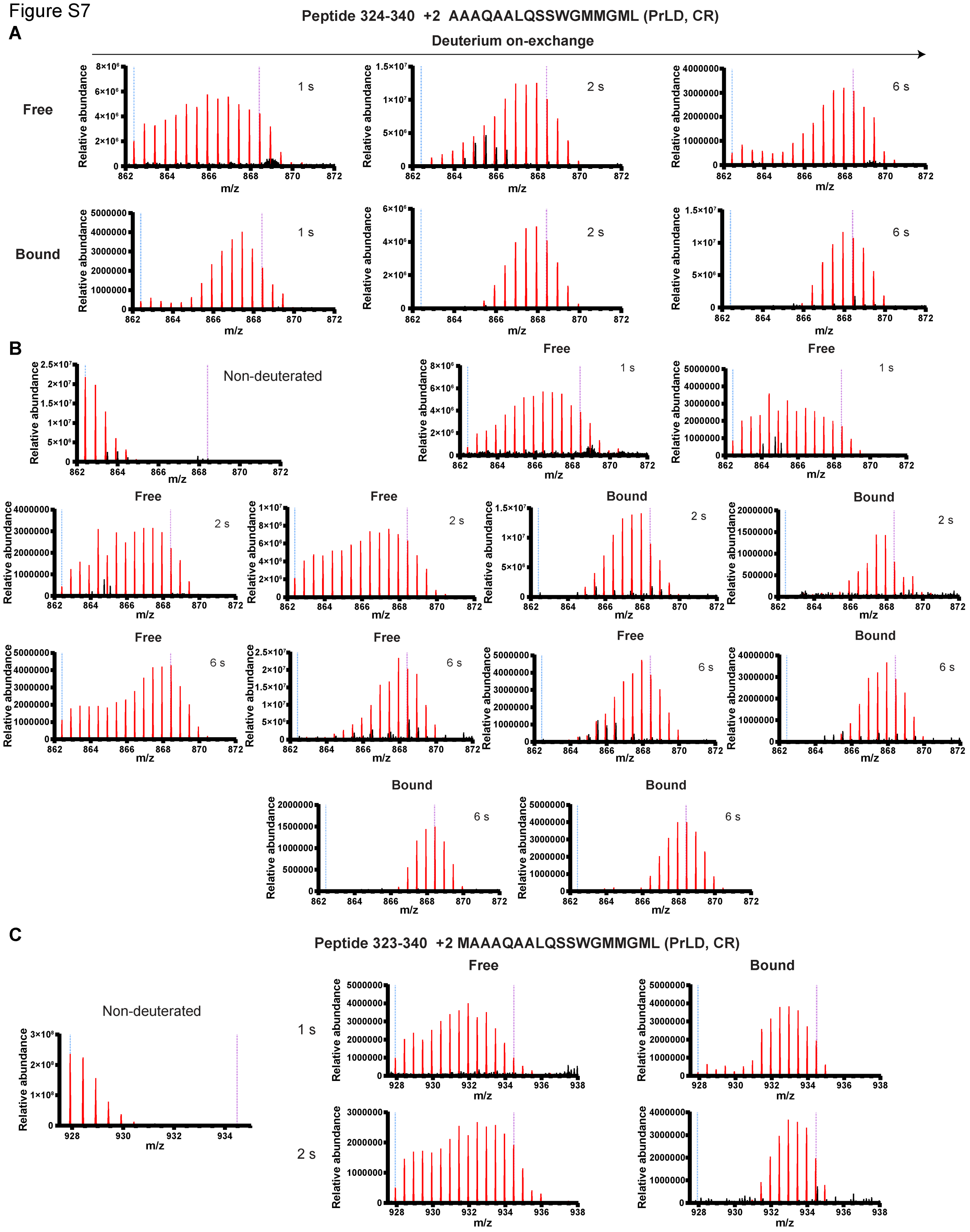

Fig. S7. Mass spectra illustrate the effects of Clip34 RNA binding on TDP-43 structure. (A-C) Raw mass spectra data, with signal corresponding to the appropriate peptide as determined by appropriate m/z values colored red, and noise from overlapping peptide(s) colored black. The two dashed lines serve as visual guides; the blue dashed line indicates the monoisotopic peak, whereas the purple dashed line indicates the centroid value of the peptide in the fully deuterated sample. Spectra at 1 s, 2 s, and 6 s timepoints for the free and bound states for the indicated peptide in the CR of the PrLD, in addition to the representative spectra shown in Fig. 2G (A). The raw mass spectrum data of a representative non-deuterated sample, and remaining raw mass spectra data for replicates at 1 s, 2 s, and 6 s timepoints for the free and bound states of the indicated peptide, in addition to those shown in Fig. 2G and fig. S7A (B). The raw mass spectrum data of a representative non-deuterated sample, and representative spectra at 1 s and 2 s timepoints for the free and bound states for the indicated peptide in the CR of the PrLD (C).

Figure S8

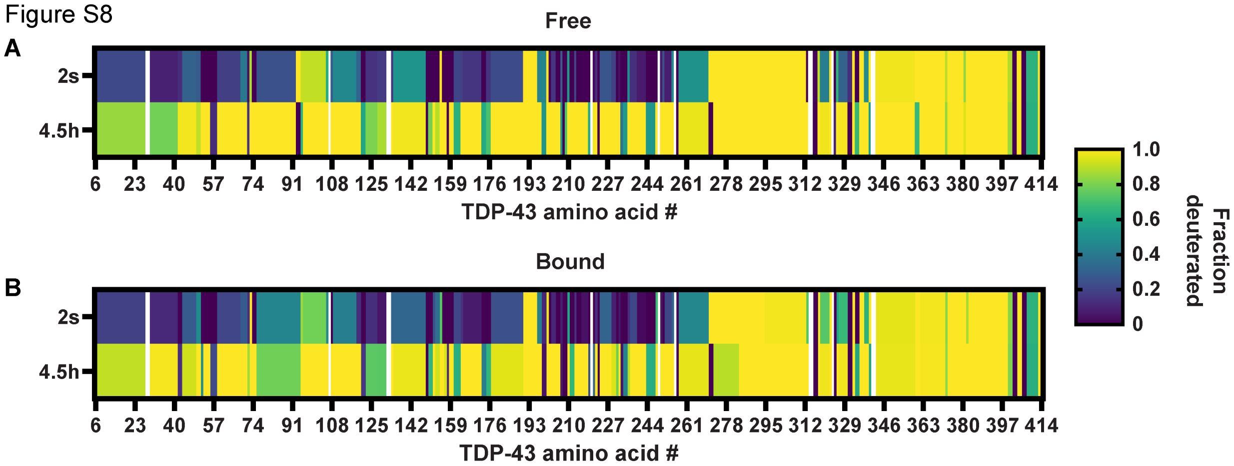

Fig. S8. Hydrogen/deuterium-exchange for TDP-43^{5FL} in the absence or presence of Clip34 RNA. (A, B) Heatmaps displaying hydrogen/deuterium-exchange for each TDP-43^{5FL} amino acid in the free (A) and bound (B) states at each timepoint, normalized so that 1 represents fully deuterated and 0 represents not deuterated. White spaces represent small gaps in coverage. Sub-localization between peptides to determine the exchange value at each amino acid was performed by HDExaminer. 2 s timepoints were collected utilizing pH 6.0 buffer, whereas 4.5 h timepoints were collected utilizing pH 7.0 buffer.

Figure S9

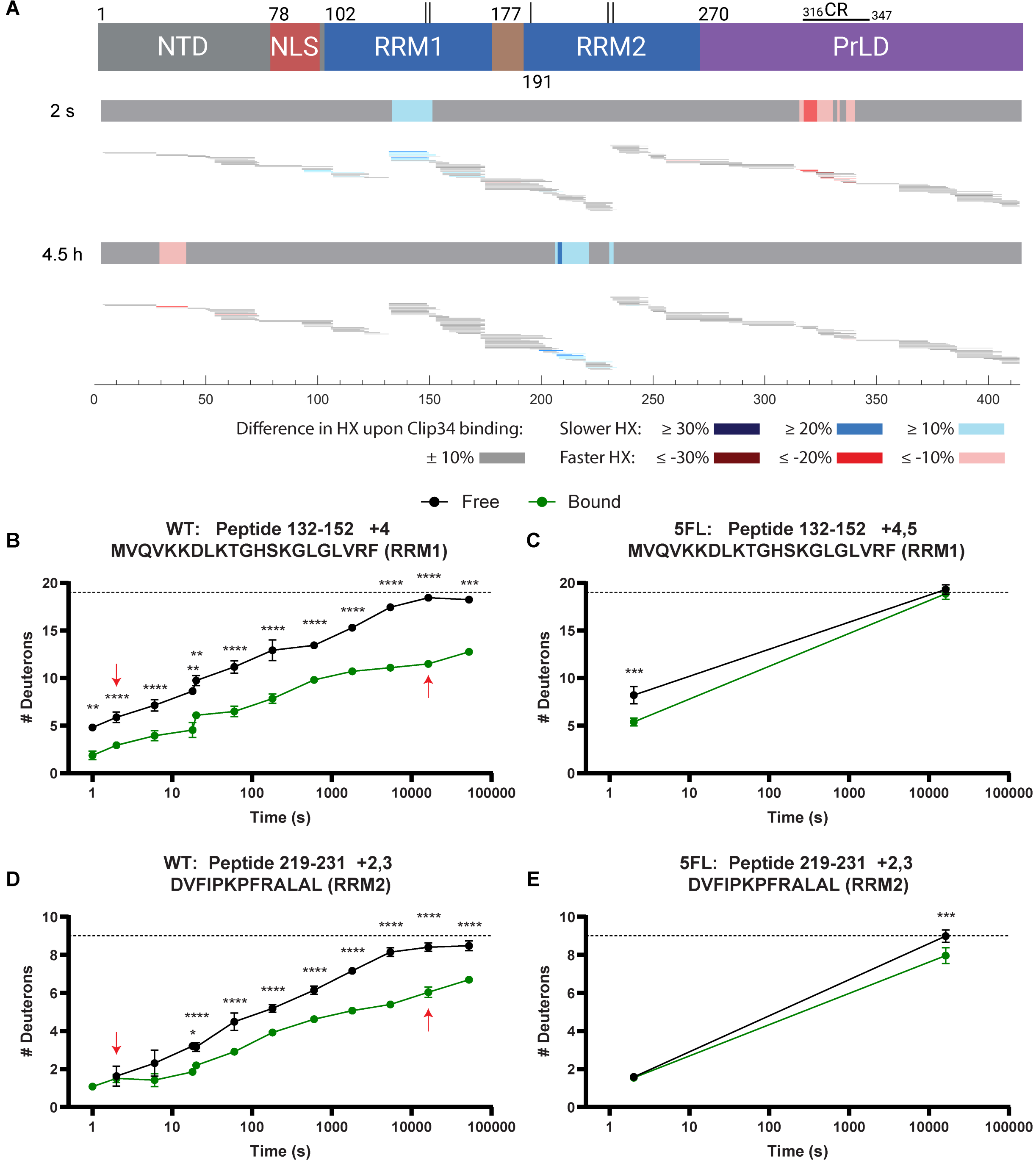

Fig. S9. Hydrogen/deuterium-exchange reveals that Clip34 induces markedly reduced stabilization of the RRMs of TDP-43^{5FL} compared to WT TDP-43. (A) *Top:* domain map of TDP-43^{5FL}, aligned with data underneath. *Bottom:* For each timepoint, residues are colored corresponding to the consensus percentage difference in exchange between the Clip34-bound (2:1::[Clip34]:[TDP-43^{5FL}]) and free states as indicated in the legend, as calculated by manual analysis of percentage exchange differences for all peptides including an amino acid. White spaces represent small coverage gaps. Aligned beneath each consensus percentage difference map are peptides analyzed at that timepoint, with percentage differences in exchange between

Clip34-bound and free states for each peptide colored as indicated in the legend. Amino acid number is indicated on the axis below. **(B, C)** HX for a representative RRM1 peptide for WT TDP-43 (B) or TDP-43^{5FL} (C). The dashed line represents the fully-deuterated condition. Red arrows are included in (B) as a visual reference for the timepoints matching timepoints collected for TDP-43^{5FL} shown in (C). Data are mean ± SD (3-7 replicates run on mass spectrometry per timepoint; n=3-8 replicates per peptide per timepoint based on medium or high confidence peptide detection across one or two charge states as indicated in graph titles; some error bars are too small to visualize; Welch's t-test comparing bound and free at each timepoint; $^{**}p < 0.01$, $^{***}p < 0.001$, $^{****}p < 0.0001$). **(D, E)** HX for a representative RRM2 peptide for WT TDP-43 (D) or TDP-43^{5FL} (E). The dashed line represents the fully-deuterated condition. Red arrows are included in (D) as a visual reference for the timepoints matching timepoints collected for TDP-43^{5FL} shown in (E). Data are mean ± SD (3-7 replicates run on mass spectrometry per timepoint; n=1-10 replicates per peptide per timepoint based on medium or high confidence peptide detection across two charge states; some error bars are too small to visualize; Welch's t-test comparing bound and free at each timepoint; $^{*}p < 0.05$, $^{***}p < 0.001$, $^{****}p < 0.0001$). Small-magnitude stabilizing effects of Clip34 on TDP-43^{5FL}, greatly reduced in magnitude compared to effects seen on WT TDP-43, agree well with the concept of strongly impaired binding affinity of TDP-43^{5FL} and consequent weak, transient binding.

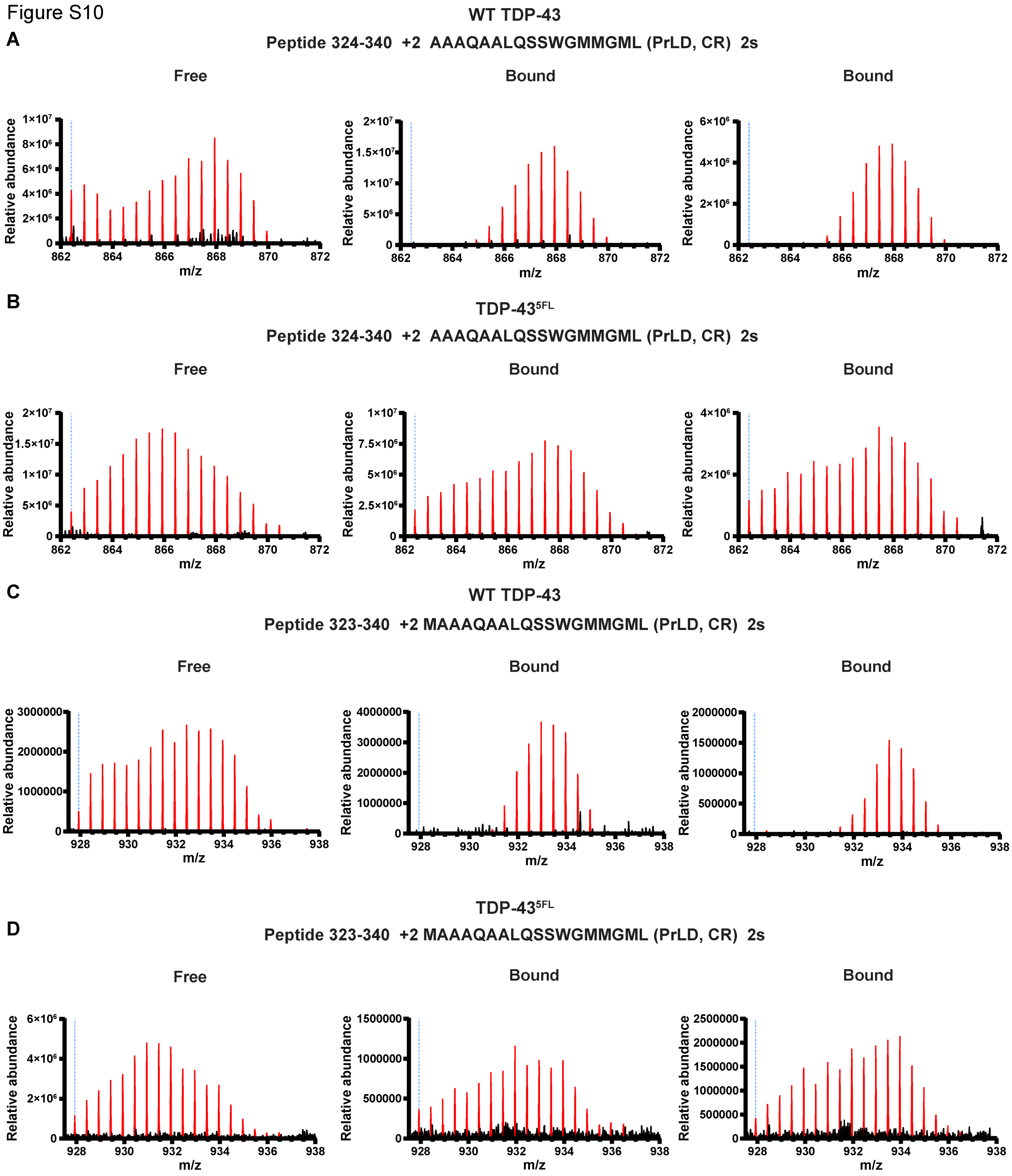

Fig. S10. Mass spectra for TDP-43^{5FL} CR peptides retain bimodality in the presence of Clip34. (A-D) Raw mass spectra data, with signal corresponding to the appropriate peptide as determined by appropriate m/z values colored red, and noise from overlapping peptide(s) colored black. The blue dashed line serves as a visual guide indicating the monoisotopic peak. Representative spectra at the 2 s timepoint for the free and bound states are displayed for the indicated peptide in the CR of the PrLD for WT TDP-43 (A, C) and TDP-43^{5FL} (B, D). WT TDP-43 spectra in (A) or (C) are the same spectra shown in Fig. 2G and fig. S7A or fig. S7C, respectively (except the rightmost spectrum in (C) is newly visualized), displayed for visual reference. Mass spectra for the free state are slightly shifted left for TDP-43^{5FL} compared to WT TDP-43, indicating that F147, F149, F194, F229, and F231 may play a role in priming unfolding of the CR in the apo state of TDP-43. Mass spectra for samples containing Clip34 display clear bimodality for TDP-43^{5FL}, indicating the presence of a stabilized population (corresponding to the α-helical form of the CR) and a destabilized population (corresponding to the unstructured form of the CR), whereas WT TDP-43 spectra only display the destabilized, unstructured form.

Figure S11

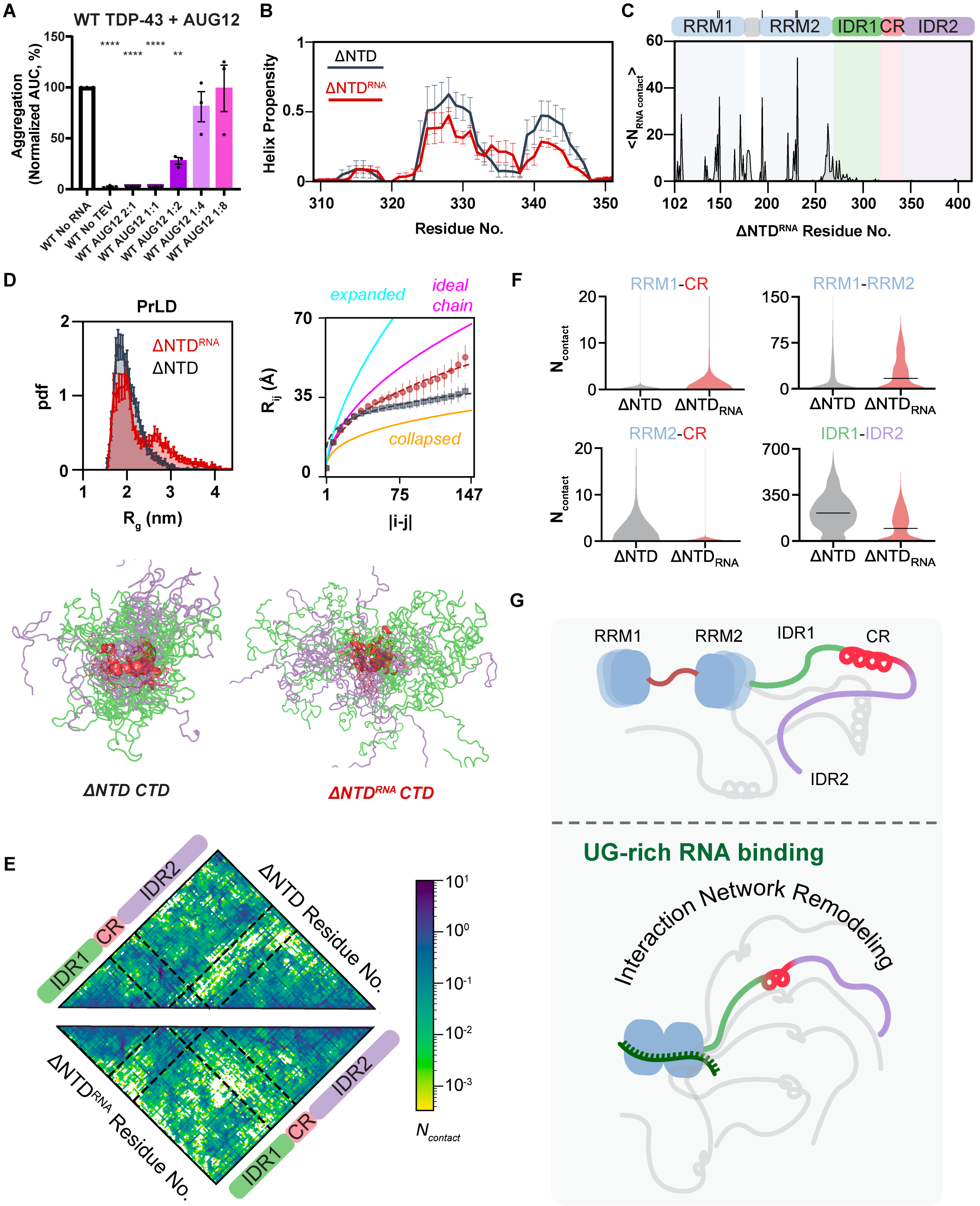

Fig. S11. Molecular insights from atomistic molecular dynamics simulations (45 µs) into the allosteric coupling between the TDP-43 RRMs, PrLD, and RNA. (A) Standardized turbidity AUC data for aggregation prevention assays with 5 µM WT TDP-43 and AUG12 RNA, normalized to the No RNA condition. Data are mean ± SEM (n=3; one-way ANOVA with Dunnett's correction comparing to No RNA; $^{**}p < 0.01$, $^{****}p < 0.0001$). **(B)** CR helix propensity in ΔNTD constructs without (black) and with RNA (red). Data are mean ± SEM. **(C)** Contacts between protein residues and RNA nucleotides across TDP-43 domains. Data show the mean. The domain map corresponds to data in the lower plot. Vertical lines mark the five Phe residues (F147, F149, F194, F229, and F231) within RRM1 and RRM2 that are mutated to Leu in TDP-43^{5FL}. **(D)** PrLD conformational changes upon RNA binding. *Left:* Radius of gyration (R_g) distributions. *Right:* Average intrachain C_α distances (R_{ij}) as a function of sequence separation ($|i-j|$). Reference scaling laws for ideal chain (magenta, $\nu=1/2$), self-avoiding random walk (cyan, $\nu=3/5$), and collapsed globule (yellow, $\nu=1/3$) are shown, with b=5.5 Å. Representative PrLD structures are shown below. **(E)** Intramolecular contact maps for the PrLD in the absence (upper diagonal) and presence of RNA (lower diagonal). **(F)** Distributions of the number of contacts between RRM1-CR, RRM2-CR, RRM1-RRM2, and IDR1-IDR2 domains. Violin plots display the full probability densities with mean shown as a solid black line, highlighting differences between interaction patterns in the absence and presence of RNA. **(G)** Model of allosteric crosstalk between the TDP-43 RRMs, PrLD, and RNA. Without RNA, the RRMs show high conformational heterogeneity, whereas the PrLD is compact with a helical CR. RNA binding through conserved Phe residues leads to a more compact tandem RRM ensemble, protecting RRM1 from adopting misfolded states. IDR1-RNA electrostatic interactions remodel the interaction network, disrupting IDR1-IDR2 contacts and CR helicity.

Figure S12

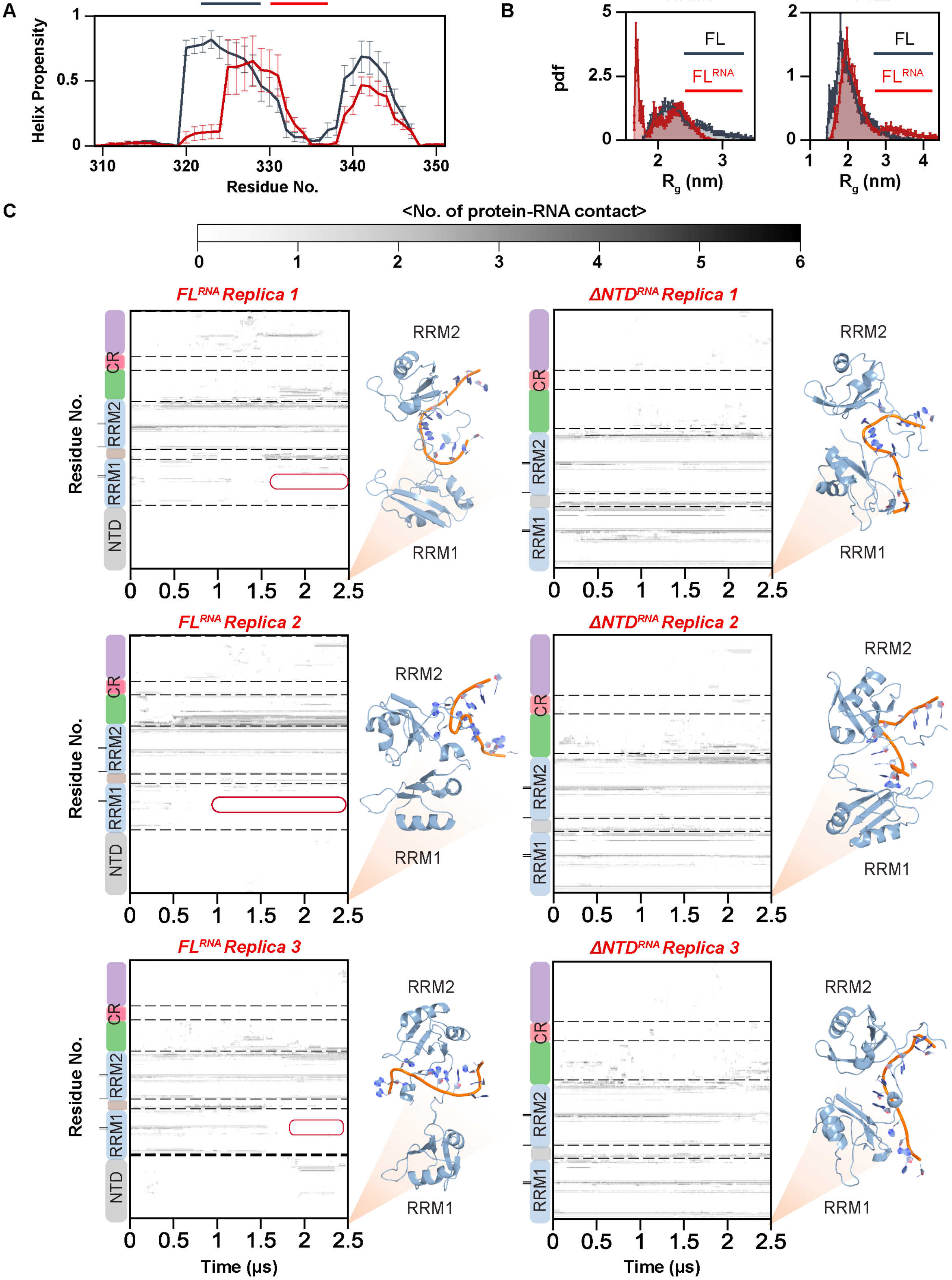

Fig. S12. Full-length TDP-43 simulations show that the NTD destabilizes RNA binding. (A) Helix propensity of the conserved region (CR, residues: 319-341) without (black) and with RNA (red). Data are mean ± SEM across three replicates. In the presence of RNA, CR secondary structure is impaired. **(B)** Radius of gyration (R_g) distributions for backbone atoms of tandem RRMs (left, residues 102-176 and 192-269) and the PrLD (right, residues 270-414). RNA binding leads the tandem RRMs to be more compact while expanding the PrLD. **(C)** RNA contact profiles over time for full-length (left) and ΔNTD (right) TDP-43. Heat maps show contacts between RNA and each protein residue, with contacts defined as heavy atoms within 4.5 Å. The presence of the NTD destabilizes RNA binding, leading to dissociation in FL simulations. Representative structures from the final frame of each trajectory show only tandem RRMs and RNA for clarity.

Figure S13

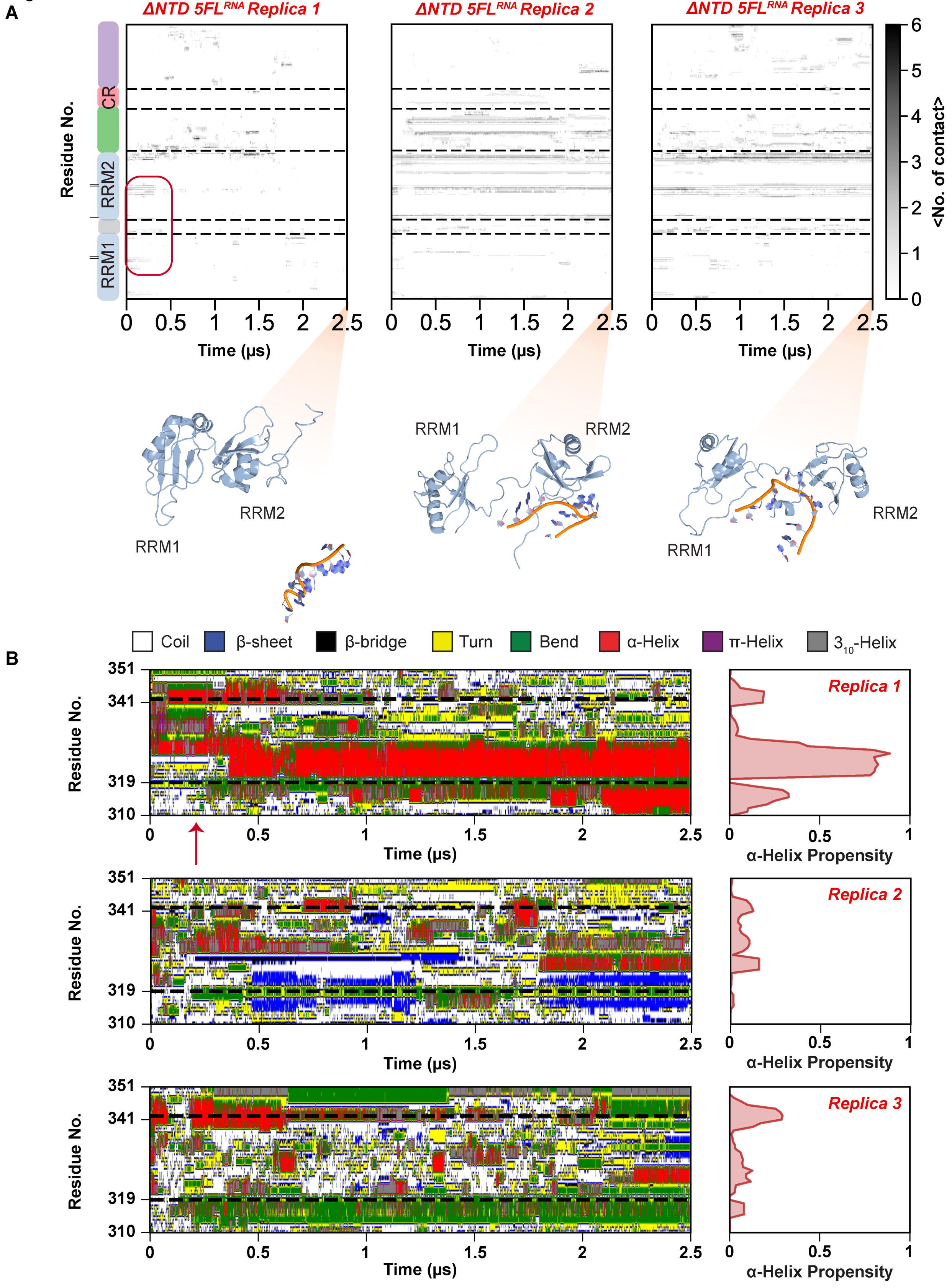
A
ΔNTD 5FL^{RNA} Replica 1
ΔNTD 5FL^{RNA} Replica 2
ΔNTD 5FL^{RNA} Replica 3
Residue No.
CR
RRM2
RRM1
0
0.5
1
1.5
2
2.5
Time (μs)
6
5
4
3
2
1
0
<No. of contact>
RRM1
RRM2
B
Coil
β-sheet
β-bridge
Turn
Bend
α-Helix
π-Helix
3_{10}-Helix
351
341
319
310
Residue No.
Time (μs)
α-Helix Propensity
Replica 1
Replica 2
Replica 3

Fig. S13. TDP-43^{5FL} mutations impair RNA binding and restore CR helicity. (A) RNA contact profiles over time for ΔNTD TDP-43^{5FL} starting from the RNA-bound state. Heat maps show contacts between RNA and each protein residue (heavy atoms within 4.5 Å). Representative structures show tandem RRMs-RNA relative positioning at the end of each simulation. **(B)** Secondary structure evolution of PrLD residues 310-350 over time (left) and helix propensity distributions (right). Disrupted Phe-RNA interactions lead to RNA dissociation and CR-helix reformation as evident from Replica 1, supporting that RNA binding is required for allosteric CR destabilization.

Figure S14

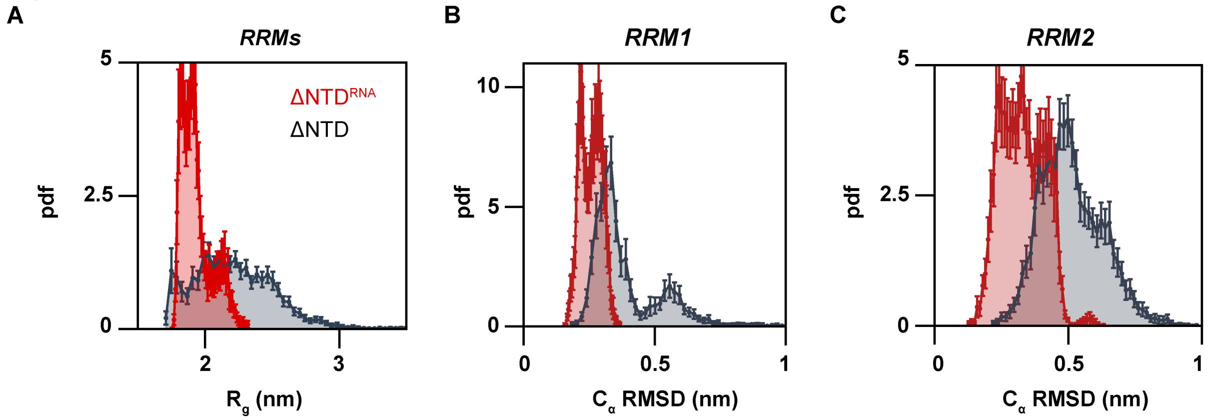

Figure S14. Characterization of the structural changes in the conformational ensemble of the tandem RRMs. (A) Radius of gyration (R_g) distributions for backbone atoms of the tandem RRMs (residues 102-176 and 192-269) without (black) and with RNA (red). **(B)** Root mean square deviation (RMSD) distribution for RRM1 C_α atoms (residues 102-176). **(C)** RMSD distribution for RRM2 C_α atoms (residues 192-269).

Figure S15

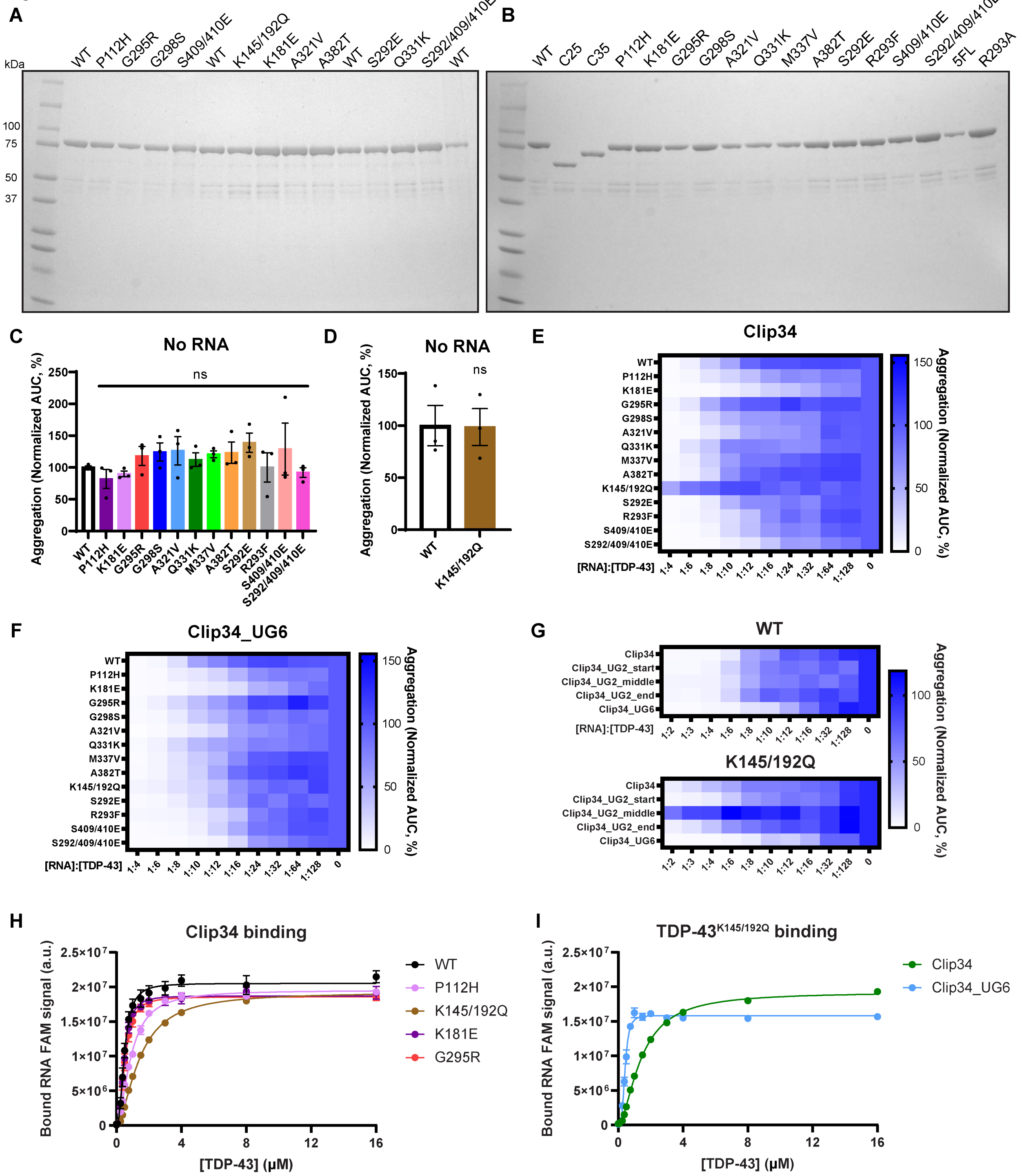

Fig. S15. Clip34 and Clip34_UG6 effectively prevent aggregation of diverse disease-linked TDP-43 variants. (A, B) 4-20% Tris-HCl SDS-PAGE gels loaded with 1 μg of each indicated purified TDP-43 variant and subsequently stained with Coomassie Brilliant Blue. **(C, D)** AUC values for No RNA conditions for all examined TDP-43 variants, normalized to WT. For each graph, all data for each replicate were collected within the same experiment. Data are mean ± SEM (n=3; one-way ANOVA with Dunnett's correction comparing to WT (C) or unpaired t-test (D)). **(E, F)** Heatmaps displaying the mean normalized AUC value at each tested molar concentration ratio of Clip34 (E) or Clip34_UG6 (F) to TDP-43, across individual replicates of aggregation assays. Data is normalized to the respective variant's No RNA condition. These data were utilized to calculate the IC_{50} values depicted in Fig. 3, B and C. **(G)** Heatmaps displaying the mean normalized AUC value at each tested molar concentration ratio of Clip34 variants to WT TDP-43 or TDP-43$^{K145/192Q}$, across individual replicates of aggregation assays. Data are normalized to the respective variant's No RNA condition. These data were utilized to calculate the IC_{50} values depicted in Fig. 3, E and F. **(H)** Bound 5' 6-FAM Clip34 signal for EMSAs performed with the indicated TDP-43-MBP-His variants. These are the summary data corresponding to K_D values calculated from individual replicates, shown in Fig. 3G. WT data is the same as shown in Fig. 1J and fig. S2D. Data are mean ± SEM (n=2-3; shown is the nonlinear regression: [agonist] vs. response with variable slope, of the combined replicates). **(I)** Bound 5' 6-FAM RNA signal for EMSAs performed with TDP-43$^{K145/192Q}$. These are the summary data corresponding to K_D values calculated from individual replicates, shown in Fig. 3H. The Clip34 curve data are the same as shown in (H), included for reference. Data are mean ± SEM (n=3; shown is the nonlinear regression: [agonist] vs. response with variable slope, of the combined replicates).

Figure S16

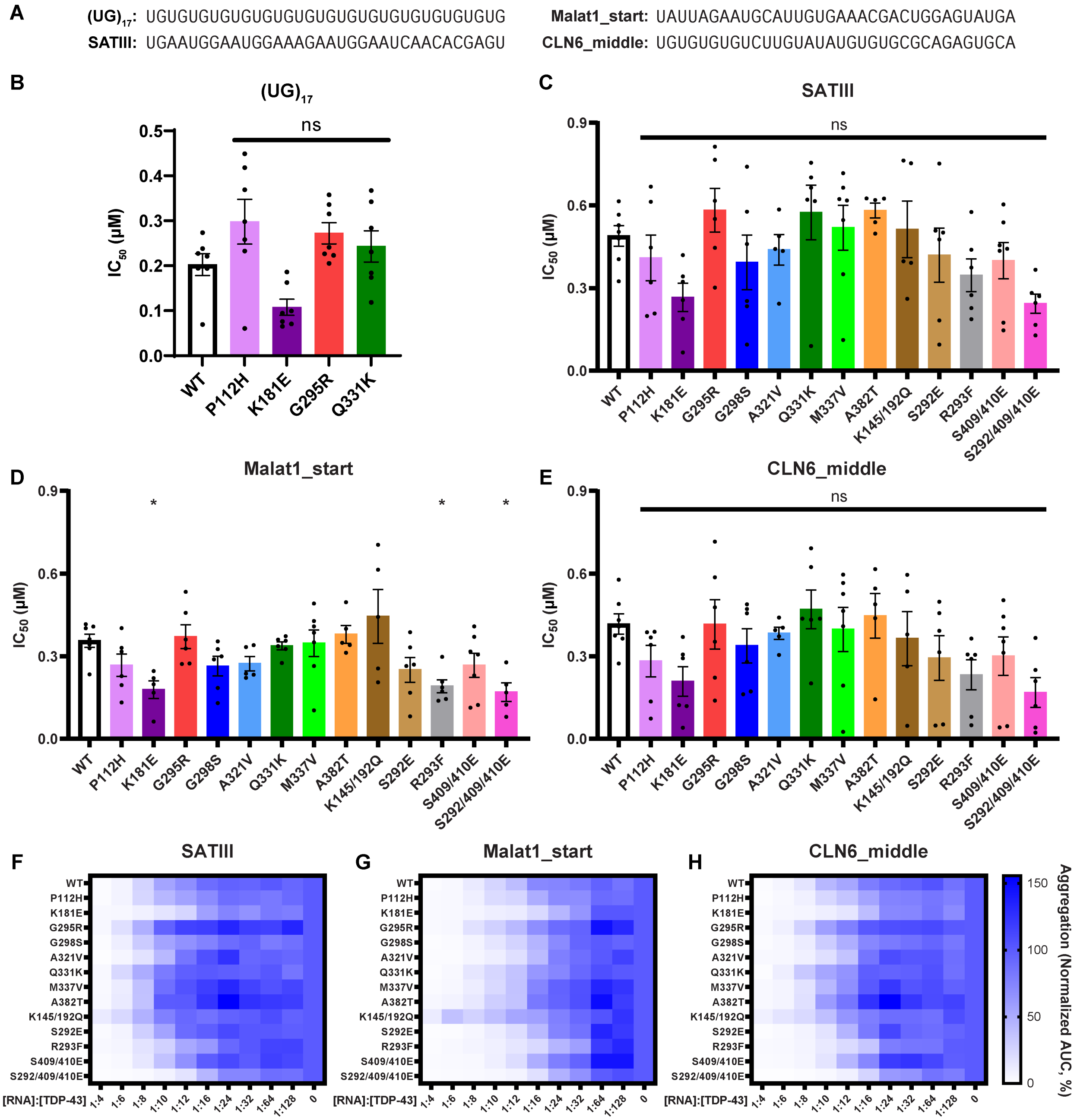

Fig. S16. Malat1_start, SATIII, CLN6_middle, and (UG)$_{17}$ effectively prevent aggregation of diverse disease-linked TDP-43 variants. (A) RNA sequences of tested RNAs. **(B)** IC$_{50}$ values calculated for the indicated TDP-43 variants with (UG)$_{17}$. Data are mean ± SEM (n=7; one-way ANOVA with Dunnett's correction comparing to WT). **(C-E)** IC$_{50}$ values for SATIII (C), Malat1_start (D), or CLN6_middle (E) RNAs with each TDP-43 variant. Data are mean ± SEM (n=5-7; one-way ANOVA with Dunnett's correction comparing to WT; *$p < 0.05$). **(F-H)** Heatmaps displaying the mean normalized AUC value at each tested molar concentration ratio of SATIII (F), Malat1_start (G), or CLN6_middle (H) RNAs to TDP-43, across individual replicates of aggregation assays. Data are normalized to the respective variant's No RNA condition. These data were utilized to calculate the IC$_{50}$ values depicted in (C-E).

Figure S17

A

Clip34: GAGAGAGCGCGUGCAGAGACUUGGUGGUGCAUAA
Clip34_UG6: GAGAGAGCGCGUGUGUGUGUGUGGUGGUGCAUAA
SATIII: UGAAUGGAAUGGAAAGAAUGGAAUCAACACGAGU
Malat1_start: UAUUAGAAUGCAUUGUGAAACGACUGGAGUAUGA
Malat1_middle: UGUGAAACGACUGGAGUAUGAUUAAAAGUUGUGU
Malat1_end: GAGUAUGAUUAAAAGUUGUGUUCCCCAAUGCUUG
CLN6_start: UCGUGUGUGUGUGUGUGUGUGUCUUGUAUAUGUG
CLN6_middle: UGUGUGUGUCUUGUAUAUGUGUGCGCAGAGUGCA
CLN6_end: UAUAUGUGUGCGCAGAGUGCAUCAUUUUCAGACU
***LTR-III*:** GGGAGGCGUGGCCUGGGCGGGACUGGGG

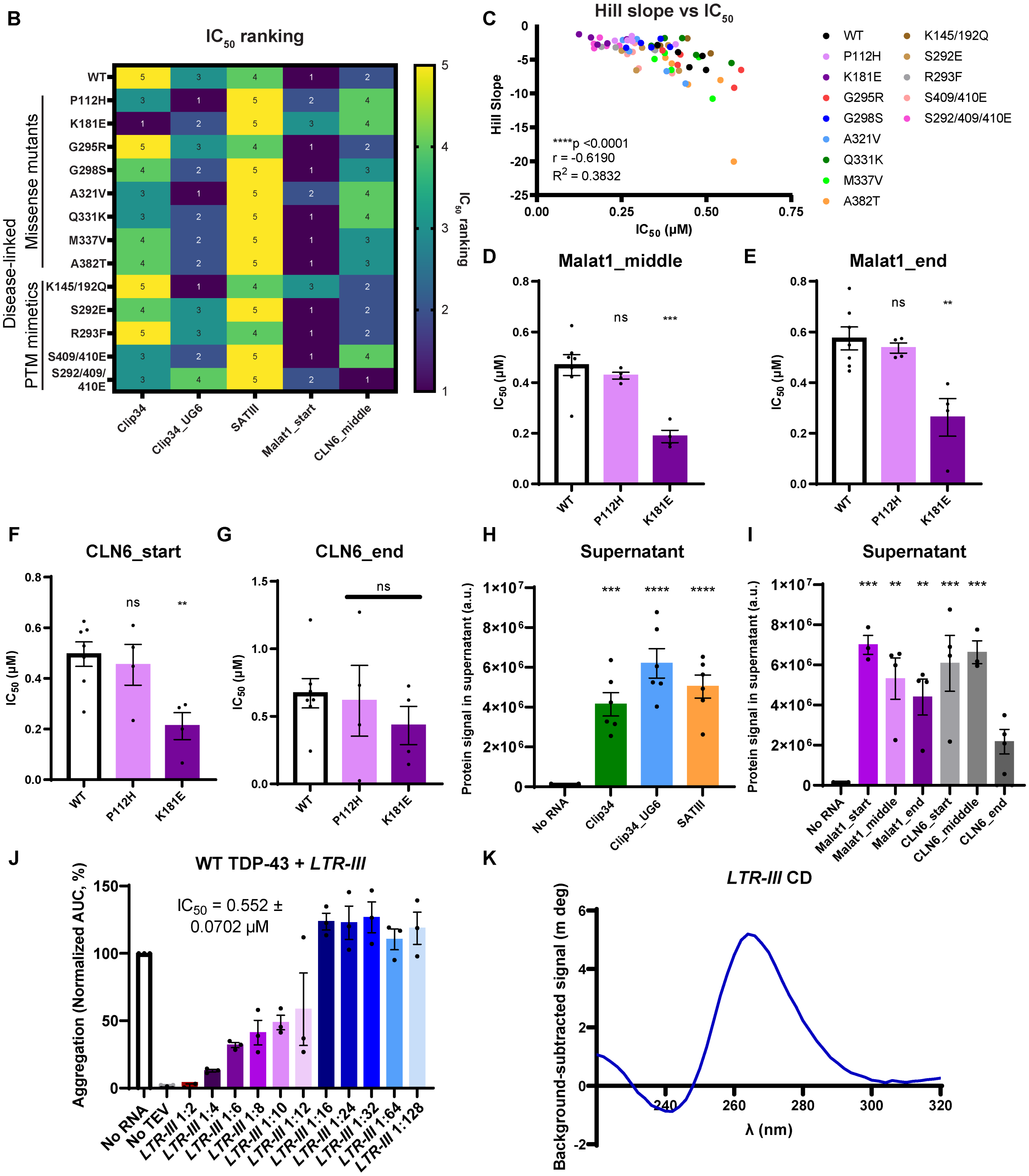

Fig. S17. Several short RNA chaperones effectively prevent aggregation of diverse disease-linked TDP-43 variants. (A) RNA sequences of tested RNAs. **(B)** Heatmap displaying rankings of the IC_{50} data shown in Fig. 4B. Rankings of RNA IC_{50} values are determined for each TDP-43 variant, with a ranking of 1 corresponding to the "best" (lowest IC_{50} value), and a ranking of 5 corresponding to the “worst” (highest IC_{50} value). **(C)** The IC_{50} for each TDP-43 variant:RNA pair is plotted against the hill slope for that same pair, as calculated by nonlinear regression: [inhibitor] vs. normalized response with variable slope, from the combined data of all replicates (Pearson correlation; ****$p < 0.0001$). **(D-G)** IC_{50} values calculated for the indicated TDP-43 variants with Malat1_middle (D), Malat1_end (E), CLN6_start (F), or CLN6_end (G) RNAs. Data are mean ± SEM (n=4-7; one-way ANOVA with Dunnett’s correction comparing to WT; **$p < 0.01$, ***$p < 0.001$). **(H, I)** Quantification of the WT TDP-43 signal in the supernatant after sedimentation was performed at the end timepoint of aggregation assays. 4-20% Tris-HCl SDS-PAGE gels were loaded with equal volumes of supernatant from each sample, and subsequently stained with Coomassie Brilliant Blue. Replicates within each graph were collected within the same experiment. Data are mean ± SEM (n=3-6; one-way ANOVA with Dunnett’s correction comparing to No RNA; **$p < 0.01$, ***$p < 0.001$, ****$p < 0.0001$). **(J)** AUC of turbidity data for WT TDP-43 with annealed *LTR-III* RNA, normalized to the No RNA condition. Data are mean ± SEM (n=2-3). **(K)** Circular dichroism spectrum for 5 μM *LTR-III* RNA after annealing.

Figure S18

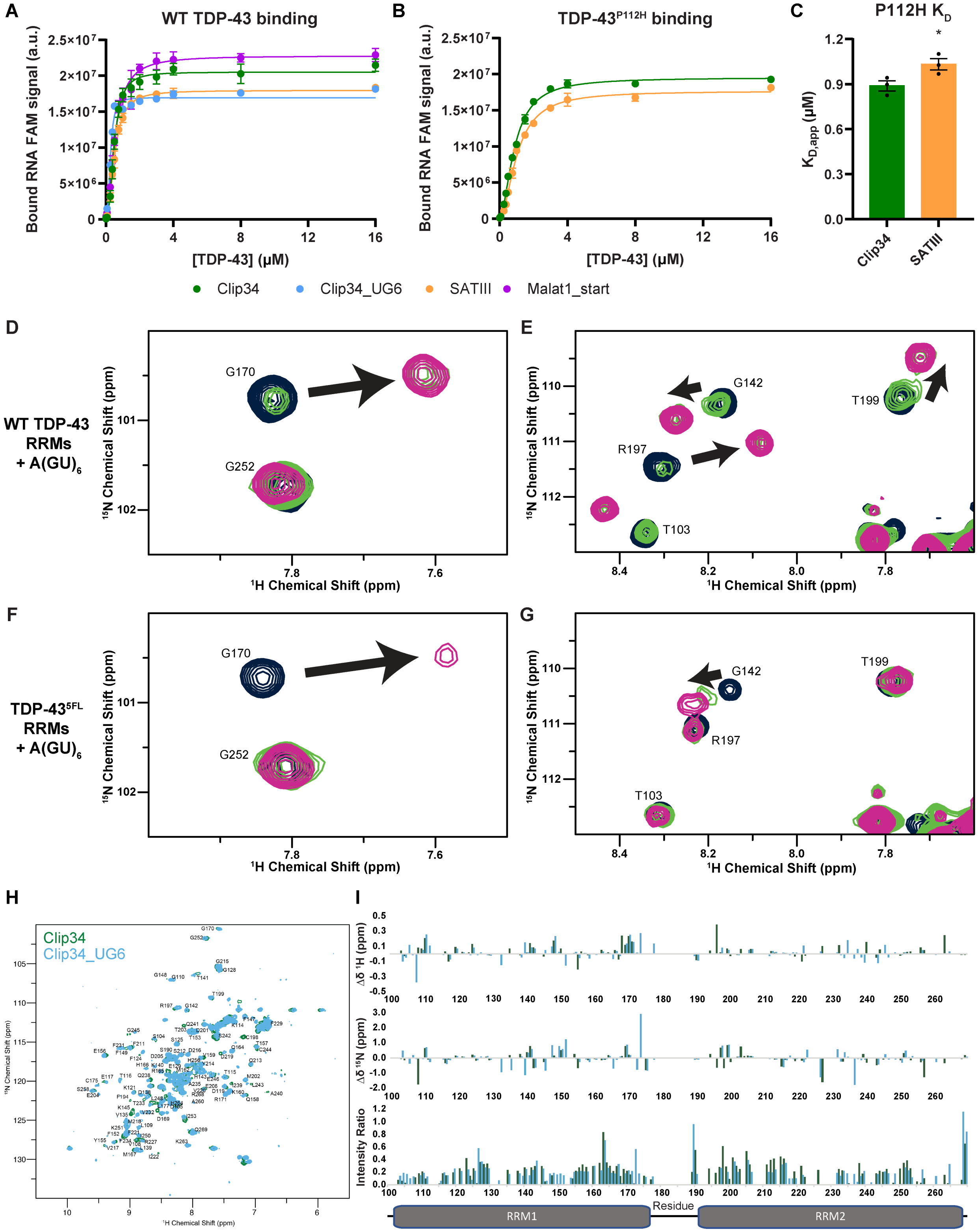

Fig. S18. Short RNA chaperone engagement of the TDP-43 RRMs. (A, B) Bound 5’ 6-FAM RNA signal for EMSAs with WT TDP-43 (A) or TDP-43^{P112H} (B). Clip34 data are the same as in Fig. 1J, fig. S2D, and fig. S15H. Data are mean ± SEM (n=2-4; shown is the nonlinear regression: [agonist] vs. response with variable slope, of combined replicates). **(C)** Apparent K_D

values from bound 5’ 6-FAM RNA signal, from individual EMSA replicates with TDP-43^{P112H}, corresponding to summary data in (B). Clip34 data is the same as in Fig. 3G. Data are mean ± SEM (n=3; unpaired t-test; $^{*}p < 0.05$). **(D-G)** Overlay of ^{1}H-^{15}N heteronuclear single quantum coherence (HSQC) spectra of WT (D, E) and TDP-43^{5FL} (F, G) RRMs with A(GU)$_6$ RNA (blue, no RNA; green, 0.5:1::[RNA]:[TDP-43]; pink, 1:1::[RNA]:[TDP-43]). Black arrows indicate chemical shift perturbation direction upon RNA binding. Although similar chemical shift perturbations at many known RNA binding sites are seen for WT and TDP-43^{5FL} RRMs with an equivalent molar amount of RNA (pink), broad resonances are observed for TDP-43^{5FL}, suggesting enhanced chemical exchange rate, consistent with weaker binding. No shifts are seen for some resonances of TDP-43^{5FL} that shift for WT (e.g., T199, T103), suggesting fewer binding residues in TDP-43^{5FL} RRMs. At 0.5 molar equivalents (green), two peaks are observed for several resonances showing large shifts for WT TDP-43, consistent with slow exchange and tight binding, while peaks are broadened beyond detection (G170) or show approximately half the shift observed at 1 molar equivalent (G142), consistent with intermediate/fast exchange due to weaker binding than for WT. **(H)** Overlay of ^{1}H-^{15}N HSQC spectra of WT TDP-43 RRMs with Clip34 (green, 2:1::[Clip34]:[TDP-43]) and Clip34_UG6 (blue, 2:1::[Clip34_UG6]:[TDP-43]) RNAs. **(I)** ^{1}H and ^{15}N chemical shift perturbations ($\Delta\delta^{1}H$ (*top*) and $\Delta\delta^{15}N$ (*middle*)), and intensity ratios (*bottom*) of WT TDP-43 RRMs upon binding of Clip34 (green) and Clip34_UG6 (blue) RNA. TDP-43 RRMs domain map is aligned to x-axes.

Figure S19

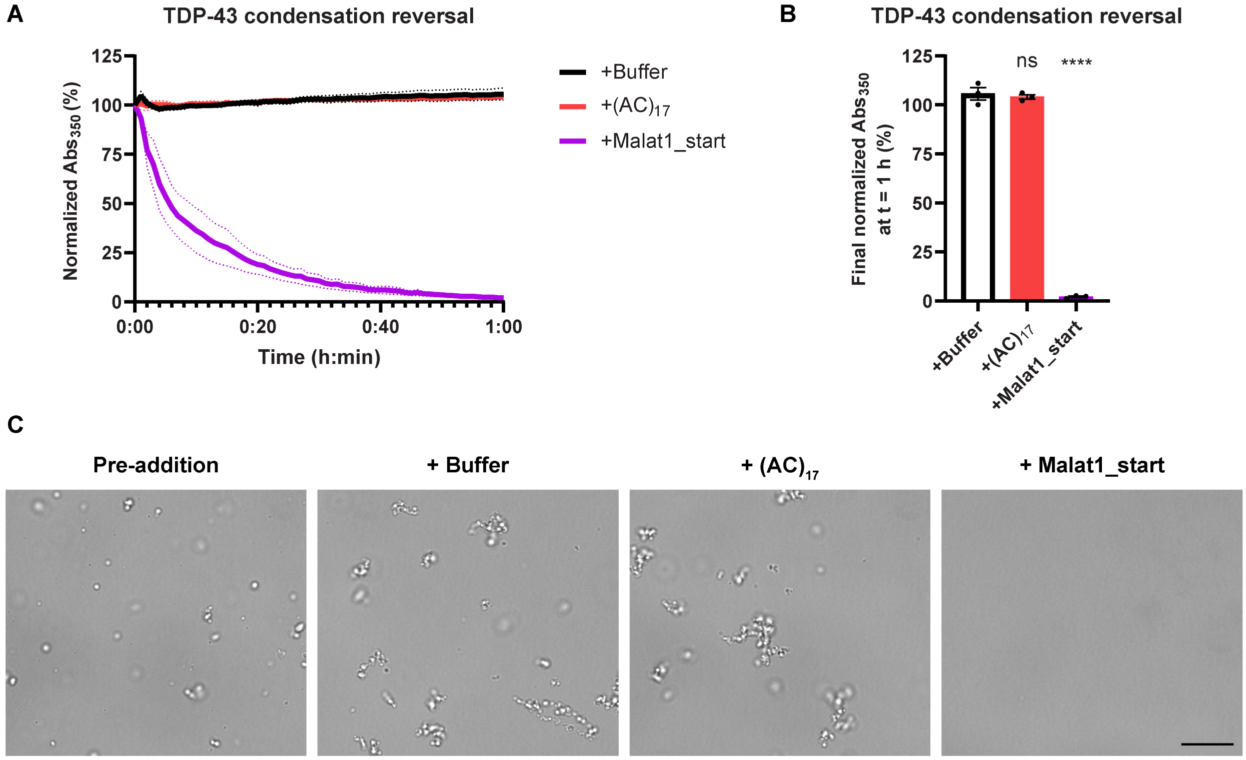

Fig. S19. Malat1_start dissolves preformed TDP-43 condensates. 4.22 µM TDP-43-MBP-His was incubated with TEV protease in the absence of RNA for 1.5 h, producing preformed TDP-43 condensates for which turbidity measurements had achieved plateau. After 1.5 h, RNA or buffer was added, resulting in final concentrations of 0 or 2 µM RNA, 4 µM TDP-43, 150 mM NaCl, 20 mM HEPES-NaOH pH 7.4, 1 mM DTT, 10 µg/mL TEV protease. Turbidity measurements at 350 nm were collected for 1 h post-addition. **(A)** Buffer-standardized turbidity measurements at 350 nm were normalized to the respective pre-addition reading for each sample. Data are mean (solid lines) ± SEM (dashed lines) (n=3). **(B)** Final normalized turbidity measurements after 1 h of incubation post-addition. Data are mean ± SEM (n=3; one-way ANOVA with Dunnett's correction comparing to +Buffer; ****$p < 0.0001$). **(C)** Representative 100x brightfield images of samples after 1.5 h of condensate formation (pre-addition) or after an additional 1 h post-addition. Scale bar indicates 10 µm.

Figure S20

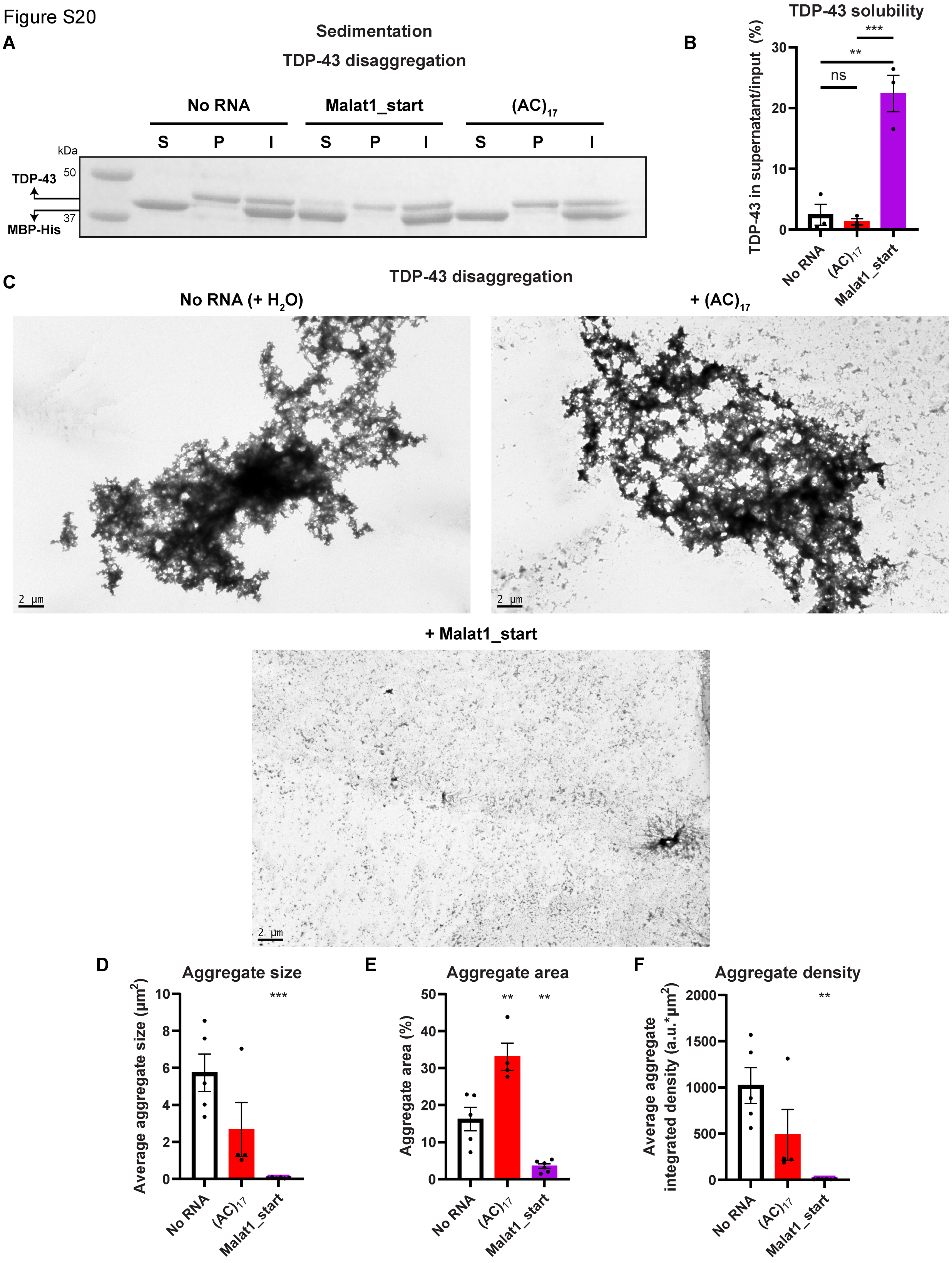

Fig. S20. Malat1_start solubilizes TDP-43 aggregates. 4 µM TDP-43-MBP-His was incubated with TEV protease in the absence of RNA for 4 h, producing preformed TDP-43 aggregates for which turbidity measurements had achieved plateau. After 4 h, RNA or water was added, resulting in final concentrations of 0 or 40 µM RNA, 3.648 µM TDP-43, 136.8 mM NaCl, 18.24 mM HEPES-NaOH pH 7.0, 0.912 mM DTT. Reactions were then incubated for 16 h before assessment at the end timepoint by sedimentation and electron microscopy. **(A)** Representative 4-20% Tris-HCl SDS-PAGE gel loaded with equal volumes of supernatant (S), pellet (P), or input (I) from each sample, and subsequently stained with Coomassie Brilliant Blue. **(B)** Quantification of the TDP-43 signal in the supernatant as a percentage of the input of that sample after sedimentation. Data are mean ± SEM (n=3; one-way ANOVA with Tukey's correction; **$p < 0.01$, ***$p < 0.001$). **(C)** Representative electron micrographs of samples collected at the end timepoint of the disaggregation assay. Scale bar indicates 2 µm. **(D-F)** Quantification of micrographs performed utilizing ImageJ, including the average size of aggregates in μm^2 (D), the percentage of micrograph area occupied by aggregates (E), and the average integrated density of aggregates (F). Data are mean ± SEM (n=4-6 micrographs per condition; one-way ANOVA with Dunnett's correction comparing to No RNA; **$p < 0.01$, ***$p < 0.001$).

Figure S21

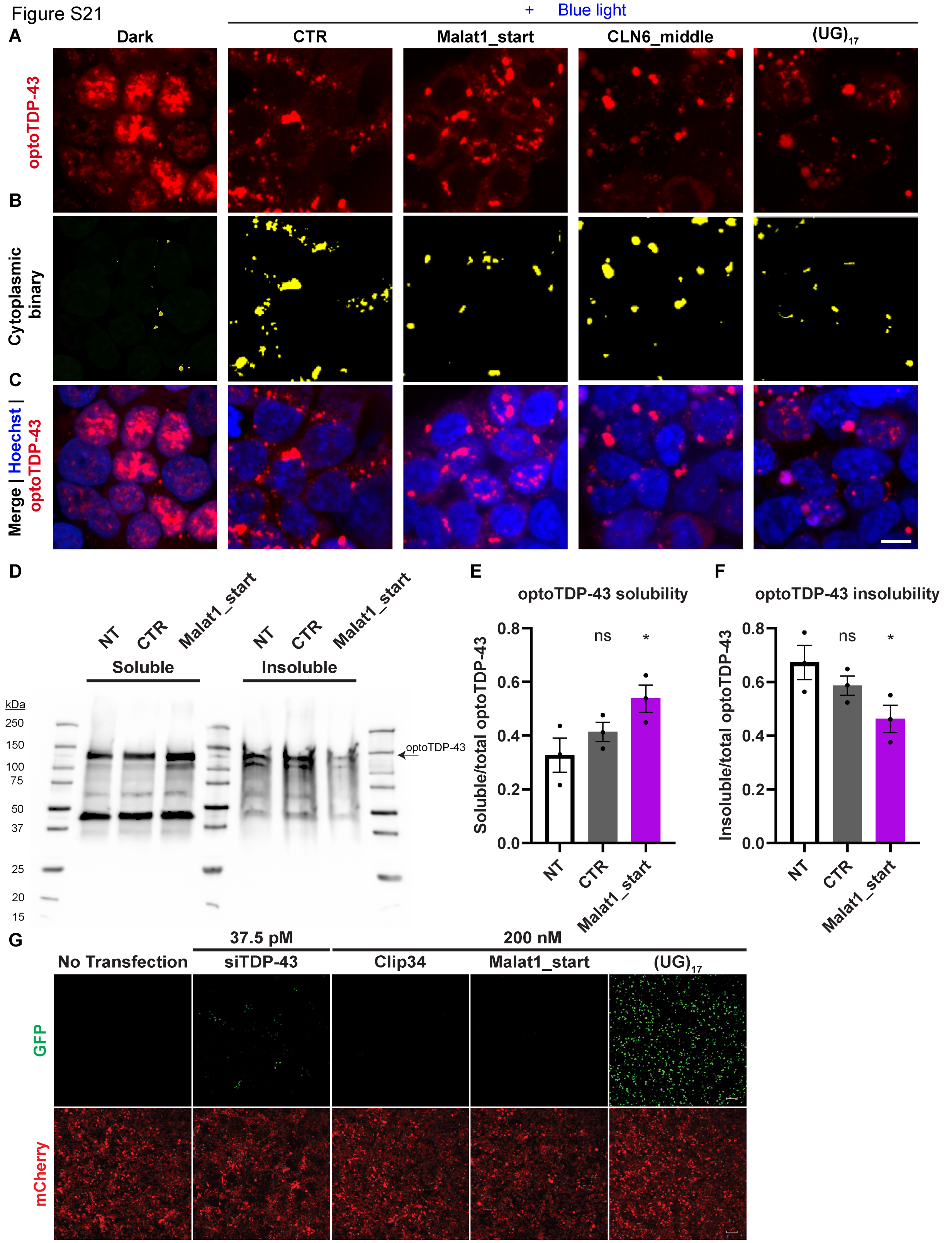

Fig. S21. Clip34 and Malat1_start mitigate aberrant TDP-43 phenotypes in an optogenetic human cell model without interfering with TDP-43 function. (A-C) OptoTDP-43 stable HEK293 cells were treated with the indicated RNA, followed by blue light exposure to induce Cry2olig oligomerization, and imaged after fixation. Representative images corresponding to quantification in Fig. 5B, for optoTDP-43 (A), the binary signal of cytoplasmic optoTDP-43 puncta (B), and the merged image showing optoTDP-43 and Hoechst (C). Images of cells without blue light exposure (Dark) are shown as references for the baseline cellular appearance of optoTDP-43 without induction of oligomerization. Scale bar indicates 10 µm. **(D-F)** OptoTDP-43 stable HEK293 cells were treated with the indicated RNA, followed by blue light exposure and protein fractionation into RIPA-soluble or RIPA-insoluble (urea-soluble) fractions. A representative blot stained by TDP-43 antibody with the optoTDP-43 band indicated (D) was quantified as soluble/total optoTDP-43 (soluble + insoluble) (E) and insoluble/total optoTDP-43 (soluble + insoluble) (F). Data are mean ± SEM (n=3; one-way ANOVA with Dunnett's correction; $^{*}p < 0.05$). **(G)** Stable HEK293 cells with inducible CUTS biosensor were transfected with 200 nM of Clip34, Malat1_start, and $(UG)_{17}$ RNA oligos for 48 hours in doxycycline supplemented media (1000 ng/mL). The cells were also reverse transfected with a low dose (37.5 pM) siRNA of TDP-43 for 72 hours, together with 48 hours of doxycycline as a positive control. Cells experiencing TDP-43 loss of function will have green nuclei due to the expression of GFP-NLS that would ordinarily be repressed by a TDP-43-regulated cryptic exon (*47*). Live-imaging of CUTS HEK cells transfected with siRNA of TDP-43, Clip34, Malat1_start, and $(UG)_{17}$. Green = GFP; red = mCherry. Scale bar indicates 100 µm.

Figure S22

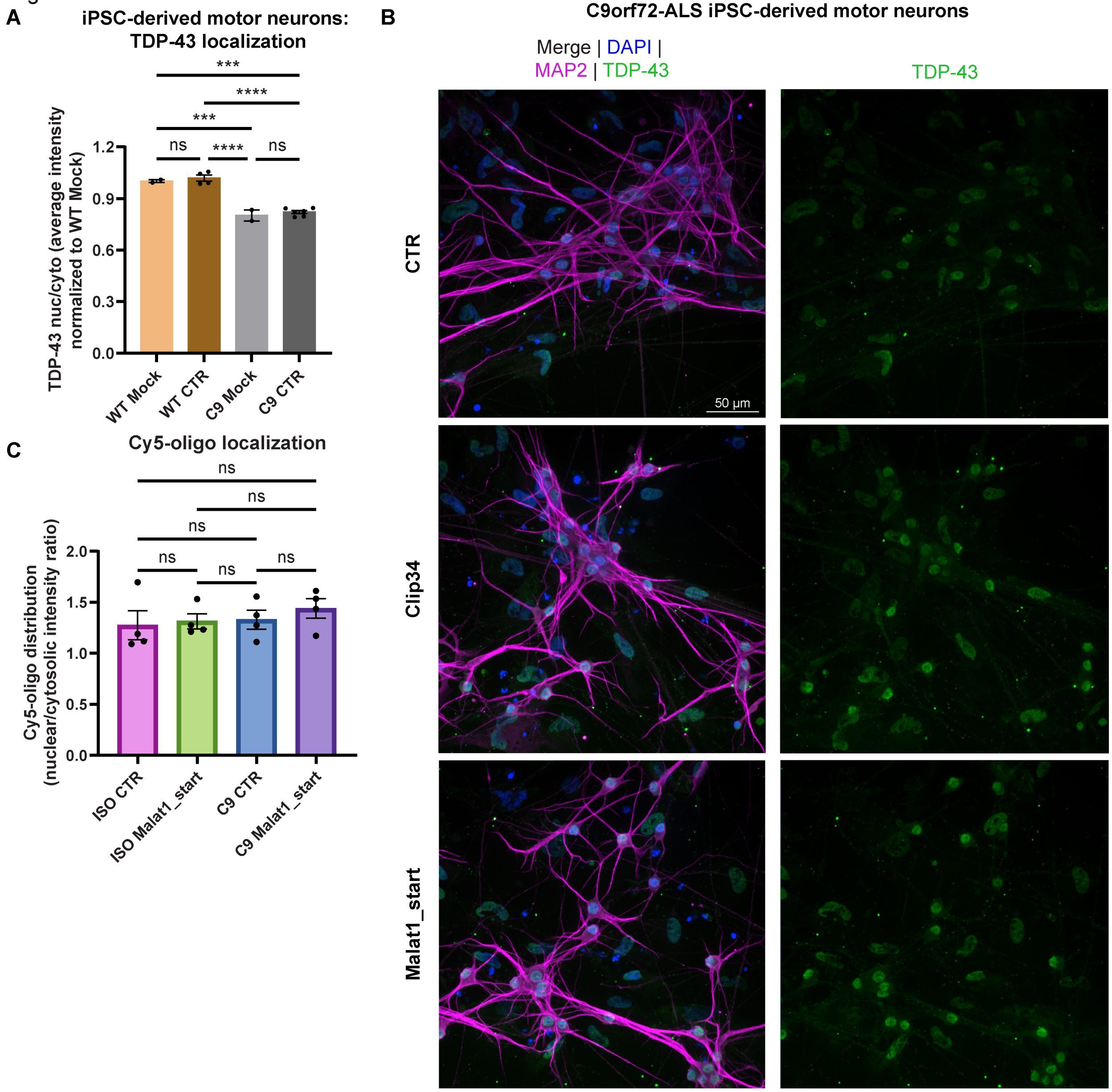

Fig. S22. Clip34 and Malat1_start restore proper TDP-43 localization in C9ORF72 iPSC-derived motor neurons. (A) The average ratio of TDP-43 nuclear to cytoplasmic signal normalized to healthy control iPSC-derived neurons without RNA treatment. C9 CTR condition data are the same as shown in Fig. 5D. Data are mean ± SEM (n=2-6 technical replicates; one-way ANOVA with Tukey's correction; ***$p < 0.001$, ****$p < 0.0001$). **(B)** In addition to images in Fig. 5C, lower magnification representative images of C9orf72-ALS patient iPSC-derived motor neurons treated with the indicated RNAs, stained with DAPI and for TDP-43 and MAP2. Scale bar indicates 50 µm. **(C)** The average ratio of nuclear to cytoplasmic signal of the indicated Cy5-labeled RNA in iPSC-derived motor neurons. Data are mean ± SEM (n=4; one-way ANOVA with Tukey's correction).

Figure S23

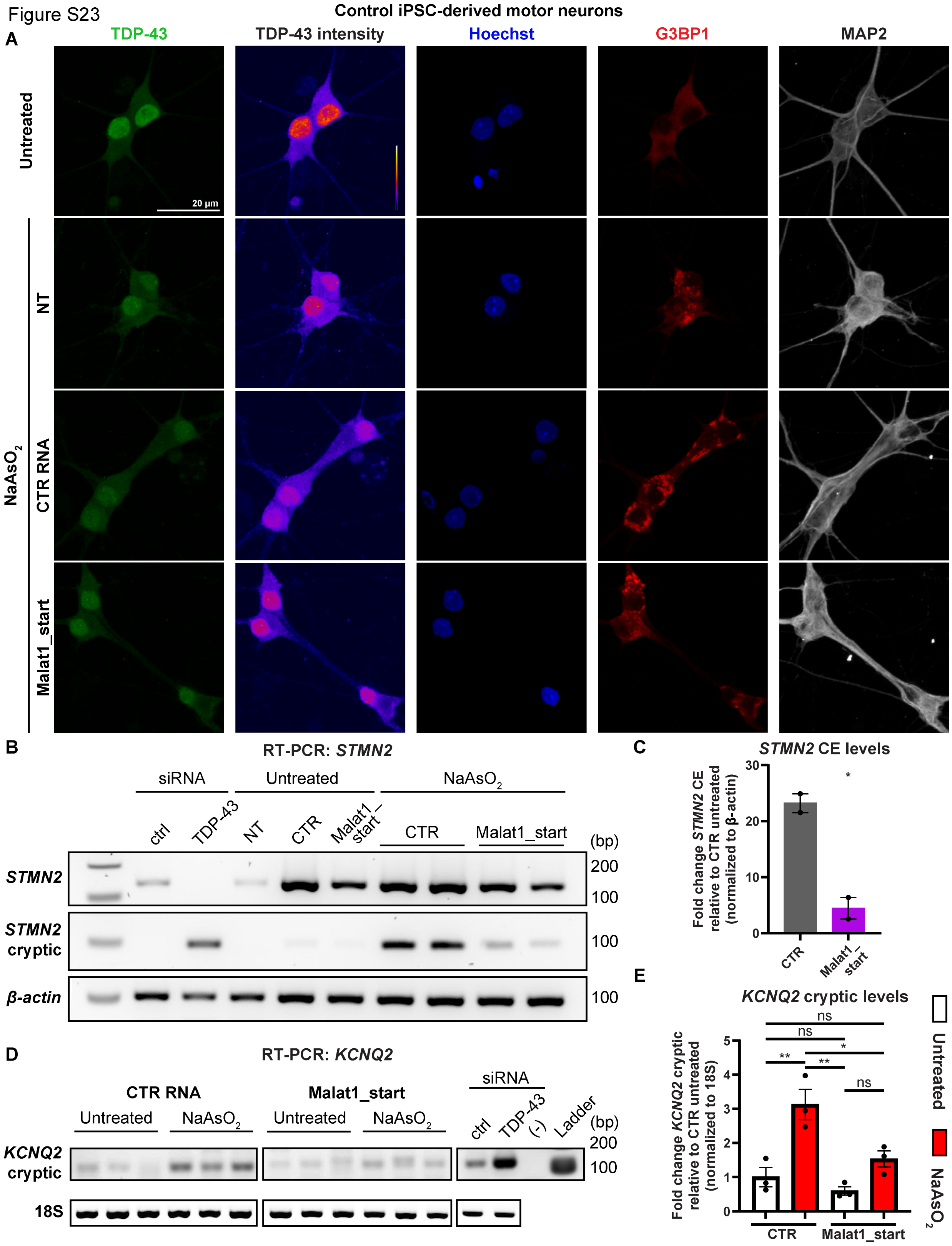

Fig. S23. Malat1_start suppresses cryptic splicing of TDP-43 targets in sodium-arsenite-treated iPSC-derived motor neurons. (A-E) Control iPSC-derived motor neurons were nontreated (NT) or treated with 500 nM CTR RNA or Malat1_start, then were untreated or treated with 250 µM sodium arsenite ($NaAsO_2$) for 2 h, as indicated. **(A)** Representative images of control iPSC-derived motor neurons stained with Hoechst and for TDP-43, G3BP1, and MAP2. Scale bar indicates 20 µm. **(B, C)** RT-PCR gel and corresponding quantification assessing aberrant splicing of TDP-43 target *STMN2*. TDP-43 knockdown by siRNA was confirmed to induce cryptic splicing. Data were normalized to β-actin as a loading control, and fold change was calculated to the untreated CTR RNA condition. Data are mean ± SEM (n=2; unpaired t-test; $^*p < 0.05$). **(D, E)** RT-PCR gel and corresponding quantification assessing aberrant splicing of TDP-43 target *KCNQ2*. TDP-43 knockdown by siRNA was confirmed to induce cryptic splicing. The (-) condition is an RT negative control, containing only cDNA reagent plus water. Data were normalized to 18S as a loading control, and fold change was calculated to the untreated CTR RNA condition. Data are mean ± SEM (n=3; two-way ANOVA with Tukey's correction; $^*p < 0.05$, $^{**}p < 0.01$).

Figure S24

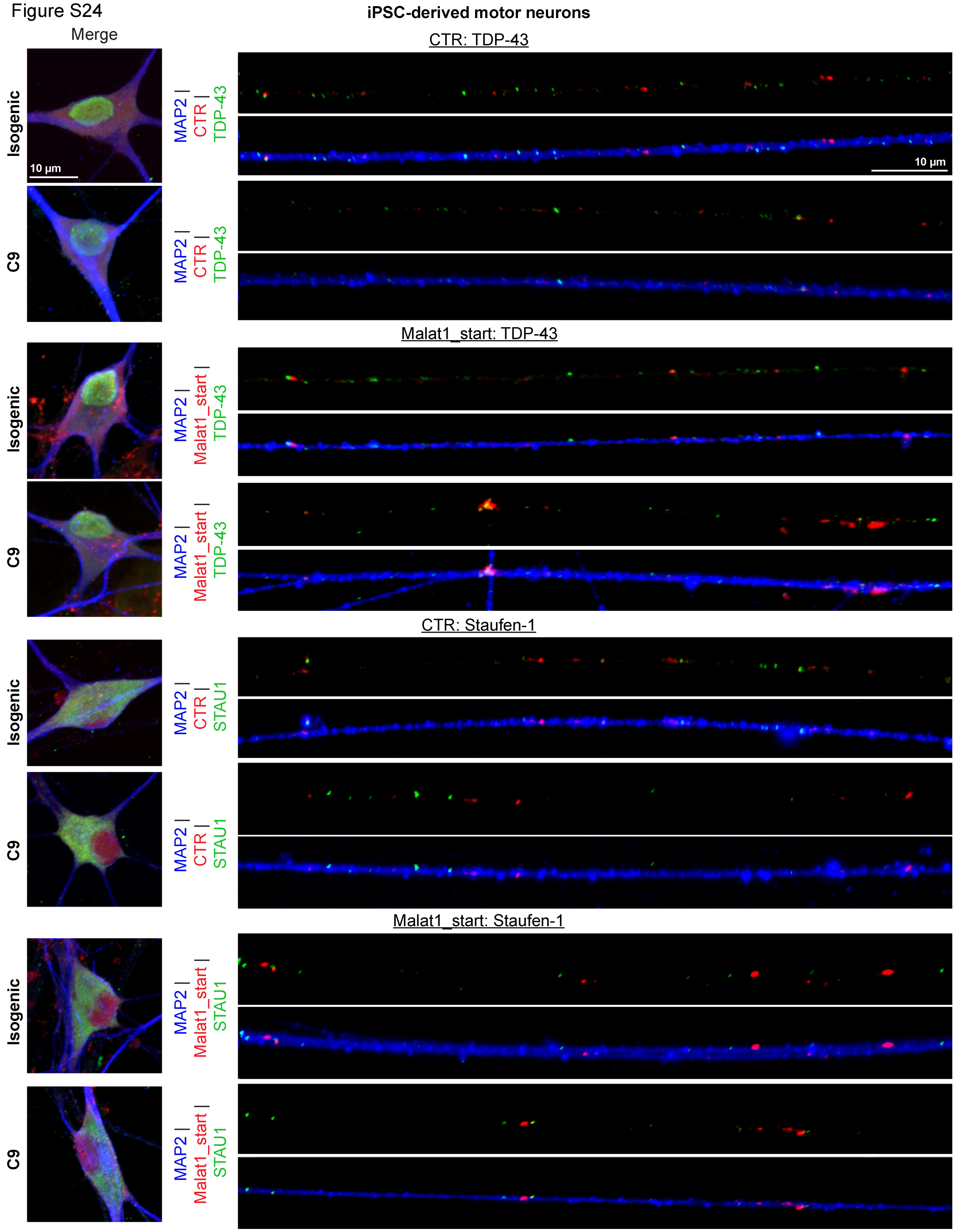

Fig. S24. Malat1_start treatment does not perturb physiological cytoplasmic RNA granules in iPSC-derived motor neurons. Representative images of soma (left) and corresponding neurites (right) for healthy isogenic control or C9orf72-ALS patient iPSC-derived motor neurons treated with Cy5-labeled CTR or Malat1_start RNA as indicated. Neurons were stained for MAP2 and TDP-43 or STAU1, as indicated. Scale bars indicate 10 µm (separate scale bars are shown for soma and neurites).

Figure S25

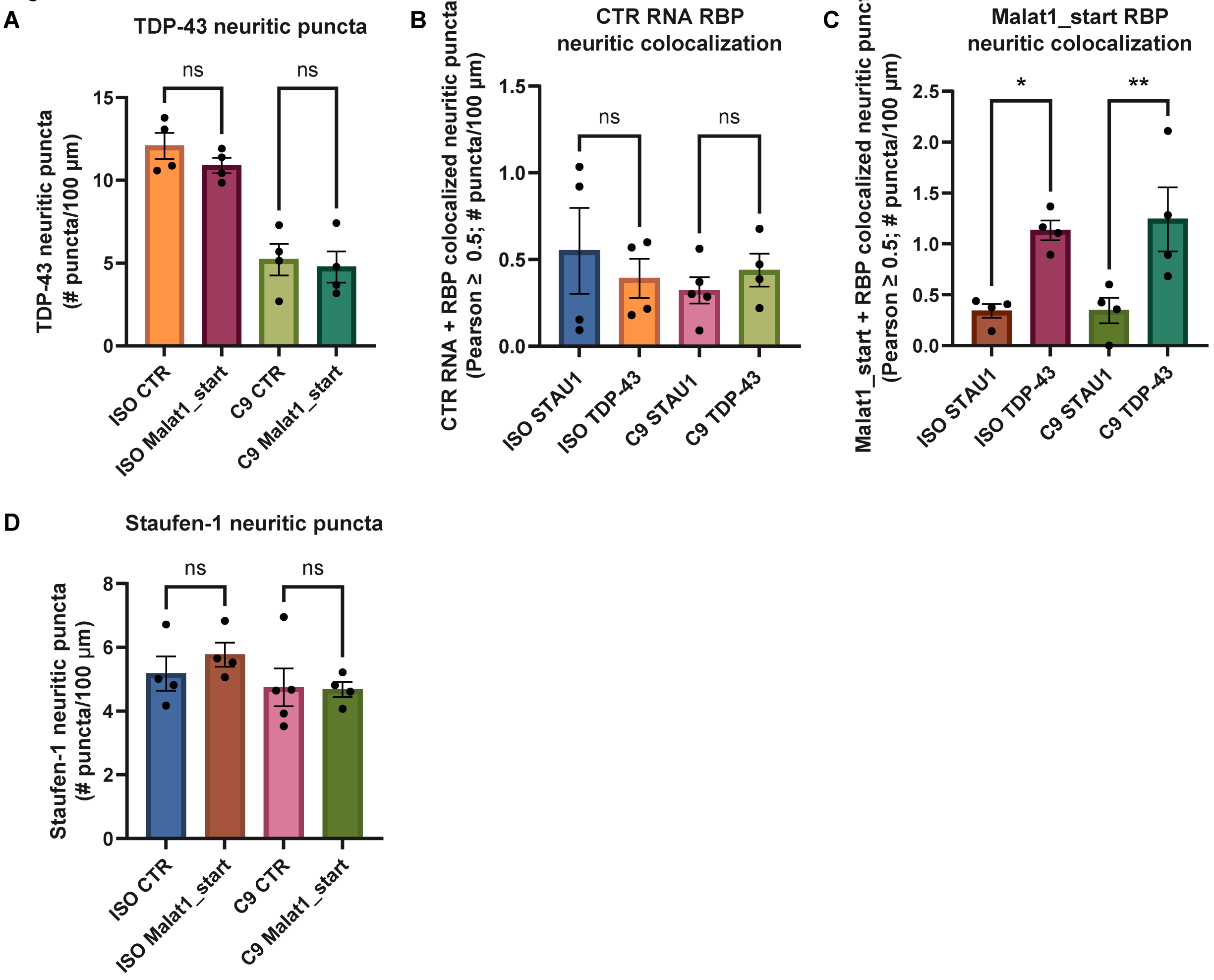

Fig. S25. Quantification of RNA granules in neurites of iPSC-derived motor neurons. (A-D) Quantification corresponding to representative images shown in fig. S24. Puncta are expressed as the number of puncta per 100 µm, and markers were considered to colocalize if Pearson ≥ 0.5. For each technical replicate, the average value was calculated across 20-25 neurites. Data are mean ± SEM (n=4-5 technical replicates; one-way ANOVA with Šidák's correction; $*p < 0.05$, $**p < 0.01$).

Figure S26

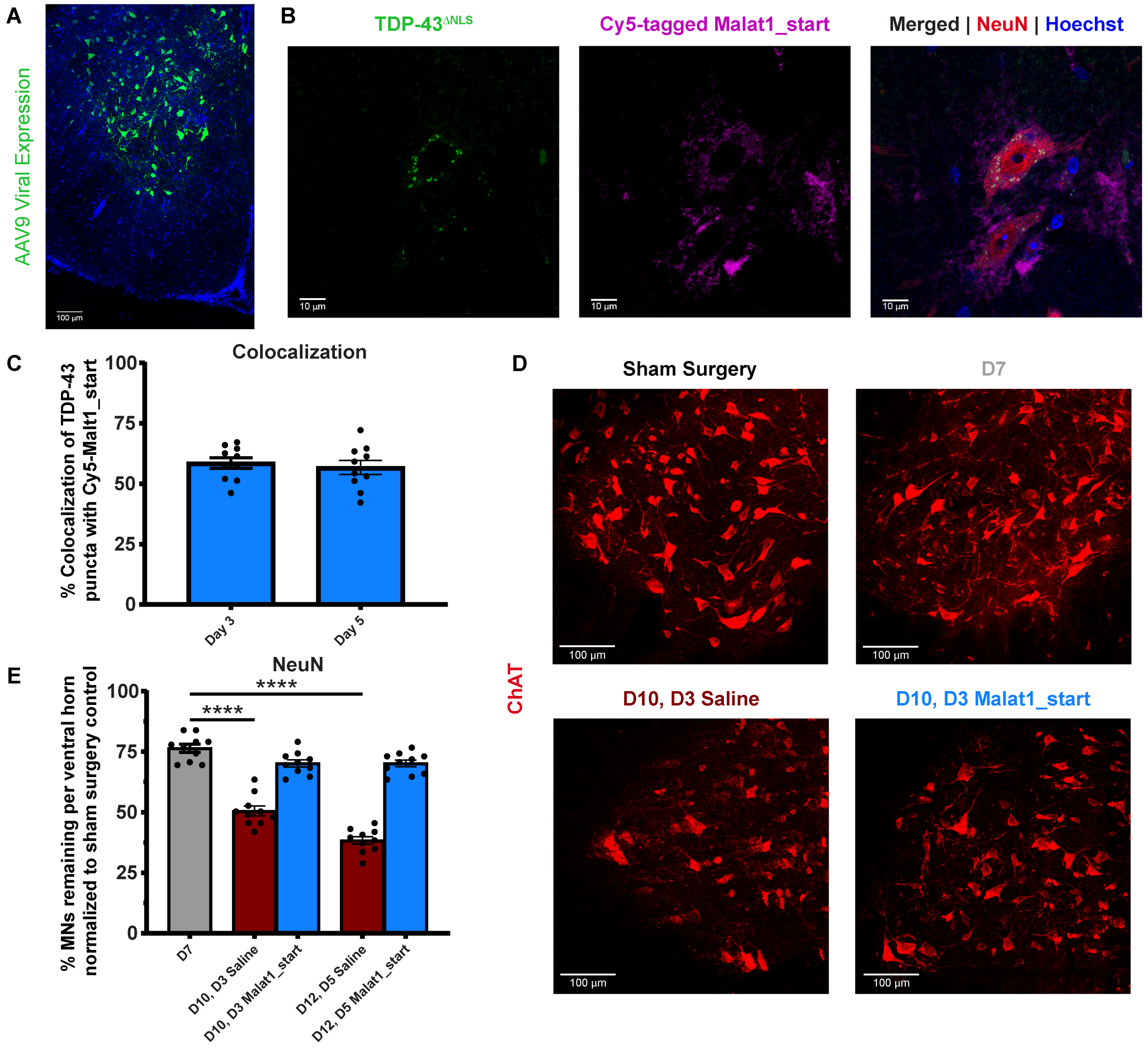

Fig. S26. Malat1_start RNA mitigates neurodegeneration in a mouse model of TDP-43 proteinopathy. (A) Representative transduction profile showing 10x magnification images following six 1x10^{11} GC injections of AAV9-TDP-$43^{\Delta NLS-YFP}$ in p180 female mice. Shown here is baseline 7 days of expression, 30 µm spinal cord slice. Scale bar indicates 100 µm. **(B)** Representative image showing TDP-43 puncta (green), as well as Cy5-tagged Malat1_start RNA (magenta) in NeuN positive (red) motor neurons of the ventral horn of the spinal cord. Shown is a 5-day (12-day expressing) treated animal, demonstrating effective penetration of RNA to this region. 60x magnification; scale bar indicates 10 µm. **(C)** The average percentage of TDP-43-YFP colocalized with Cy5-Malat1_start per cell, based on Mander's coefficient for colocalization. Data shown are mean ± SEM (n=10). **(D)** Representative immunohistochemistry images of ventral horns, stained for choline acetyltransferase (ChAT). 20x magnification z-stack confocal images; scale bar indicates 100 µm. **(E)** Immunostaining quantification for $NeuN^+$ neurons manually counted within the ventral horn region of spinal cord sections. Data are mean ± SEM (n=10 animals per condition; shown: one-way ANOVA with Dunnett's correction comparing to D7 TDP-43: ****$p < 0.0001$; not shown: two-way ANOVA with Šídák's correction: ****$p < 0.0001$ for Malat1_start versus saline at D10 and D12).

Figure S27

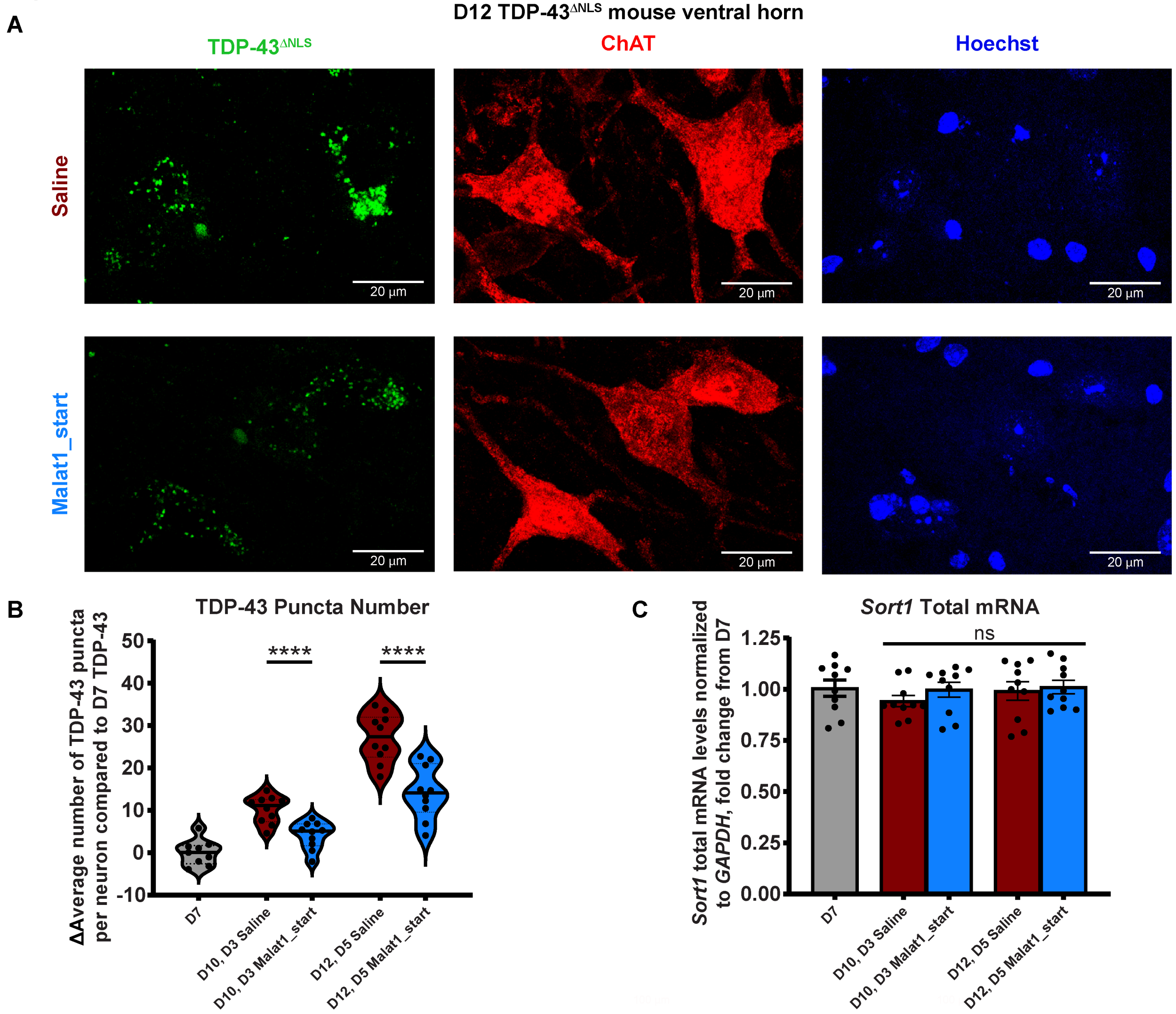

Fig. S27. Malat1_start RNA mitigates TDP-43 aggregation and dysfunction in a mouse model of TDP-43 proteinopathy. (A) Representative 60x magnification immunofluorescent staining images showing single channels corresponding to merged images shown in Fig. 6D; from 5-day (12-day expressing) saline-treated (top) and RNA-treated (bottom) animals. Scale bar indicates 20 µm. **(B)** TDP-43 positive puncta were assessed in ChAT$^+$ motor neurons. Fields at 60x magnification were taken in the ventral horn for each animal (same fields as for Fig. 6E). For each animal, the average number of puncta per neuron was standardized to set the average D7 TDP-43 value to 0. Data shown are mean ± SEM (n=9-10 animals per condition; shown: two-way ANOVA with Šídák's correction: ****p < 0.0001; not shown: one-way ANOVA with Dunnett's correction comparing to D7 TDP-43: ****p < 0.0001 for D10 and D12 saline, and D12 Malat1_start). **(C)** Total *Sort1* mRNA transcripts normalized to *GAPDH*, with fold change calculated from D7 baseline. Data are mean ± SEM (n=10 animals per condition; one-way ANOVA with Dunnett's correction comparing to D7 TDP-43).

Table S1. RNA oligonucleotides utilized in this study.

Name	**RNA sequence and predicted secondary structure (ΔG, kcal/mol)**	**Length (# nt)**	**UG (%)**	**(UG) nt (#)**	**IC_{50} (μM)***	**$K_{D,app}$ (μM)***
Clip34	GAGAGAGCGCGUGCAGAGACUUGGUGGUGCAUAA 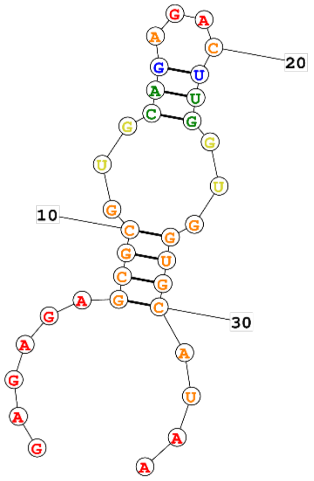 (-6.6)	34	58.82	4	0.50	0.49
$(AC)_{17}$	ACACACACACACACACACACACACACACACACAC n.p.	34	0	0	n.d.	n.d.
AUG12	GUGUGAAUGAAU	12	66.67	3	1.79	n.d.
Clip34_ UG6	GAGAGAGCGCGUGUGUGUGUGUGGUGGUGCAUAA 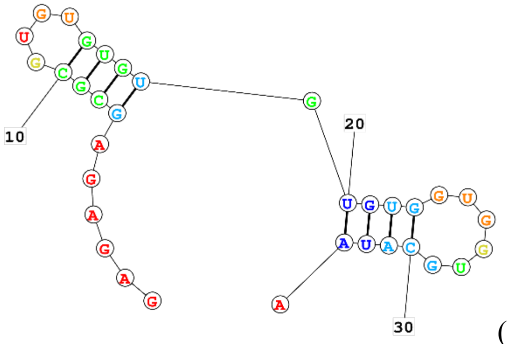 (-5.6)	34	73.53	8	0.45	0.27
Clip34_ UG2_ start	GAGAGAGCGCGUGUGUGGACUUGGUGGUGCAUAA 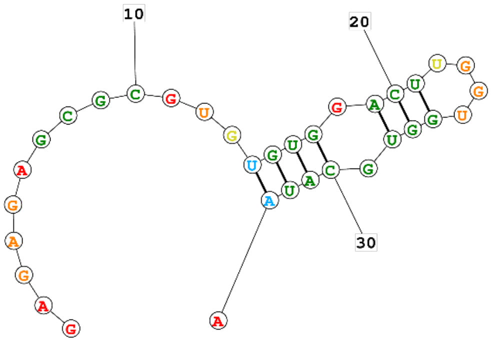 (-5.8)	34	67.65	6	0.38	n.d.
Clip34_ UG2_ middle	GAGAGAGCGCGUGCAUGUGCUUGGUGGUGCAUAA	34	64.71	6	0.33	n.d.

	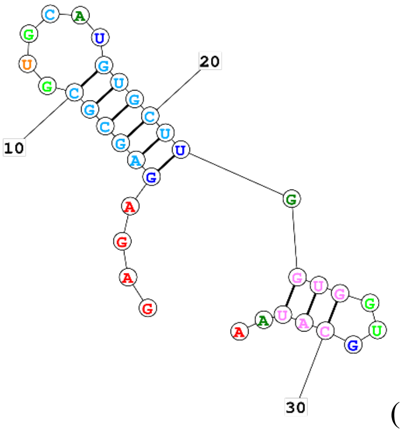 (-7.2)					
Clip34_ UG2_end	GAGAGAGCGCGUGCAGAUGUGUGGUGGUGCAUAA 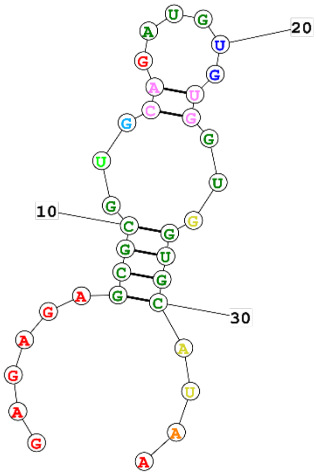 (-6.8)	34	64.71	6	0.48	n.d.
$(UG)_{17}$	UGUGUGUGUGUGUGUGUGUGUGUGUGUGUGUGUG 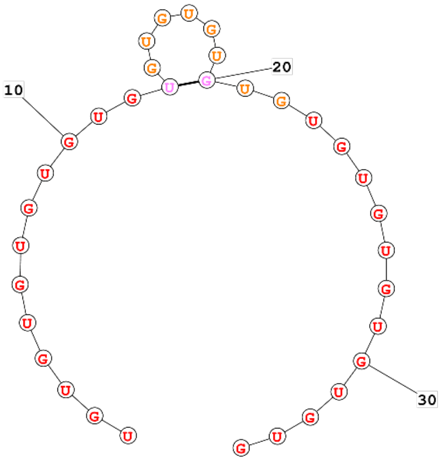 (3.1)	34	100	17	0.20	n.d.
SATIII	UGAAUGGAAUGGAAAGAAUGGAAUCAACACGAGU	34	47.06	4	0.49	0.53

	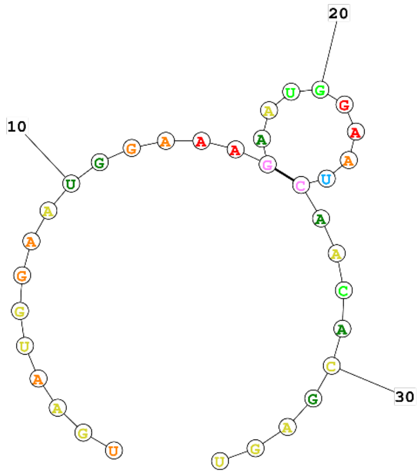 (2.9)					
Malat1_ start	UAUUAGAAUGCAUUGUGAAACGACUGGAGUAUGA 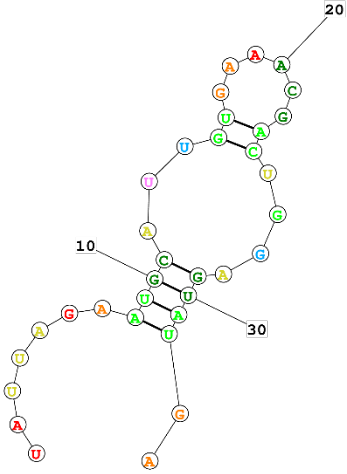 (-1.4)	34	55.88	5	0.36	0.56
CLN6_ middle	UGUGUGUGUCUUGUAUAUGUGUGCGCAGAGUGCA 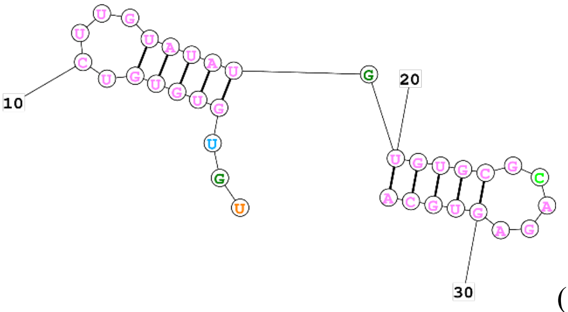 (-4.9)	34	73.53	9	0.42	n.d.
Malat1_ middle	UGUGAAACGACUGGAGUAUGAUUAAAAGUUGUGU	34	61.76	6	0.47	n.d.

	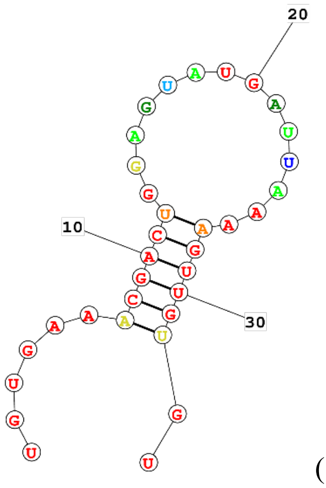 (-4.4)					
Malat1_ end	GAGUAUGAUUAAAGUUGUGUUCCCCAAUGCUUG 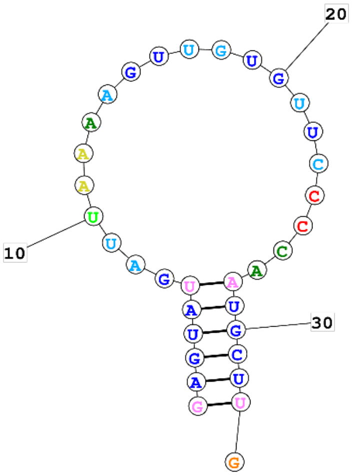 (-2.4)	34	58.82	5	0.57	n.d.
CLN6_ start	UCGUGUGUGUGUGUGUGUGUGUCUUGUAUAUGUG 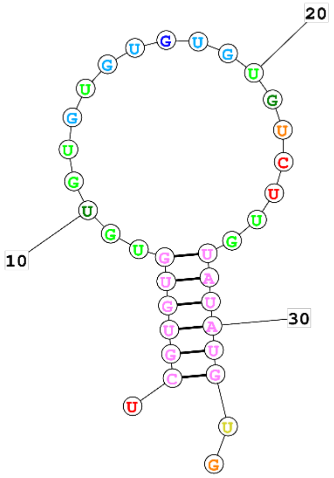 (0.2)	34	88.24	12	0.50	n.d.
CLN6_ end	UAUAUGUGUGCGCAGAGUGCAUCAUUUUCAGACU	34	58.82	4	0.67	n.d.

	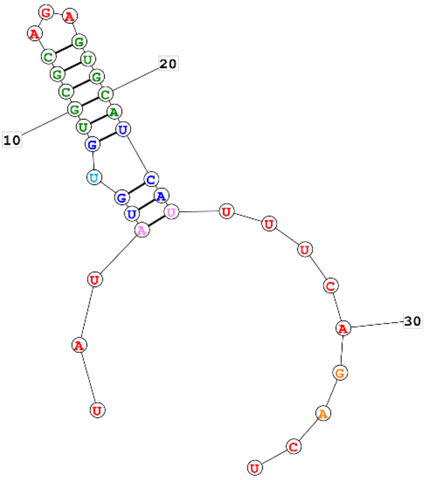 (-6.3)					
LTR-III	GGGAGGCGUGGCCUGGGCGGGACUGGGG 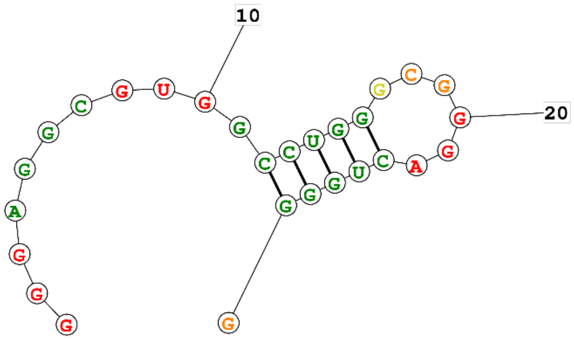 (-5.7)	28	75.00	3	0.55	n.d.
A(GU)$_6$	AGUGUGUGUGUGU n.p.	13	92.31	5	n.d.	n.d.
5’ 6-FAM Clip34	6-FAM - GAGAGAGCGCGUGCAGAGACUUGGUGGUGCAUAA	34	58.82	4	0.50	0.49
5’ 6-FAM Clip34 3’ BHQ1	6-FAM - GAGAGAGCGCGUGCAGAGACUUGGUGGUGC AUAA – BHQ1	34	58.82	4	n.d.	n.d.
5’ 6-FAM Clip34_ UG6	6-FAM - GAGAGAGCGCGUGUGUGUGUGUGGUGGUGCAUAA	34	73.53	8	0.45	0.27
5’ 6-FAM SATIII	6-FAM – UGAAUGGAAUGGAAAGAAUGGAAUCAACACGAGU	34	47.06	4	0.49	0.53
5’ 6-FAM Malat1_ start	6-FAM – UAUUAGAAUGCAUUGUGAAACGACUGGAGUAUGA	34	55.88	5	0.36	0.56
CTR 2’OMe	mUmGmUmAmUmUmUmUmGmAmGmCmUmAmGmUmU mUmGmCmUmGmAmU	24	75.00	4	n.d.	n.d.

	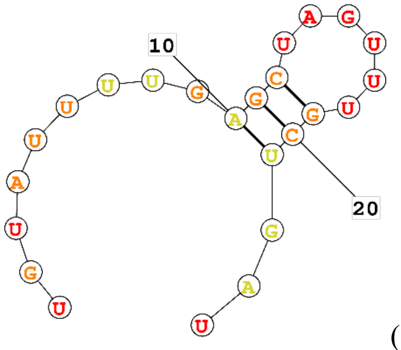 (-2.9)					
Malat1_ start 2’OMe	mUmAmUmUmAmGmAmAmUmGmCmAmUmUmGmUmG mAmAmAmCmGmAmCmUmGmGmAmGmUmAmUmGmA	34	55.88	5	n.d.	n.d.
CLN6_ middle 2’OMe	mUmGmUmGmUmGmUmGmUmCmUmUmGmUmAmUmA mUmGmUmGmUmGmCmGmCmAmGmAmGmUmGmCmA	34	73.53	9	n.d.	n.d.
(UG)$_{17}$ 2’OMe	mUmGmUmGmUmGmUmGmUmGmUmGmUmGmUmGmU mGmUmGmUmGmUmGmUmGmUmGmUmGmUmGmUmG	34	100	17	n.d.	n.d.
Clip34 2’OMe	mG*mA*mG*mA*mGmAmGmCmGmCmGmUmGmCmAmG mAmGmAmCmUmUmGmGmUmGmGmUmG*mC*mA*mU* mA*mA	34	58.82	4	n.d.	n.d.
Malat1_ start PS	mU*mA*mU*mU*mA*mGmAmAmUmGmCmAmUmUmGm UmGmAmAmAmCmGmAmCmUmGmGmAmG*mU*mA*m U*mG*mA	34	55.88	5	n.d.	n.d.
5’ Cy5 Malat1_ start PS	Cy5 –mU*mA*mU*mU*mA*mGmAmAmUmGmCmAmUmU mGmUmGmAmAmAmCmGmAmCmUmGmGmAmG*mU*m A*mU*mG*mA	34	55.88	5	n.d.	n.d.

Table S1. RNA oligonucleotides utilized in this study. The sequences of all RNA oligonucleotides used in this study are provided. ‘m’ indicates the nucleotide has a 2’-O-Methyl modification. ‘*’ indicates a phosphorothioate bond modification. RNA secondary structure predictions were performed utilizing the RNAstructure web server, and reported ΔG values (in kcal/mol) are listed. Nucleotide color corresponds to the confidence in prediction probability; red ≥ 99%; orange ≥ 95%; yellow ≥ 90%; dark green ≥ 80%; light green ≥ 70%; light blue ≥ 60%; dark blue ≥ 50%; pink < 50%. ‘n.p.’ indicates RNAstructure did not generate a predicted secondary structure. Structures were not repeated for the modified versions of unmodified RNAs. The length of each sequence is indicated, as well as two measures of the UG-richness of the sequence. UG (%) was calculated as the percentage of nucleotides in the sequence that are either U or G. UG (#) was calculated as the number of ‘UG’ dinucleotide repeats within the sequence. The rounded IC$_{50}$ and K$_{D,app}$ values for each RNA with WT TDP-43 are listed, referring to data shown in Fig. 3, B and C and E, Fig. 4C, fig. S11A, fig. S16B-E, and fig. S17D-G, J; RNAs for which these values were not determined are indicated as ‘n.d.’ *Both IC$_{50}$ and K$_{D,app}$ values are displayed for reference for both the unmodified and fluorophore-labeled versions of the same RNA sequence, although IC$_{50}$ values were only calculated with the unmodified RNA and K$_{D,app}$ values only with the fluorophore-labeled RNA.

Table S2. HXMS data summary		
Dataset	**TDP-43 (free)**	**TDP-43 + Clip34 RNA (bound)**
HX reaction details	150 mM NaCl, 20 mM HEPES-NaOD, 1 mM DTT in D_2O, pD_{read} 6.0 or 7.0, at 25°C; 80% D_2O	150 mM NaCl, 20 mM HEPES-NaOD, 1 mM DTT in D_2O, pD_{read} 6.0 or 7.0, at 25°C; 80% D_2O
HX time course	pD_{read} 6.0: 1 s, 2 s, 6 s, 18 s, 1 min, 3 min. pD_{read} 7.0: 20 s, 1 min, 3 min, 10 min, 30 min, 1.5 h, 4.5 h, 14.5 h	pD_{read} 6.0: 1 s, 2 s, 6 s, 18 s, 1 min, 3 min. pD_{read} 7.0: 20 s, 1 min, 3 min, 10 min, 30 min, 1.5 h, 4.5 h, 14.5 h
HX control samples	6 Non-deuterated (ND) and 1 fully deuterated (FD; 30°C for 18 h)	6 Non-deuterated (ND) and 1 fully deuterated (FD; 30°C for 18 h)
Back-exchange	Mean: 17%; interquartile range: 11%	Mean: 17%; interquartile range: 11%
Number of peptides	MS/MS identified 246 unique peptides. 137 peptides were found to have good signal and used for HX analysis (a subset of these peptides were analyzed at multiple charge states). Some peptides were not recovered at all timepoints.	MS/MS identified 246 unique peptides. 135 peptides were found to have good signal and used for HX analysis (a subset of these peptides were analyzed at multiple charge states). Some peptides were not recovered at all timepoints.
Sequence coverage	92.7-97.1% (differences in sequence coverage at each timepoint are displayed in figS4A)	87.9-97.1% (differences in sequence coverage at each timepoint are displayed in figS4B)
Average peptide length/redundancy	15.8/5.24	15.9/5.20
Replicates	3 (1 s, 18 s, 20 s, 10 min, 30 min, 1.5 h, 4.5 h, 14.5 h); 5 (2 s, 6 s); 6 (3 min; 3 replicates at each pD); or 7 (1 min; 4 replicates at pD 7.0, 3 at pD 6.0)	3 (1 s, 18 s, 20 s, 10 min, 30 min, 1.5 h, 4.5 h, 14.5 h); 5 (2 s, 6 s); 6 (1 min, 3 min; 3 replicates at each pD)
Repeatability	2.67% (average standard deviation from replicate measurements of percent deuteration of peptides at 10 min timepoint)	1.34% (average standard deviation from replicate measurements of percent deuteration of peptides at 10 min timepoint)
Significant differences in HX	Unpaired t-test with Welch's correction of a difference between free and bound states using p-value < 0.05	Unpaired t-test with Welch's correction of a difference between free and bound states using p-value < 0.05

Table S2. HXMS data summary. Data concerning HXMS experiments (*93*). Only peptides determined to have good signal were used for HX analysis; only these peptides were used to calculate the values for back-exchange, sequence coverage, average peptide length, redundancy, and repeatability. Back-exchange was determined including all charge states for each peptide. Average peptide length counts all amino acids in the peptide, including the two N-terminal amino acids and proline residues. Average peptide length was determined based on only unique peptide sequences; additional charge states for the same peptide sequence were excluded from the calculation. Redundancy was determined based on the total number of peptides used for HX analysis, including all charge states for each peptide. Redundancy was calculated as the total number of peptides multiplied by the average number of deuterons per peptide (peptide length excluding the two N-terminal amino acids and proline residues), divided by the total number of available amides in the protein (excluding the two N-terminal amino acids and proline residues). Repeatability was determined including all charge states for each peptide and was calculated based on percent deuteration values for each peptide (rather than for the absolute number of deuterons).

Table S3. TDP-43^{5FL} HXMS data summary

Dataset	TDP-43^{5FL} (free)	TDP-43^{5FL} + Clip34 RNA (bound)
HX reaction details	150 mM NaCl, 20 mM HEPES-NaOD, 1 mM DTT in D_2O, pD$_{read}$ 6.0 or 7.0, at 25°C; 80% D_2O	150 mM NaCl, 20 mM HEPES-NaOD, 1 mM DTT in D_2O, pD$_{read}$ 6.0 or 7.0, at 25°C; 80% D_2O
HX time course	pD$_{read}$ 6.0: 2 s; pD$_{read}$ 7.0: 4.5 h	pD$_{read}$ 6.0: 2 s; pD$_{read}$ 7.0: 4.5 h
HX control samples	3 Non-deuterated (ND) and 1 fully deuterated (FD; 30°C for 18 h)	3 Non-deuterated (ND) and 1 fully deuterated (FD; 30°C for 18 h)
Back-exchange	Mean: 22%; interquartile range: 11%	Mean: 22%; interquartile range: 11%
Number of peptides	MS/MS identified 197 unique peptides. 153 peptides were found to have good signal and used for HX analysis (a subset of these peptides were analyzed at multiple charge states). Some peptides were not recovered at all timepoints.	MS/MS identified 197 unique peptides. 153 peptides were found to have good signal and used for HX analysis (a subset of these peptides were analyzed at multiple charge states). Some peptides were not recovered at all timepoints.
Sequence coverage	96.1% (differences in sequence coverage at each timepoint are displayed in figS8A)	96.1% (differences in sequence coverage at each timepoint are displayed in figS8B)
Average peptide length/redundancy	16.3/7.71	16.3/7.74
Replicates	3 (2 s) or 4 (4.5 h)	3 (4.5 h) or 4 (2 s)
Repeatability	2.82% (average standard deviation from replicate measurements of percent deuteration of peptides at 4.5 h timepoint)	1.93% (average standard deviation from replicate measurements of percent deuteration of peptides at 4.5 h timepoint)
Significant differences in HX	Unpaired t-test with Welch's correction of a difference between free and bound states using p-value < 0.05	Unpaired t-test with Welch's correction of a difference between free and bound states using p-value < 0.05

Table S3. TDP-43^{5FL} HXMS data summary. Data concerning HXMS experiments performed with TDP-43^{5FL}-MBP-His is provided as previously suggested (*93*). Only peptides determined to have good signal were used for HX analysis; only these peptides were used to calculate the values for back-exchange, sequence coverage, average peptide length, redundancy, and repeatability. Back-exchange was determined including all charge states for each peptide. Average peptide length counts all amino acids in the peptide, including the two N-terminal amino acids and proline residues. Average peptide length was determined based on only unique peptide sequences; additional charge states for the same peptide sequence were excluded from the calculation. Redundancy was determined based on the total number of peptides used for HX analysis, including all charge states for each peptide. Redundancy was calculated as the total number of peptides multiplied by the average number of deuterons per peptide (peptide length excluding the two N-terminal amino acids and proline residues), divided by the total number of available amides in the protein (excluding the two N-terminal amino acids and proline residues). Repeatability was determined including all charge states for each peptide, and was calculated based on percent deuteration values for each peptide (rather than for the absolute number of deuterons).

Table S4. Simulations conducted in this study

Construct	**Condition**	**Duration**
ΔNTD	TDP-43 lacking the NTD (residues 102-414) without RNA	2.5 μs * 3 replica
ΔNTD^{RNA}	TDP-43 lacking the NTD (residues 102-414) bound to AUG12 RNA (5′-GUGUGAAUGAAU-3′)	2.5 μs * 3 replica
ΔNTD 5FL^{RNA}	TDP-43 lacking the NTD (residues 102-414) with F147/149/194/229/231L mutations and AUG12 RNA (5′-GUGUGAAUGAAU-3′)	2.5 μs * 3 replica
FL	TDP-43 full-length	2.5 μs * 3 replica
FL^{RNA}	TDP-43 full-length bound to AUG12 RNA (5′-GUGUGAAUGAAU-3′)	2.5 μs * 3 replica
FL 5FL^{RNA}	TDP-43 full-length with F147/149/194/229/231L mutations and AUG12 RNA (5′-GUGUGAAUGAAU-3′)	2.5 μs * 3 replica

Table S4. Simulations conducted in this study. Details of the conditions and simulation durations for each indicated construct.

References and Notes

1. A. F. Harrison, J. Shorter, RNA-binding proteins with prion-like domains in health and disease. *Biochem. J.* **474**, 1417–1438 (2017). doi:10.1042/BCJ20160499 Medline
2. B. Portz, B. L. Lee, J. Shorter, FUS and TDP-43 Phases in Health and Disease. *Trends Biochem. Sci.* **46**, 550–563 (2021). doi:10.1016/j.tibs.2020.12.005 Medline
3. A. Meneses, S. Koga, J. O'Leary, D. W. Dickson, G. Bu, N. Zhao, TDP-43 Pathology in Alzheimer's Disease. *Mol. Neurodegener.* **16**, 84 (2021). doi:10.1186/s13024-021-00503-x Medline
4. P. T. Nelson, D. W. Dickson, J. Q. Trojanowski, C. R. Jack, P. A. Boyle, K. Arfanakis, R. Rademakers, I. Alafuzoff, J. Attems, C. Brayne, I. T. S. Coyle-Gilchrist, H. C. Chui, D. W. Fardo, M. E. Flanagan, G. Halliday, S. R. K. Hokkanen, S. Hunter, G. A. Jicha, Y. Katsumata, C. H. Kawas, C. D. Keene, G. G. Kovacs, W. A. Kukull, A. I. Levey, N. Makkinejad, T. J. Montine, S. Murayama, M. E. Murray, S. Nag, R. A. Rissman, W. W. Seeley, R. A. Sperling, C. L. White 3rd, L. Yu, J. A. Schneider, Limbic-predominant age-related TDP-43 encephalopathy (LATE): Consensus working group report. *Brain* **142**, 1503–1527 (2019). doi:10.1093/brain/awz099 Medline
5. R. Nicks, N. F. Clement, V. E. Alvarez, Y. Tripodis, Z. H. Baucom, B. R. Huber, J. Mez, M. L. Alosco, N. Aytan, J. D. Cherry, K. A. Cormier, C. Kubilius, R. Mathias, S. E. Svirsky, M. J. Pothast, A. M. Hildebrandt, J. Chung, X. Han, J. F. Crary, A. C. McKee, M. P. Frosch, T. D. Stein, Repetitive head impacts and chronic traumatic encephalopathy are associated with TDP-43 inclusions and hippocampal sclerosis. *Acta Neuropathol.* **145**, 395–408 (2023). doi:10.1007/s00401-023-02539-3 Medline
6. D. Arseni, R. Chen, A. G. Murzin, S. Y. Peak-Chew, H. J. Garringer, K. L. Newell, F. Kametani, A. C. Robinson, R. Vidal, B. Ghetti, M. Hasegawa, B. Ryskeldi-Falcon, TDP-43 forms amyloid filaments with a distinct fold in type A FTLD-TDP. *Nature* **620**, 898–903 (2023). doi:10.1038/s41586-023-06405-w Medline
7. D. Arseni, M. Hasegawa, A. G. Murzin, F. Kametani, M. Arai, M. Yoshida, B. Ryskeldi-Falcon, Structure of pathological TDP-43 filaments from ALS with FTLD. *Nature* **601**, 139–143 (2022). doi:10.1038/s41586-021-04199-3 Medline
8. M. Neumann, D. M. Sampathu, L. K. Kwong, A. C. Truax, M. C. Micsenyi, T. T. Chou, J. Bruce, T. Schuck, M. Grossman, C. M. Clark, L. F. McCluskey, B. L. Miller, E. Masliah, I. R. Mackenzie, H. Feldman, W. Feiden, H. A. Kretzschmar, J. Q. Trojanowski, V. M.-Y. Lee, Ubiquitinated TDP-43 in frontotemporal lobar degeneration and amyotrophic lateral sclerosis. *Science* **314**, 130–133 (2006). doi:10.1126/science.1134108 Medline
9. P. R. Mehta, A. L. Brown, M. E. Ward, P. Fratta, The era of cryptic exons: Implications for ALS-FTD. *Mol. Neurodegener.* **18**, 16 (2023). doi:10.1186/s13024-023-00608-5 Medline
10. S. Yang, Z. Lei, J. U. Guo, TDP-43 loss brings RNA to a twist ending. *Nat. Neurosci.* **28**, 2176–2177 (2025). doi:10.1038/s41593-025-02065-3 Medline
11. C. M. Fare, J. Shorter, (Dis)Solving the problem of aberrant protein states. *Dis. Model. Mech.* **14**, dmm048983 (2021). doi:10.1242/dmm.048983 Medline
12. F. Gasset-Rosa, S. Lu, H. Yu, C. Chen, Z. Melamed, L. Guo, J. Shorter, S. Da Cruz, D. W. Cleveland, Cytoplasmic TDP-43 De-mixing Independent of Stress Granules Drives

Inhibition of Nuclear Import, Loss of Nuclear TDP-43, and Cell Death. *Neuron* **102**, 339–357.e7 (2019). doi:10.1016/j.neuron.2019.02.038 Medline

13. L. Guo, J. R. Mann, J. C. Mauna, K. E. Copley, H. Wang, J. D. Rubien, C. A. Bergmann, J. L. Carey, J. Merjane, M. Ngo, J. Xu, H. M. Odeh, J. Lin, B. L. Lee, L. Ganser, E. Robinson, K. M. Kim, A. C. Murthy, T. Paul, B. Portz, A. M. Gleixner, Z. Diaz, A. Smirnov, G. Padilla, E. Lavorando, C. Espy, Y. Shang, E. J. Huang, A. Chesi, N. L. Fawzi, S. Myong, C. J. Donnelly, J. Shorter, Defining RNA oligonucleotides that reverse deleterious phase transitions of RNA-binding proteins with prion-like domains. *Mol. Cell* **86**, 114–134.e10 (2026). doi:10.1016/j.molcel.2025.12.009 Medline
14. J. R. Mann, A. M. Gleixner, J. C. Mauna, E. Gomes, M. R. DeChellis-Marks, P. G. Needham, K. E. Copley, B. Hurtle, B. Portz, N. J. Pyles, L. Guo, C. B. Calder, Z. P. Wills, U. B. Pandey, J. K. Kofler, J. L. Brodsky, A. Thathiah, J. Shorter, C. J. Donnelly, RNA Binding Antagonizes Neurotoxic Phase Transitions of TDP-43. *Neuron* **102**, 321–338.e8 (2019). doi:10.1016/j.neuron.2019.01.048 Medline
15. L. McGurk, E. Gomes, L. Guo, J. Mojsilovic-Petrovic, V. Tran, R. G. Kalb, J. Shorter, N. M. Bonini, Poly(ADP-Ribose) Prevents Pathological Phase Separation of TDP-43 by Promoting Liquid Demixing and Stress Granule Localization. *Mol. Cell* **71**, 703–717.e9 (2018). doi:10.1016/j.molcel.2018.07.002 Medline
16. X. Yan, D. Kuster, P. Mohanty, J. Nijssen, K. Pombo-García, J. Garcia Morato, A. Rizuan, T. M. Franzmann, A. Sergeeva, A. M. Ly, F. Liu, P. M. Passos, L. George, S.-H. Wang, J. Shenoy, H. L. Danielson, B. Ozguney, A. Honigmann, Y. M. Ayala, N. L. Fawzi, D. W. Dickson, W. Rossoll, J. Mittal, S. Alberti, A. A. Hyman, Intra-condensate demixing of TDP-43 inside stress granules generates pathological aggregates. *Cell* **188**, 4123–4140.e18 (2025). doi:10.1016/j.cell.2025.04.039 Medline
17. P. J. Lukavsky, D. Daujotyte, J. R. Tollervey, J. Ule, C. Stuani, E. Buratti, F. E. Baralle, F. F. Damberger, F. H.-T. Allain, Molecular basis of UG-rich RNA recognition by the human splicing factor TDP-43. *Nat. Struct. Mol. Biol.* **20**, 1443–1449 (2013). doi:10.1038/nsmb.2698 Medline
18. A. E. Conicella, G. L. Dignon, G. H. Zerze, H. B. Schmidt, A. M. D’Ordine, Y. C. Kim, R. Rohatgi, Y. M. Ayala, J. Mittal, N. L. Fawzi, TDP-43 α-helical structure tunes liquid-liquid phase separation and function. *Proc. Natl. Acad. Sci. U.S.A.* **117**, 5883–5894 (2020). doi:10.1073/pnas.1912055117 Medline
19. A. E. Conicella, G. H. Zerze, J. Mittal, N. L. Fawzi, ALS Mutations Disrupt Phase Separation Mediated by α-Helical Structure in the TDP-43 Low-Complexity C-Terminal Domain. *Structure* **24**, 1537–1549 (2016). doi:10.1016/j.str.2016.07.007 Medline
20. B. S. Johnson, D. Snead, J. J. Lee, J. M. McCaffery, J. Shorter, A. D. Gitler, TDP-43 is intrinsically aggregation-prone, and amyotrophic lateral sclerosis-linked mutations accelerate aggregation and increase toxicity. *J. Biol. Chem.* **284**, 20329–20339 (2009). doi:10.1074/jbc.M109.010264 Medline
21. E. Buratti, TDP-43 post-translational modifications in health and disease. *Expert Opin. Ther. Targets* **22**, 279–293 (2018). doi:10.1080/14728222.2018.1439923 Medline

22. T. J. Cohen, A. W. Hwang, C. R. Restrepo, C.-X. Yuan, J. Q. Trojanowski, V. M. Y. Lee, An acetylation switch controls TDP-43 function and aggregation propensity. *Nat. Commun.* **6**, 5845 (2015). doi:10.1038/ncomms6845 Medline

23. S. Maharana, J. Wang, D. K. Papadopoulos, D. Richter, A. Pozniakovsky, I. Poser, M. Bickle, S. Rizk, J. Guillén-Boixet, T. M. Franzmann, M. Jahnel, L. Marrone, Y.-T. Chang, J. Sterneckert, P. Tomancak, A. A. Hyman, S. Alberti, RNA buffers the phase separation behavior of prion-like RNA binding proteins. *Science* **360**, 918–921 (2018). doi:10.1126/science.aar7366 Medline

24. C. J. Sumner, T. M. Miller, The expanding application of antisense oligonucleotides to neurodegenerative diseases. *J. Clin. Invest.* **134**, e186116 (2024). doi:10.1172/JCI186116 Medline

25. C. N. Cook, Y. Wu, H. M. Odeh, T. F. Gendron, K. Jansen-West, G. Del Rosso, M. Yue, P. Jiang, E. Gomes, J. Tong, L. M. Daughrity, N. M. Avendano, M. Castanedes-Casey, W. Shao, B. Oskarsson, G. S. Tomassy, A. McCampbell, F. Rigo, D. W. Dickson, J. Shorter, Y.-J. Zhang, L. Petrucelli, *C9orf72* poly(GR) aggregation induces TDP-43 proteinopathy. *Sci. Transl. Med.* **12**, eabb3774 (2020). doi:10.1126/scitranslmed.abb3774 Medline

26. E. Buratti, F. E. Baralle, Characterization and functional implications of the RNA binding properties of nuclear factor TDP-43, a novel splicing regulator of *CFTR* exon 9. *J. Biol. Chem.* **276**, 36337–36343 (2001). doi:10.1074/jbc.M104236200 Medline

27. X. Zhang, T. Das, T. F. Chao, V. Trinh, R. P. Carmen-Orozco, J. P. Ling, P. Kalab, L. R. Hayes, Multivalent GU-rich oligonucleotides sequester TDP-43 in the nucleus by inducing high molecular weight RNP complexes. *iScience* **27**, 110109 (2024). doi:10.1016/j.isci.2024.110109 Medline

28. N. Mollasalehi, L. Francois-Moutal, D. D. Scott, J. A. Tello, H. Williams, B. Mahoney, J. M. Carlson, Y. Dong, X. Li, V. G. Miranda, V. Gokhale, W. Wang, S. J. Barmada, M. Khanna, An Allosteric Modulator of RNA Binding Targeting the N-Terminal Domain of TDP-43 Yields Neuroprotective Properties. *ACS Chem. Biol.* **15**, 2854–2859 (2020). doi:10.1021/acschembio.0c00494 Medline

29. M. Hallegger, A. M. Chakrabarti, F. C. Y. Lee, B. L. Lee, A. G. Amalietti, H. M. Odeh, K. E. Copley, J. D. Rubien, B. Portz, K. Kuret, I. Huppertz, F. Rau, R. Patani, N. L. Fawzi, J. Shorter, N. M. Luscombe, J. Ule, TDP-43 condensation properties specify its RNA-binding and regulatory repertoire. *Cell* **184**, 4680–4696.e22 (2021). doi:10.1016/j.cell.2021.07.018 Medline

30. A. Rizuan, J. Shenoy, P. Mohanty, P. M. Dos Passos, J. F. Mercado Ortiz, L. Bai, R. Viswanathan, J. Zaborowksy, S.-H. Wang, V. Johnson, L. D. Mamede, A. R. Titus, Y. M. Ayala, R. Ghirlando, J. Mittal, N. L. Fawzi, Structural details of helix-mediated multimerization of the conserved region of TDP-43 C-terminal domain. *Nat. Commun.* **16**, 10528 (2025). doi:10.1038/s41467-025-65546-w Medline

31. M. Polymenidou, C. Lagier-Tourenne, K. R. Hutt, S. C. Huelga, J. Moran, T. Y. Liang, S.-C. Ling, E. Sun, E. Wancewicz, C. Mazur, H. Kordasiewicz, Y. Sedaghat, J. P. Donohue, L. Shiue, C. F. Bennett, G. W. Yeo, D. W. Cleveland, Long pre-mRNA depletion and RNA missplicing contribute to neuronal vulnerability from loss of TDP-43. *Nat. Neurosci.* **14**, 459–468 (2011). doi:10.1038/nn.2779 Medline

32. J. R. Tollervey, T. Curk, B. Rogelj, M. Briese, M. Cereda, M. Kayikci, J. König, T. Hortobágyi, A. L. Nishimura, V. Župunski, R. Patani, S. Chandran, G. Rot, B. Zupan, C. E. Shaw, J. Ule, Characterizing the RNA targets and position-dependent splicing regulation by TDP-43. *Nat. Neurosci.* **14**, 452–458 (2011). doi:10.1038/nn.2778 Medline

33. J. S. Reuter, D. H. Mathews, RNAstructure: Software for RNA secondary structure prediction and analysis. *BMC Bioinformatics* **11**, 129 (2010). doi:10.1186/1471-2105-11-129 Medline

34. S. W. Englander, Hydrogen exchange and mass spectrometry: A historical perspective. *J. Am. Soc. Mass Spectrom.* **17**, 1481–1489 (2006). doi:10.1016/j.jasms.2006.06.006 Medline

35. J. Jumper, R. Evans, A. Pritzel, T. Green, M. Figurnov, O. Ronneberger, K. Tunyasuvunakool, R. Bates, A. Žídek, A. Potapenko, A. Bridgland, C. Meyer, S. A. A. Kohl, A. J. Ballard, A. Cowie, B. Romera-Paredes, S. Nikolov, R. Jain, J. Adler, T. Back, S. Petersen, D. Reiman, E. Clancy, M. Zielinski, M. Steinegger, M. Pacholska, T. Berghammer, S. Bodenstein, D. Silver, O. Vinyals, A. W. Senior, K. Kavukcuoglu, P. Kohli, D. Hassabis, Highly accurate protein structure prediction with AlphaFold. *Nature* **596**, 583–589 (2021). doi:10.1038/s41586-021-03819-2 Medline

36. M. Aikio, H. M. Odeh, H. J. Wobst, B. L. Lee, Ú. Chan, J. C. Mauna, K. L. Mack, B. Class, T. A. Ollerhead, A. F. Ford, E. M. Barbieri, R. R. Cupo, L. E. Drake, J. L. Smalley, Y.-T. Lin, S. Lam, R. Thomas, N. Castello, A. Baral, J. N. Beyer, M. A. Najar, J. Dunlop, A. D. Gitler, A. Javaherian, J. A. Kaye, G. M. Burslem, D. G. Brown, C. J. Donnelly, S. Finkbeiner, S. J. Moss, N. J. Brandon, J. Shorter, Opposing roles of p38α-mediated phosphorylation and PRMT1-mediated arginine methylation in driving TDP-43 proteinopathy. *Cell Rep.* **44**, 115205 (2025). doi:10.1016/j.celrep.2024.115205 Medline

37. S. Agrawal, M. Jain, W. Z. Yang, H. S. Yuan, Frontotemporal dementia-linked P112H mutation of TDP-43 induces protein structural change and impairs its RNA binding function. *Protein Sci.* **30**, 350–365 (2021). doi:10.1002/pro.3990 Medline

38. F. Moreno, G. D. Rabinovici, A. Karydas, Z. Miller, S. C. Hsu, A. Legati, J. Fong, D. Schonhaut, H. Esselmann, C. Watson, M. L. Stephens, J. Kramer, J. Wiltfang, W. W. Seeley, B. L. Miller, G. Coppola, L. T. Grinberg, A novel mutation P112H in the *TARDBP* gene associated with frontotemporal lobar degeneration without motor neuron disease and abundant neuritic amyloid plaques. *Acta Neuropathol. Commun.* **3**, 19 (2015). doi:10.1186/s40478-015-0190-6 Medline

39. H. J. Chen, S. D. Topp, H. S. Hui, E. Zacco, M. Katarya, C. McLoughlin, A. King, B. N. Smith, C. Troakes, A. Pastore, C. E. Shaw, RRM adjacent *TARDBP* mutations disrupt RNA binding and enhance TDP-43 proteinopathy. *Brain* **142**, 3753–3770 (2019). doi:10.1093/brain/awz313 Medline

40. M. Neumann, L. K. Kwong, E. B. Lee, E. Kremmer, A. Flatley, Y. Xu, M. S. Forman, D. Troost, H. A. Kretzschmar, J. Q. Trojanowski, V. M.-Y. Lee, Phosphorylation of S409/410 of TDP-43 is a consistent feature in all sporadic and familial forms of TDP-43 proteinopathies. *Acta Neuropathol.* **117**, 137–149 (2009). doi:10.1007/s00401-008-0477-9 Medline

41. H. Yu, S. Lu, K. Gasior, D. Singh, S. Vazquez-Sanchez, O. Tapia, D. Toprani, M. S. Beccari, J. R. Yates 3rd, S. Da Cruz, J. M. Newby, M. Lafarga, A. S. Gladfelter, E. Villa, D. W.

Cleveland, HSP70 chaperones RNA-free TDP-43 into anisotropic intranuclear liquid spherical shells. *Science* **371**, eabb4309 (2021). doi:10.1126/science.abb4309 Medline

42. P. Wang, C. M. Wander, C. X. Yuan, M. S. Bereman, T. J. Cohen, Acetylation-induced TDP-43 pathology is suppressed by an HSF1-dependent chaperone program. *Nat. Commun.* **8**, 82 (2017). doi:10.1038/s41467-017-00088-4 Medline

43. J. C. Necarsulmer, J. M. Simon, B. A. Evangelista, Y. Chen, X. Tian, S. Nafees, A. B. Marquez, H. Jiang, P. Wang, D. Ajit, V. D. Nikolova, K. M. Harper, J. A. Ezzell, F.-C. Lin, A. S. Beltran, S. S. Moy, T. J. Cohen, RNA-binding deficient TDP-43 drives cognitive decline in a mouse model of TDP-43 proteinopathy. *eLife* **12**, RP85921 (2023). doi:10.7554/eLife.85921.3 Medline

44. A. Bhardwaj, M. P. Myers, E. Buratti, F. E. Baralle, Characterizing TDP-43 interaction with its RNA targets. *Nucleic Acids Res.* **41**, 5062–5074 (2013). doi:10.1093/nar/gkt189 Medline

45. C. Y. Chung, A. Berson, J. R. Kennerdell, A. Sartoris, T. Unger, S. Porta, H.-J. Kim, E. R. Smith, A. Shilatifard, V. Van Deerlin, V. M.-Y. Lee, A. Chen-Plotkin, N. M. Bonini, Aberrant activation of non-coding RNA targets of transcriptional elongation complexes contributes to TDP-43 toxicity. *Nat. Commun.* **9**, 4406 (2018). doi:10.1038/s41467-018-06543-0 Medline

46. C. Jolly, A. Metz, J. Govin, M. Vigneron, B. M. Turner, S. Khochbin, C. Vourc'h, Stress-induced transcription of satellite III repeats. *J. Cell Biol.* **164**, 25–33 (2004). doi:10.1083/jcb.200306104 Medline

47. L. Xie, J. Merjane, C. A. Bergmann, J. Xu, S. Balasubramaniyan, B. Hurtle, C. T. Chu, C. J. Donnelly, CUTS RNA Biosensor for the Real-Time Detection of TDP-43 Loss-of-Function. *eLife* **13**, RP101216 (2024). doi:10.7554/eLife.101216.2

48. K. Zhang, C. J. Donnelly, A. R. Haeusler, J. C. Grima, J. B. Machamer, P. Steinwald, E. L. Daley, S. J. Miller, K. M. Cunningham, S. Vidensky, S. Gupta, M. A. Thomas, I. Hong, S.-L. Chiu, R. L. Huganir, L. W. Ostrow, M. J. Matunis, J. Wang, R. Sattler, T. E. Lloyd, J. D. Rothstein, The *C9orf72* repeat expansion disrupts nucleocytoplasmic transport. *Nature* **525**, 56–61 (2015). doi:10.1038/nature14973 Medline

49. A. N. Coyne, V. Baskerville, B. L. Zaepfel, D. W. Dickson, F. Rigo, F. Bennett, C. P. Lusk, J. D. Rothstein, Nuclear accumulation of CHMP7 initiates nuclear pore complex injury and subsequent TDP-43 dysfunction in sporadic and familial ALS. *Sci. Transl. Med.* **13**, eabe1923 (2021). doi:10.1126/scitranslmed.abe1923 Medline

50. L. Xie, Y. Zhu, B. T. Hurtle, M. Wright, J. L. Robinson, J. C. Mauna, E. E. Brown, M. Ngo, C. A. Bergmann, J. Xu, J. Merjane, A. M. Gleixner, G. Grigorean, F. Liu, W. Rossoll, E. B. Lee, E. Kiskinis, M. Chikina, C. J. Donnelly, Context-dependent Interactors Regulate TDP-43 Dysfunction in ALS/FTLD. bioRxiv 2025.04.07.646890 [Preprint] (2025). doi:10.1101/2025.04.07.646890

51. V. Casiraghi, M. N. Sorce, S. Santangelo, S. Invernizzi, P. Bossolasco, C. Lattuada, C. Battaglia, M. Venturin, V. Silani, C. Colombrita, A. Ratti, Modeling of TDP-43 proteinopathy by chronic oxidative stress identifies rapamycin as beneficial in ALS patient-derived 2D and 3D iPSC models. *Exp. Neurol.* **383**, 115057 (2025). doi:10.1016/j.expneurol.2024.115057 Medline

52. B. J. Joseph, K. A. Marshall, P. Harley, J. R. Mann, F. Alessandrini, C. G. Vanoye, W. Chi, M. Prudencio, D. Simkin, T.-T. Kao, R. R. Desai, M. J. Keuss, S. Barattucci, M. Zanovello, P. R. Mehta, J.-M. DeKeyser, F. Limone, J. Lee, A.-L. Brown, M. F. Leyton-Jaimes, L. A. Nash, I. G. S. Juan, E. Aronica, B. J. Wainger, M. Shah, A. Goswami, N. A. Shneider, D. W. Dickson, J. Burrone, C. Zhang, H. Wichterle, L. Petrucelli, J. K. Watts, A. L. George Jr., P. Fratta, K. Eggan, E. Kiskinis, TDP-43-dependent mis-splicing of *KCNQ2* triggers intrinsic neuronal hyperexcitability in ALS/FTD. *Nat. Neurosci.* **28**, 2476–2492 (2025). doi:10.1038/s41593-025-02096-w Medline

53. Z. Melamed, J. López-Erauskin, M. W. Baughn, O. Zhang, K. Drenner, Y. Sun, F. Freyermuth, M. A. McMahon, M. S. Beccari, J. W. Artates, T. Ohkubo, M. Rodriguez, N. Lin, D. Wu, C. F. Bennett, F. Rigo, S. Da Cruz, J. Ravits, C. Lagier-Tourenne, D. W. Cleveland, Premature polyadenylation-mediated loss of stathmin-2 is a hallmark of TDP-43-dependent neurodegeneration. *Nat. Neurosci.* **22**, 180–190 (2019). doi:10.1038/s41593-018-0293-z Medline

54. S. Seddighi, Y. A. Qi, A.-L. Brown, O. G. Wilkins, C. Bereda, C. Belair, Y.-J. Zhang, M. Prudencio, M. J. Keuss, A. Khandeshi, S. Pickles, S. E. Kargbo-Hill, J. Hawrot, D. M. Ramos, H. Yuan, J. Roberts, E. K. Sacramento, S. I. Shah, M. A. Nalls, J. M. Colón-Mercado, J. F. Reyes, V. H. Ryan, M. P. Nelson, C. N. Cook, Z. Li, L. Screven, J. Y. Kwan, P. R. Mehta, M. Zanovello, M. Hallegger, A. Shantaraman, L. Ping, Y. Koike, B. Oskarsson, N. P. Staff, D. M. Duong, A. Ahmed, M. Secrier, J. Ule, S. Jacobson, D. S. Reich, J. D. Rohrer, A. Malaspina, D. W. Dickson, J. D. Glass, A. Ori, N. T. Seyfried, M. Maragkakis, L. Petrucelli, P. Fratta, M. E. Ward, Mis-spliced transcripts generate de novo proteins in TDP-43–related ALS/FTD. *Sci. Transl. Med.* **16**, eadg7162 (2024). doi:10.1126/scitranslmed.adg7162 Medline

55. N. H. Alami, R. B. Smith, M. A. Carrasco, L. A. Williams, C. S. Winborn, S. S. W. Han, E. Kiskinis, B. Winborn, B. D. Freibaum, A. Kanagaraj, A. J. Clare, N. M. Badders, B. Bilican, E. Chaum, S. Chandran, C. E. Shaw, K. C. Eggan, T. Maniatis, J. P. Taylor, Axonal transport of TDP-43 mRNA granules is impaired by ALS-causing mutations. *Neuron* **81**, 536–543 (2014). doi:10.1016/j.neuron.2013.12.018 Medline

56. J. P. Vessey, P. Macchi, J. M. Stein, M. Mikl, K. N. Hawker, P. Vogelsang, K. Wieczorek, G. Vendra, J. Riefler, F. Tübing, S. A. J. Aparicio, T. Abel, M. A. Kiebler, A loss of function allele for murine Staufen1 leads to impairment of dendritic Staufen1-RNP delivery and dendritic spine morphogenesis. *Proc. Natl. Acad. Sci. U.S.A.* **105**, 16374–16379 (2008). doi:10.1073/pnas.0804583105 Medline

57. B. K. Jensen, K. J. McAvoy, N. M. Heinsinger, A. C. Lepore, H. Ilieva, A. R. Haeusler, D. Trotti, P. Pasinelli, Targeting TNFα produced by astrocytes expressing amyotrophic lateral sclerosis-linked mutant fused in sarcoma prevents neurodegeneration and motor dysfunction in mice. *Glia* **70**, 1426–1449 (2022). doi:10.1002/glia.24183 Medline

58. A. C. Elden, H.-J. Kim, M. P. Hart, A. S. Chen-Plotkin, B. S. Johnson, X. Fang, M. Armakola, F. Geser, R. Greene, M. M. Lu, A. Padmanabhan, D. Clay-Falcone, L. McCluskey, L. Elman, D. Juhr, P. J. Gruber, U. Rüb, G. Auburger, J. Q. Trojanowski, V. M.-Y. Lee, V. M. Van Deerlin, N. M. Bonini, A. D. Gitler, Ataxin-2 intermediate-length polyglutamine expansions are associated with increased risk for ALS. *Nature* **466**, 1069–1075 (2010). doi:10.1038/nature09320 Medline

59. M. Prudencio, K. R. Jansen-West, W. C. Lee, T. F. Gendron, Y.-J. Zhang, Y.-F. Xu, J. Gass, C. Stuani, C. Stetler, R. Rademakers, D. W. Dickson, E. Buratti, L. Petrucelli, Misregulation of human sortilin splicing leads to the generation of a nonfunctional progranulin receptor. *Proc. Natl. Acad. Sci. U.S.A.* **109**, 21510–21515 (2012). doi:10.1073/pnas.1211577110 Medline

60. J. Gao, L. Wang, X. Ren, J. R. Dunn, A. Peters, M. Miyagi, H. Fujioka, F. Zhao, C. Askwith, J. Liang, X. Wang, Translational regulation in the brain by TDP-43 phase separation. *J. Cell Biol.* **220**, e202101019 (2021). doi:10.1083/jcb.202101019 Medline

61. P. Zhang, B. Fan, P. Yang, J. Temirov, J. Messing, H. J. Kim, J. P. Taylor, Chronic optogenetic induction of stress granules is cytotoxic and reveals the evolution of ALS-FTD pathology. *eLife* **8**, e39578 (2019). doi:10.7554/eLife.39578 Medline

62. Z. R. Grese, A. C. S. Bastos, L. D. Mamede, R. L. French, T. M. Miller, Y. M. Ayala, Specific RNA interactions promote TDP-43 multivalent phase separation and maintain liquid properties. *EMBO Rep.* **22**, e53632 (2021). doi:10.15252/embr.202153632 Medline

63. B. Khalil, M. Linsenmeier, C. L. Smith, J. Shorter, W. Rossoll, Nuclear-import receptors as gatekeepers of pathological phase transitions in ALS/FTD. *Mol. Neurodegener.* **19**, 8 (2024). doi:10.1186/s13024-023-00698-1 Medline

64. J. A. Ortega, E. L. Daley, S. Kour, M. Samani, L. Tellez, H. S. Smith, E. A. Hall, Y. T. Esengul, Y.-H. Tsai, T. F. Gendron, C. J. Donnelly, T. Siddique, J. N. Savas, U. B. Pandey, E. Kiskinis, Nucleocytoplasmic Proteomic Analysis Uncovers eRF1 and Nonsense-Mediated Decay as Modifiers of ALS/FTD *C9orf72* Toxicity. *Neuron* **106**, 90–107.e13 (2020). doi:10.1016/j.neuron.2020.01.020 Medline

65. M. J. Ziller, J. A. Ortega, K. A. Quinlan, D. P. Santos, H. Gu, E. J. Martin, C. Galonska, R. Pop, S. Maidl, A. Di Pardo, M. Huang, H. Y. Meltzer, A. Gnirke, C. J. Heckman, A. Meissner, E. Kiskinis, Dissecting the Functional Consequences of *De Novo* DNA Methylation Dynamics in Human Motor Neuron Differentiation and Physiology. *Cell Stem Cell* **22**, 559–574.e9 (2018). doi:10.1016/j.stem.2018.02.012 Medline

66. A. Wang, A. E. Conicella, H. B. Schmidt, E. W. Martin, S. N. Rhoads, A. N. Reeb, A. Nourse, D. Ramirez Montero, V. H. Ryan, R. Rohatgi, F. Shewmaker, M. T. Naik, T. Mittag, Y. M. Ayala, N. L. Fawzi, A single N-terminal phosphomimic disrupts TDP-43 polymerization, phase separation, and RNA splicing. *EMBO J.* **37**, e97452 (2018). doi:10.15252/embj.201797452 Medline

67. E. Bogaert, S. Boeynaems, M. Kato, L. Guo, T. R. Caulfield, J. Steyaert, W. Scheveneels, N. Wilmans, W. Haeck, N. Hersmus, J. Schymkowitz, F. Rousseau, J. Shorter, P. Callaerts, W. Robberecht, P. Van Damme, L. Van Den Bosch, Molecular Dissection of FUS Points at Synergistic Effect of Low-Complexity Domains in Toxicity. *Cell Rep.* **24**, 529–537.e4 (2018). doi:10.1016/j.celrep.2018.06.070 Medline

68. Y. Hamuro, Quantitative Hydrogen/Deuterium Exchange Mass Spectrometry. *J. Am. Soc. Mass Spectrom.* **32**, 2711–2727 (2021). doi:10.1021/jasms.1c00216 Medline

69. L. Mayne, Z.-Y. Kan, P. S. Chetty, A. Ricciuti, B. T. Walters, S. W. Englander, Many overlapping peptides for protein hydrogen exchange experiments by the fragment separation-mass spectrometry method. *J. Am. Soc. Mass Spectrom.* **22**, 1898–1905 (2011). doi:10.1007/s13361-011-0235-4 Medline

70. P. Mohanty, J. Shenoy, A. Rizuan, J. F. Mercado-Ortiz, N. L. Fawzi, J. Mittal, A synergy between site-specific and transient interactions drives the phase separation of a disordered, low-complexity domain. *Proc. Natl. Acad. Sci. U.S.A.* **120**, e2305625120 (2023). doi:10.1073/pnas.2305625120 Medline

71. Y. Luo, B. Roux, Simulation of Osmotic Pressure in Concentrated Aqueous Salt Solutions. *J. Phys. Chem. Lett.* **1**, 183–189 (2009). doi:10.1021/jz900079w

72. R. B. Best, W. Zheng, J. Mittal, Balanced Protein–Water Interactions Improve Properties of Disordered Proteins and Non-Specific Protein Association. *J. Chem. Theory Comput.* **10**, 5113–5124 (2014). doi:10.1021/ct500569b Medline

73. G. H. Zerze, W. Zheng, R. B. Best, J. Mittal, Evolution of All-Atom Protein Force Fields to Improve Local and Global Properties. *J. Phys. Chem. Lett.* **10**, 2227–2234 (2019). doi:10.1021/acs.jpclett.9b00850 Medline

74. M. Zgarbová, M. Otyepka, J. Šponer, A. Mládek, P. Banáš, T. E. Cheatham 3rd, P. Jurečka, Refinement of the Cornell et al. Nucleic Acids Force Field Based on Reference Quantum Chemical Calculations of Glycosidic Torsion Profiles. *J. Chem. Theory Comput.* **7**, 2886–2902 (2011). doi:10.1021/ct200162x Medline

75. T. Steinbrecher, J. Latzer, D. A. Case, Revised AMBER parameters for bioorganic phosphates. *J. Chem. Theory Comput.* **8**, 4405–4412 (2012). doi:10.1021/ct300613v Medline

76. B. Ozguney, P. Mohanty, J. Mittal, RNA binding tunes the conformational plasticity and intradomain stability of TDP-43 tandem RNA recognition motifs. *Biophys. J.* **123**, 3844–3855 (2024). doi:10.1016/j.bpj.2024.09.031 Medline

77. M. J. Abraham, T. Murtola, R. Schulz, S. Páll, J. C. Smith, B. Hess, E. Lindahl, GROMACS: High performance molecular simulations through multi-level parallelism from laptops to supercomputers. *SoftwareX* **1-2**, 19–25 (2015). doi:10.1016/j.softx.2015.06.001

78. G. Bussi, D. Donadio, M. Parrinello, Canonical sampling through velocity rescaling. *J. Chem. Phys.* **126**, 014101 (2007). doi:10.1063/1.2408420 Medline

79. M. Parrinello, A. Rahman, Polymorphic transitions in single crystals: A new molecular dynamics method. *J. Appl. Phys.* **52**, 7182–7190 (1981). doi:10.1063/1.328693

80. D. A. Case, H. M. Aktulga, K. Belfon, D. S. Cerutti, G. A. Cisneros, V. W. D. Cruzeiro, N. Forouzesh, T. J. Giese, A. W. Götz, H. Gohlke, S. Izadi, K. Kasavajhala, M. C. Kaymak, E. King, T. Kurtzman, T.-S. Lee, P. Li, J. Liu, T. Luchko, R. Luo, M. Manathunga, M. R. Machado, H. M. Nguyen, K. A. O'Hearn, A. V. Onufriev, F. Pan, S. Pantano, R. Qi, A. Rahnamoun, A. Risheh, S. Schott-Verdugo, A. Shajan, J. Swails, J. Wang, H. Wei, X. Wu, Y. Wu, S. Zhang, S. Zhao, Q. Zhu, T. E. Cheatham 3rd, D. R. Roe, A. Roitberg, C. Simmerling, D. M. York, M. C. Nagan, K. M. Merz Jr., AmberTools. *J. Chem. Inf. Model.* **63**, 6183–6191 (2023). doi:10.1021/acs.jcim.3c01153 Medline

81. C. W. Hopkins, S. Le Grand, R. C. Walker, A. E. Roitberg, Long-Time-Step Molecular Dynamics through Hydrogen Mass Repartitioning. *J. Chem. Theory Comput.* **11**, 1864–1874 (2015). doi:10.1021/ct5010406 Medline

82. J. Åqvist, P. Wennerström, M. Nervall, S. Bjelic, B. O. Brandsdal, Molecular dynamics simulations of water and biomolecules with a Monte Carlo constant pressure algorithm. *Chem. Phys. Lett.* **384**, 288–294 (2004). doi:10.1016/j.cplett.2003.12.039

83. T. Darden, D. York, L. Pedersen, Particle mesh Ewald: An *N*·log(*N*) method for Ewald sums in large systems. *J. Chem. Phys.* **98**, 10089–10092 (1993). doi:10.1063/1.464397

84. J.-P. Ryckaert, G. Ciccotti, H. J. C. Berendsen, Numerical integration of the cartesian equations of motion of a system with constraints: Molecular dynamics of *n*-alkanes. *J. Comput. Phys.* **23**, 327–341 (1977). doi:10.1016/0021-9991(77)90098-5

85. F. Delaglio, S. Grzesiek, G. W. Vuister, G. Zhu, J. Pfeifer, A. Bax, NMRPipe: A multidimensional spectral processing system based on UNIX pipes. *J. Biomol. NMR* **6**, 277–293 (1995). doi:10.1007/BF00197809 Medline

86. S. P. Skinner, R. H. Fogh, W. Boucher, T. J. Ragan, L. G. Mureddu, G. W. Vuister, CcpNmr AnalysisAssign: A flexible platform for integrated NMR analysis. *J. Biomol. NMR* **66**, 111–124 (2016). doi:10.1007/s10858-016-0060-y Medline

87. J. Ganssauge, S. Hawkins, S. C. Namboori, S. K. Leung, J. Mill, A. Bhinge, Rapid and inducible mislocalization of endogenous TDP43 in a novel human model of amyotrophic lateral sclerosis. *eLife* **13**, RP95062 (2025). doi:10.7554/eLife.95062.3 Medline

88. Z. Y. Kan, X. Ye, J. J. Skinner, L. Mayne, S. W. Englander, ExMS2: An Integrated Solution for Hydrogen–Deuterium Exchange Mass Spectrometry Data Analysis. *Anal. Chem.* **91**, 7474–7481 (2019). doi:10.1021/acs.analchem.9b01682 Medline

89. Y. Perez-Riverol, C. Bandla, D. J. Kundu, S. Kamatchinathan, J. Bai, S. Hewapathirana, N. S. John, A. Prakash, M. Walzer, S. Wang, J. A. Vizcaíno, The PRIDE database at 20 years: 2025 update. *Nucleic Acids Res.* **53**, D543–D553 (2025). doi:10.1093/nar/gkae1011 Medline

90. J. Shorter, Data from: Short RNA chaperones promote aggregation-resistant TDP-43 conformers to mitigate neurodegeneration, Dryad (2026). doi:10.5061/dryad.9s4mw6mx4

91. Q. Meng, Y.-L. Song, C. Zhou, H. He, N. Zhang, H. Zhou, A hydrogen-deuterium exchange mass spectrometry-based protocol for protein-small molecule interaction analysis. *Biophys. Rep.* **9**, 99–111 (2023). doi:10.52601/bpr.2023.230006 Medline

92. J. Zhang, P. Ramachandran, R. Kumar, M. L. Gross, H/D exchange centroid monitoring is insufficient to show differences in the behavior of protein states. *J. Am. Soc. Mass Spectrom.* **24**, 450–453 (2013). doi:10.1007/s13361-012-0555-z Medline

93. G. R. Masson, J. E. Burke, N. G. Ahn, G. S. Anand, C. Borchers, S. Brier, G. M. Bou-Assaf, J. R. Engen, S. W. Englander, J. Faber, R. Garlish, P. R. Griffin, M. L. Gross, M. Guttman, Y. Hamuro, A. J. R. Heck, D. Houde, R. E. Iacob, T. J. D. Jørgensen, I. A. Kaltashov, J. P. Klinman, L. Konermann, P. Man, L. Mayne, B. D. Pascal, D. Reichmann, M. Skehel, J. Snijder, T. S. Strutzenberg, E. S. Underbakke, C. Wagner, T. E. Wales, B. T. Walters, D. D. Weis, D. J. Wilson, P. L. Wintrode, Z. Zhang, J. Zheng, D. C. Schriemer, K. D. Rand, Recommendations for performing, interpreting and reporting hydrogen deuterium exchange mass spectrometry (HDX-MS) experiments. *Nat. Methods* **16**, 595–602 (2019). doi:10.1038/s41592-019-0459-y Medline

94. G. M. Carlson, A. W. Fenton, What Mutagenesis Can and Cannot Reveal About Allostery. *Biophys. J.* **110**, 1912–1923 (2016). doi:10.1016/j.bpj.2016.03.021 Medline

95. V. J. Hilser, E. B. Thompson, Intrinsic disorder as a mechanism to optimize allosteric coupling in proteins. *Proc. Natl. Acad. Sci. U.S.A.* **104**, 8311–8315 (2007). doi:10.1073/pnas.0700329104 Medline

96. X. Pang, H. X. Zhou, Disorder-to-Order Transition of an Active-Site Loop Mediates the Allosteric Activation of Sortase A. *Biophys. J.* **109**, 1706–1715 (2015). doi:10.1016/j.bpj.2015.08.039 Medline

97. S. A. Wankowicz, J. S. Fraser, Advances in uncovering the mechanisms of macromolecular conformational entropy. *Nat. Chem. Biol.* **21**, 623–634 (2025). doi:10.1038/s41589-025-01879-3 Medline

98. B. N. Flores, X. Li, A. M. Malik, J. Martinez, A. A. Beg, S. J. Barmada, An Intramolecular Salt Bridge Linking TDP43 RNA Binding, Protein Stability, and TDP43-Dependent Neurodegeneration. *Cell Rep.* **27**, 1133–1150.e8 (2019). doi:10.1016/j.celrep.2019.03.093 Medline

99. A. Son, V. Huizar Cabral, Z. Huang, T. J. Litberg, S. Horowitz, G-quadruplexes rescuing protein folding. *Proc. Natl. Acad. Sci. U.S.A.* **120**, e2216308120 (2023). doi:10.1073/pnas.2216308120 Medline

100. S. H. Ou, F. Wu, D. Harrich, L. F. García-Martínez, R. B. Gaynor, Cloning and characterization of a novel cellular protein, TDP-43, that binds to human immunodeficiency virus type 1 TAR DNA sequence motifs. *J. Virol.* **69**, 3584–3596 (1995). doi:10.1128/jvi.69.6.3584-3596.1995 Medline